



Development of Advanced Compton Imaging Camera
with Gaseous Electron Tracker
and
First Flight of Sub-MeV Gamma-Ray Imaging
Loaded-on-Balloon Experiment

Atsushi Takada

Department of Physics, Faculty of Science, Kyoto University
Kitashirakawa Oiwake-cho, Sakyo-ku, Kyoto, 606-8502, Japan
takada@cr.scphys.kyoto-u.ac.jp

This thesis was submitted to the Department of Physics,
Graduate School of Science, Kyoto University
on May 8, 2007
in partial fulfillment of the requirements
for the degree of Doctor of Philosophy in physics.

Abstract

For a MeV gamma-ray telescope in the next generation, we developed an Electron Tracking Compton Camera, which consists of a tracker and an absorber. The camera obtains the energy and the direction of both the scattered gamma-ray and the recoil electron, and determines both the energy and the direction of the incident gamma-ray, photon by photon. Also this camera rejects the backgrounds using the kinematics of Compton scattering. We use a μ -TPC as the tracker and the GSO:Ce pixel scintillator arrays as the absorbers. A μ -TPC is a gaseous time projection chamber, which has a high gas gain of 2×10^4 and a good position resolution of $\sim 500 \mu\text{m}$. Our Compton camera is expected to have a good signal to noise ratio and a good angular resolution due to a gaseous high resolution tracker.

In this thesis, I reported things as below. First, in order to verify the principle of the gamma-ray reconstruction and the background rejection due to the Compton scattering kinematics, we constructed a prototype camera using μ -TPC filling with an Ar gas. By this prototype, we obtained the images and the spectra of the gamma-rays from the radioactive sources, and measured the performance of the prototype camera. Next, in order to measure diffuse cosmic gamma-rays and atmospheric gamma-rays, we designed and constructed a flight model detector with an improvement of the detection efficiency using a Xe gas as a Compton scattering target. By this improvement, the detection efficiency was 10 times larger than that of the prototype and the FOV spread to 3 str. Finally, we loaded the flight model on a balloon, and launched on September 1 2006 as the 1st flight of Sub-MeV gamma-ray Imaging Loaded-on-balloon Experiment (SMILE). The balloon reached to 35 km at altitude, and the level flight continued during 4 hours. We succeeded in the detection of ~ 200 downward gamma-rays during the 3.5 hours level flight (live time 3.0 hours). The detected photon number was consistent to the simulated one, which was ~ 200 photons in 3 hours. By this balloon experiment, we succeeded in the observation of the fluxes of diffuse gamma-ray and atmospheric gamma-ray between 100 keV and 1 MeV.

Contents

1	MeV Gamma-Ray Astronomy	1
1.1	Production Mechanism of Gamma-Ray	1
1.1.1	Synchrotron Radiation	3
1.1.2	Bremsstrahlung	3
1.1.3	Inverse Compton Scattering	4
1.1.4	Nuclear Transitions and Decay	4
1.1.5	Annihilation	5
1.2	Sky in Gamma-Ray	6
1.2.1	All sky map	6
1.2.2	Galactic diffuse gamma-ray	6
1.2.3	Extragalactic diffuse gamma-ray	6
1.3	Source of Gamma-Rays	9
1.3.1	Supernova Remnant	9
1.3.2	Spin-Down Pulsars	10
1.3.3	Black Hole	13
1.3.4	Galactic Center	14
1.3.5	Active Galactic Nuclei (AGN)	15
1.3.6	Solar Flare	16
1.3.7	Gamma-Ray Burst	16
2	Detection of Gamma-Rays	19
2.1	Interaction of Gamma-Rays and Matter	19
2.1.1	Photoelectric Absorption	19
2.1.2	Compton Scattering	20
2.1.3	Pair Creation	20
2.2	Sub-MeV/MeV Gamma-Ray Imaging	21
2.2.1	Active and Passive Collimators	22
2.2.2	Coded Aperture Imaging	23
2.2.3	Gamma-Ray Lenses	24
2.2.4	Compton Imaging	25
2.2.5	Pair Tracking	28
2.2.6	Summary of MeV Gamma-Ray Imaging	28
2.3	Low Energy Gamma-Ray Observatories	30
2.3.1	CGRO	30
2.3.2	INTEGRAL	31
3	Advanced Compton Imaging	33
3.1	Imaging by Electron Tracking Compton Method	33
3.2	Background Rejection	35
3.3	Doppler Broadening	36
3.4	Multiple Scattering	37

CONTENTS

3.5	Composition of Advanced Compton Camera	38
3.5.1	Goal for Next Generation Telescopes	38
3.5.2	Requirements for Tracker and Absorber	39
3.5.3	Advanced Compton Camera with Gaseous Electron Tracker	41
4	μ-PIC, μ-TPC & Scintillator	43
4.1	μ -PIC (Micro Pixel Chamber)	43
4.1.1	Introduction of μ -PIC	43
4.1.2	Morphology of Pixels	44
4.1.3	Readout Circuit	45
4.1.4	Performance of μ -PIC	49
4.1.5	μ -PIC as an X-ray Imaging Detector	50
4.2	Time Projection Chamber with μ -PIC (μ -TPC)	51
4.2.1	Structure and Principle of μ -TPC	51
4.2.2	Gas Electron Multiplier	51
4.2.3	Drift and Diffusion	52
4.2.4	Spectroscopy	54
4.3	Scintillation Camera	55
4.3.1	Scintillator & PMT	55
4.3.2	HV Operation/Readout System	57
4.3.3	Image and Energy Spectrum	58
5	Tracking of Charged Particles	59
5.1	Tracking of Cosmic Muon	59
5.1.1	DAQ System for Muon Tracking	59
5.1.2	Tracks of Muon & Track Efficiency	60
5.1.3	Clock Counter Histogram	61
5.1.4	dE/dX Spectrum	61
5.1.5	Position Resolution	61
5.1.6	Threshold	62
5.2	Tracking of Recoil Electron	62
5.2.1	Fixing of the Track Points	63
5.2.2	Connection of the Points	64
5.2.3	Selection of the Stopping Electron	65
5.2.4	Judgement of the Initial/End Point of the Track	65
5.2.5	Determination of the Recoil Direction	66
6	Prototype Camera	67
6.1	Prototype Setup	67
6.1.1	Absorber & Tracker of Prototype	67
6.1.2	Alignment of Prototype Camera	68
6.1.3	Data Acquisition System of Prototype Camera	68
6.2	Reconstruction of Gamma-Ray	70
6.2.1	Event Selection	70
6.2.2	Reconstructed Gamma-Rays	71
6.2.3	Effect of α Cut	75
6.2.4	Comparison with Classical Compton Imaging	75
6.3	Performance of Prototype Camera	75

7	Flight Model Detector	79
7.1	Design of Flight Model	79
7.1.1	Cosmic-Ray Fluxes at Balloon Altitude	79
7.1.2	Design of Flight Model for First Flight	80
7.1.3	Particle Incoming to Detector	80
7.1.4	Expectation of Gamma-Ray Detection	82
7.2	Data Acquisition of Flight Model Detector	82
7.2.1	Compton Camera Mode	84
7.2.2	Charged Particle Tracking Mode	86
7.2.3	Dead Time Measurement & Condition Monitoring System	86
7.3	Flight Model μ -TPC	86
7.3.1	Properties of TPC Gas	87
7.3.2	Gain Uniformity	87
7.3.3	Clock Counter Histogram	88
7.3.4	Energy Resolution	88
7.3.5	Position Resolution	89
7.3.6	Summary of Flight Model μ -TPC	90
7.4	Performance of Flight Model Detector	90
8	Balloon Flight	95
8.1	First Flight of SMILE	95
8.1.1	Specification of Physical Instrument	95
8.1.2	Flight Path and Operation Mode	97
8.2	Status of Detector in Balloon Flight	98
8.2.1	House Keeping Data	98
8.2.2	Count Rate of Scintillators	98
8.2.3	Current of μ -TPC	101
8.2.4	Dead Time & Event Rate	101
8.3	Results of Experiment & Discussion	103
8.3.1	Charged Particle Tracking Mode	103
8.3.2	Compton Camera Mode	104
9	Summary & Future Work	115

Chapter 1

MeV Gamma-Ray Astronomy

Once, the astronomy meant the studies of the stars' and planets' movements with the visible light observation, and hence the image of the universe was static and silent. However, astronomers now observe not only the electromagnetic waves from radio to gamma-ray but also cosmic-rays, neutrinos and so on. By these new windows, we have got the new various information that the universe is active and violent.

Gamma-ray is one of these new windows. Figure 1.1 shows the history of the gamma-ray observatories in space. The gamma-ray observations started in 1961, which was almost the same time as the discovery of Sco X-1. After the prediction by Hayakawa et al. in early 1950s about the existence of the gamma-ray radiation due to the decay of π^0 created by the interaction of cosmic-rays and interstellar matter, several gamma-ray sources were discovered by the satellites, OSO-7 (≥ 500 MeV) in 1967, SAS-2 (> 30 MeV) in 1972 and COS-B (2 keV - 5 GeV) in 1975. Besides, low-energy gamma-rays were observed by Granat which was launched in 1989 by Russia and France, and CGRO which was launched in 1991 by United States. Recently, INTEGRAL was launched in 2004 by ESA, and GLAST will be launched soon in 2007. On the ground, very high-energy gamma-rays of energy about 10^{12} eV were observed by Cherenkov telescopes, Whipple, HEGRA and CANGAROO, in 1990s.

Although gamma-rays mean all electromagnetic waves with the energy above a few hundred keV, the gamma-rays of each MeV - TeV energy band provide us the different information even if they were emitted from same object. A gamma-ray observation in the MeV region provides the information of the nucleosynthesis, the particle acceleration and the interaction of cosmic-rays and interstellar matter. MeV gamma-rays are hardly attenuated from source objects to the earth, but can't pass through the atmosphere (Figure 1.2). Thus celestial MeV gamma-rays must be obtained outside the atmosphere. In this energy band, the number of photons is less than X-ray, and the complete absorption of photon is difficult because of the dominated process of Compton scattering. Besides this energy band has the backgrounds of photons produced by the hadron process of cosmic-ray and satellite body, although the band above 100 MeV has no background. Consequently the observation is very difficult, and the MeV gamma-rays astronomy has not been advanced than other energy bands.

1.1 Production Mechanism of Gamma-Ray

Thermal radiation is an emission from a large population of electromagnetically interacting particles in equilibrium, with their mean energy characterized by temperature T . The spectrum of radiation intensity follows the 'black body' distribution, and the energy density of radiation at frequency ν is

$$I_\nu = \frac{8\pi h\nu^3}{c^3} \frac{1}{e^{h\nu/k_B T} - 1}, \quad (1.1)$$

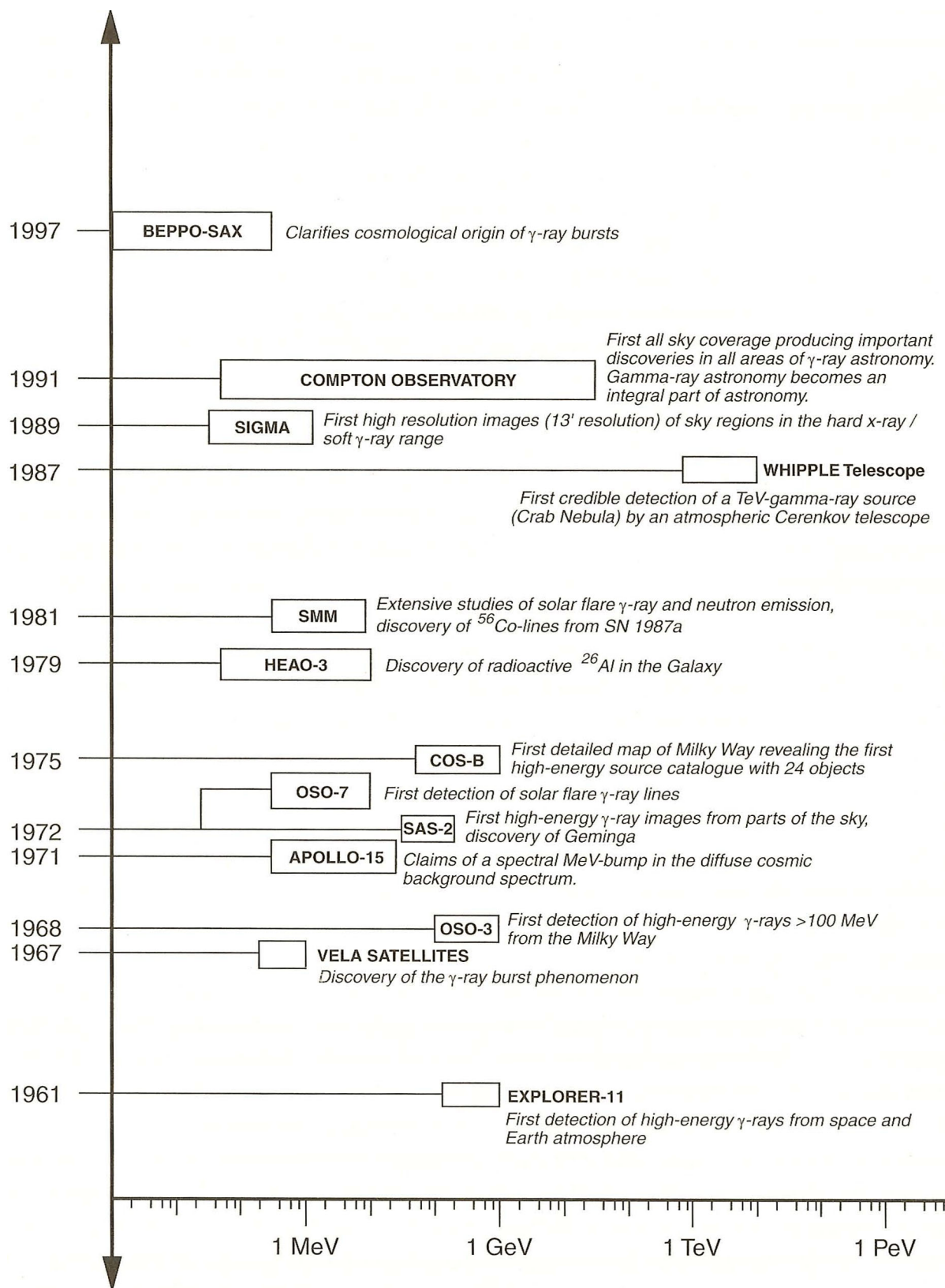


Figure 1.1: The history of Gamma-Ray Observatories [1]

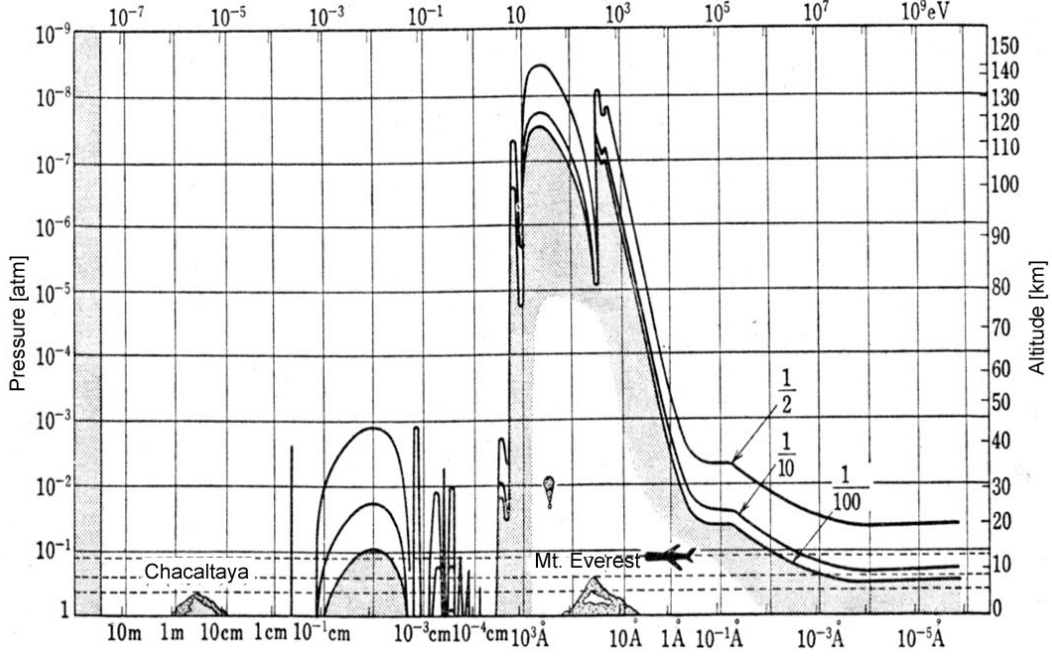


Figure 1.2: The attenuation by atmosphere in multi-wavelength [2]

where h is Planck's constant, and k_B is Boltzmann's constant. For the thermal gamma-rays of 1 MeV, the corresponding temperature would be above 10^9 K. Thus, thermal process is not reasonable, and nonthermal processes are the more reasonable source of gamma-rays. In the MeV region, several nonthermal processes exist as follows.

1.1.1 Synchrotron Radiation

When a relativistic electron moves via the magnetic field B , an electron trajectory will be changed by the Lorentz force. Because any acceleration of the charged particle can be viewed as the modification of the field, the kinetic energy of the electron is transformed into the energy of the electromagnetic field. For the relativistic electron, such an energy loss as an emission of photon, which is called Synchrotron Radiation.

Synchrotron radiation spectrum has a peak at the characteristic as

$$h\nu_c = \frac{3h e B_{\perp}}{4\pi m_e c} \left(\frac{E_e}{m_e c^2} \right)^2, \quad (1.2)$$

where, e , m_e , E_e are charge, mass, energy of the electron, respectively, and $B_{\perp} = B \sin \theta$ with the pitch angle θ which is the angle between the particle trajectory and the direction of the magnetic field. The total energy loss rate by synchrotron radiation of an electron moving in the magnetic field B is

$$-\left(\frac{dE_e}{dt} \right)_{\text{syn}} = \frac{4}{3} \sigma_T c \frac{B^2}{8\pi} \gamma^2 \beta^2, \quad (1.3)$$

where $\sigma_T = \frac{8\pi e^4}{3m_e^2 c^4}$ is Thomson cross section.

1.1.2 Bremsstrahlung

Another important process of gamma-ray production is 'Bremsstrahlung'. When an electron passes very near the nucleus, the electron's trajectory is substantially changed by the strong electric field of the nucleus, and photons are emitted.

The spectrum of bremsstrahlung radiation remains flat up to roughly the electron kinetic energy, and it drops sharply toward zero above. For relativistic electrons in a fully ionized plasma (no screening), the bremsstrahlung loss is

$$-\left(\frac{dE_e}{dt}\right)_B = 4n_a Z^2 r_0^2 \alpha c \left(\ln \frac{E_e}{m_e c^2} + 0.36 \right) E_e. \quad (1.4)$$

In the case of total screening, above formula is modified to

$$-\left(\frac{dE_e}{dt}\right)_B = 4n_a Z^2 r_0^2 \alpha c \left(\ln \frac{183}{Z^{-1/3}} - \frac{1}{18} \right) E_e, \quad (1.5)$$

where n_a is the target atom density, $r_0 = \frac{e^2}{m_e c^2}$ is the classical radius of the electron, and α is the fine structure constant.

1.1.3 Inverse Compton Scattering

When an energetic photon collides with a low energy electron, the photon is scattered and some of the photon energy transfers to the electron. This process is called Compton scattering. The inverse process also surely exists, and generates a gamma-ray: when the low energy photons collide with energetic electrons, these photons gain the some amount of the energy of the electron via the collision. This ‘Inverse Compton Scattering’ is important in the regions of the high photon density.

The energy loss for an electron in the photon field energy density w_{ph} is written as

$$-\left(\frac{dE_e}{dt}\right)_{IC} = \frac{4}{3} \sigma_T c w_{ph} \gamma^2 \beta^2. \quad (1.6)$$

1.1.4 Nuclear Transitions and Decay

A nucleus has several specific, quantized states of the energy to bind the nucleons. These nuclear states have typical energy bands of the MeV scale, and hence the transition between those states of a nuclear absorbs or emits the MeV gamma-ray photons. Thus, the gamma-rays are emitted from ‘de-excitation’ of a nucleus:

$$X^* \longrightarrow X + \gamma, \quad (1.7)$$

and ‘radioactive decay’:

$$X \longrightarrow Y^* + e^+ \longrightarrow Y + \gamma. \quad (1.8)$$

De-excitation occurs by the energetic collisions of cosmic-rays with the interstellar gas nuclei, in the space. On the other hand, a radioactive decay occurs by nuclearsynthesis in a supernova and a core of heavy stars. The examples of line gamma-ray emissions by nuclear transitions expected in the universe are listed up in Table 1.1.

Pion is a boson involved in the strong nuclear interaction, and is created during the strong-interaction events such as collisions of cosmic-ray protons with ambient-gas nuclei. The dominant π -producing channels in hadronic interactions are as follows

$$p + p \longrightarrow p + p + a\pi^0 + b(\pi^+ + \pi^-), \quad (1.9)$$

$$p + p \longrightarrow p + n + \pi^+ + a\pi^0 + b(\pi^+ + \pi^-), \quad (1.10)$$

where a and b are positive integers. A π^0 decays rapidly into two gamma-rays with a proper time of 9×10^{-17} sec, and the distribution of the photon energy has a peak at about 70 MeV at the center of gravity system, which is the half of the rest mass of pion. Because pions created by energetic protons has a momentum distribution, the observed gamma-ray spectrum of the pion decay is broadened by Doppler shift.

Table 1.1: The gamma-rays by nuclear transitions [1, 3, 4]

process		Energy [MeV]
De-Excitation	$^{12}\text{C}^*$	4.438
	$^{14}\text{N}^*$	2.313, 5.105
	$^{16}\text{O}^*$	2.741, 6.129, 6.917, 7.117
	$^{26}\text{Mg}^*$	1.809
	$^{56}\text{Fe}^*$	0.847, 1.238, 1.811
radioactive decay	^{56}Ni (6.10 d)	0.158, 0.270, 0.480, 0.759, 0.812
	^{56}Co (77.2 d)	0.847, 1.238, 2.598
	^{57}Co (271.7 d)	0.122, 0.136
	^{44}Ti (63 y)	1.157
	^{26}Al (7.4×10^5 y)	1.809
	^{60}Fe (1.5×10^6 y)	1.173, 1.333
capture	$n + ^1\text{H} \rightarrow ^2\text{D} + \gamma$	2.223

1.1.5 Annihilation

An electron-positron annihilation is an important source of gamma-rays. In the annihilation, two or more photons are created, and the total energy of electron and positron is distributed to these photons. Positron and electron may form a bound system, which is called positronium, and two different states exist. One is the ground state, and a positronium decays to two gamma-rays. In this case, each photon has an energy of 511 keV, which is equal to the rest energy of an electron. The other state is the parallel-spin state, and it decays to three gamma-rays having the continuum spectrum.

Actually, the 511 keV line was observed at near the Galactic Center by SMM and OSSE, and implied the annihilation rate of $\sim 2 \times 10^{43} \text{ sec}^{-1}$. Annihilation photons suggests the existence of the electron-positron plasma. Positrons are produced by β^+ -decay, decay of π^+ and the collision of hadronic antiparticles and normal matter. The examples of the radioactive isotopes causing β^+ -decay are ^{26}Al , ^{44}Ti , ^{56}Co , and the distinct nova products ^{13}N and ^{18}F . On the other hand, π^+ s would be produced at the vicinity of the compact stars.

However, positrons would be also produced by the decay of the intrinsic radioactive isotopes or the interactions of the cosmic-rays with the satellite platform. Therefore, spectral decomposition of annihilation photons from the inner Galaxy is considered to be quite difficult.

1.2 Sky in Gamma-Ray

1.2.1 All sky map

For the all sky survey in gamma-ray, Compton Gamma-Ray Observatory (CGRO) satellite had 4 detectors: COMPTEL, EGRET, OSSE and BATSE. COMPTEL found about 30 gamma-ray sources in the MeV region [5], and EGRET found about 270 sources in the sub GeV region [6]. Figures 1.3 and 1.4 show the all sky maps of the gamma-ray obtained by EGRET and COMPTEL, respectively. These images show that the gamma-rays are radiated from not only the compact objects but also the solar flare. Besides, in EGRET observations, Figure 1.3 says there are about 170 undefined objects of which counter part are not identified by other energy bands.

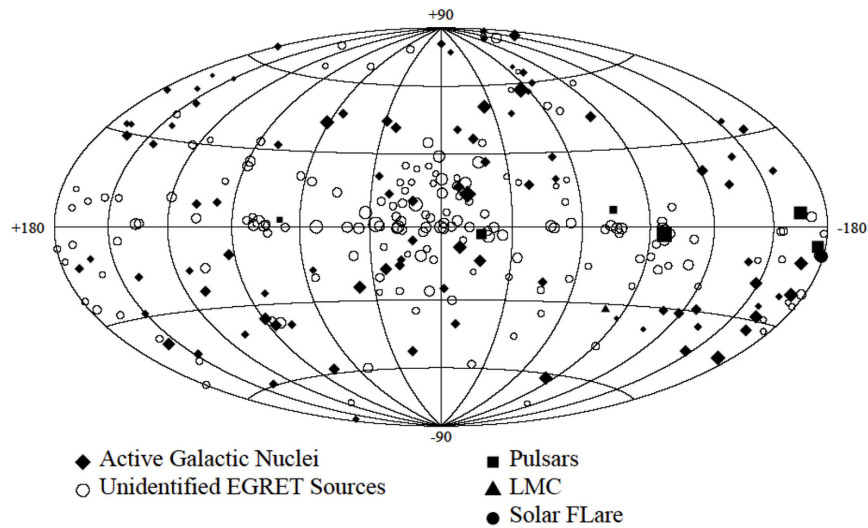


Figure 1.3: The distribution of the gamma-ray objects by EGRET [6]

1.2.2 Galactic diffuse gamma-ray

The gamma-rays from the Galactic Plane were also observed by those detectors. Figures 1.4, 1.5 and 1.6 show the galactic diffuse gamma-ray radiation in both energy regions.. Figure 1.7 shows the multi-wave energy spectrum of the galactic diffuse gamma-rays and X-rays. In the energy region from sub MeV to MeV, photons are mainly produced by the bremsstrahlung and the inverse Compton scattering of an electron [7].

On the other hand, the galactic diffuse gamma-rays in the MeV region consist of not only the continuum component but also the line emissions. Figure 1.5 the all sky map of 1.8 MeV from the decay of ^{26}Al . The source of the gamma-ray of 1.8 MeV is the decay of ^{26}Al ($T_{1/2} \approx 10^6 \text{ year}$), which is considered to be synthesized in the cores of massive stars.

However, in the observation of the point-sources near the galactic plane, the galactic diffuse gamma-rays make difficult to observe them as the background.

1.2.3 Extragalactic diffuse gamma-ray

Extragalactic diffuse gamma-rays come from the outside of the Galaxy, of which the distribution is uniform in the all sky. Figure 1.8 is the spectrum of the extragalactic diffuse gamma-ray. The spectrum is explained by the combination of the emissions from AGNs and the type Ia supernovae. Particularly, in the energy region of MeV gamma-rays, the majority is considered to be gamma-rays by type Ia supernovae in galaxies.

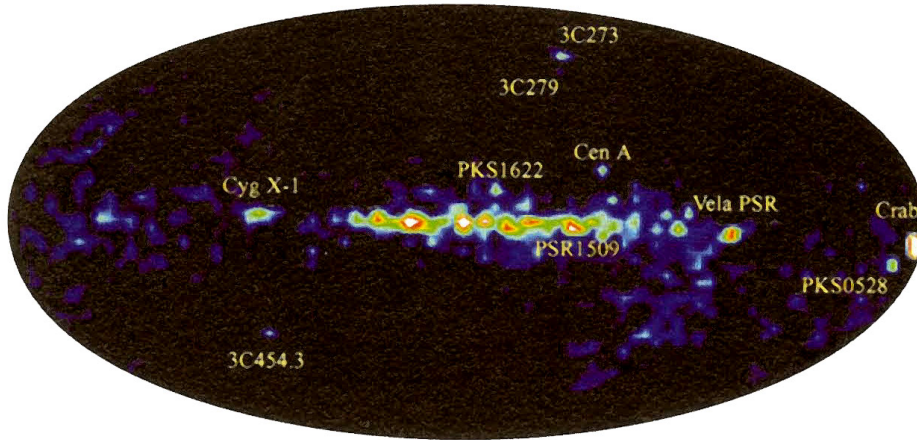


Figure 1.4: The all sky map by COMPTEL (1 - 30 MeV) [1]

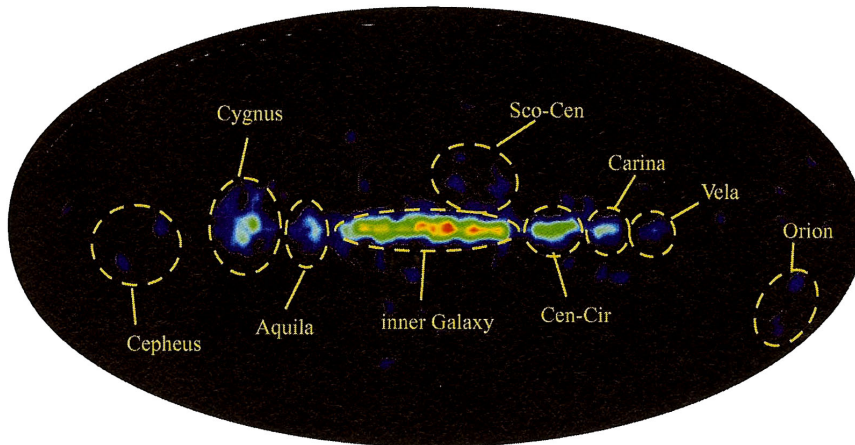


Figure 1.5: The all sky map in 1.8 MeV by COMPTEL [1]

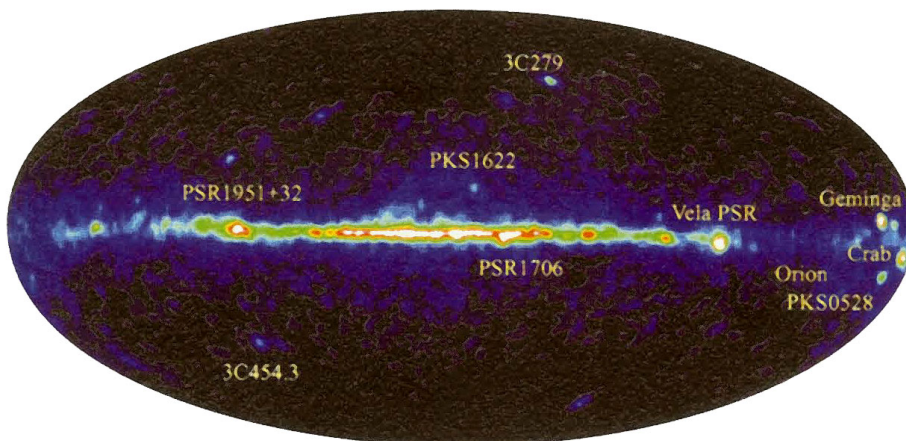


Figure 1.6: The all sky map by EGRET (≥ 100 MeV) [1]

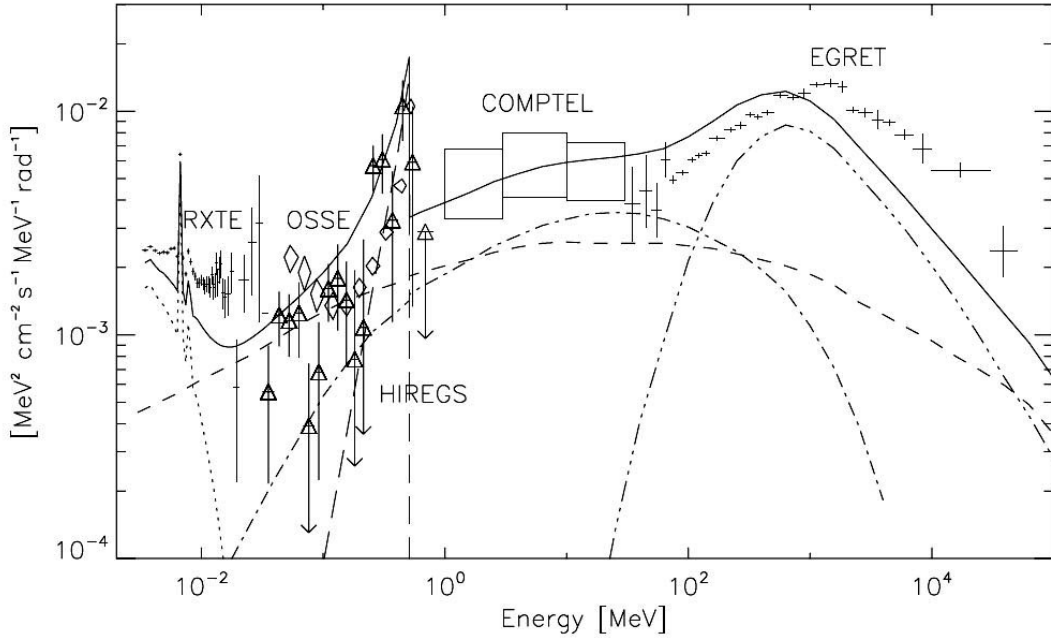


Figure 1.7: The spectrum of galactic diffuse gamma-ray [7]. Also shown is the bremsstrahlung (dot-dashed line), inverse Compton scattering (short-dashed line), and π^0 (triple-dotted line) model, positronium continuum (long-dashed line) and the thermal Raymond-Smith plasma component (dotted line). The total of the model components is also presented (solid line).

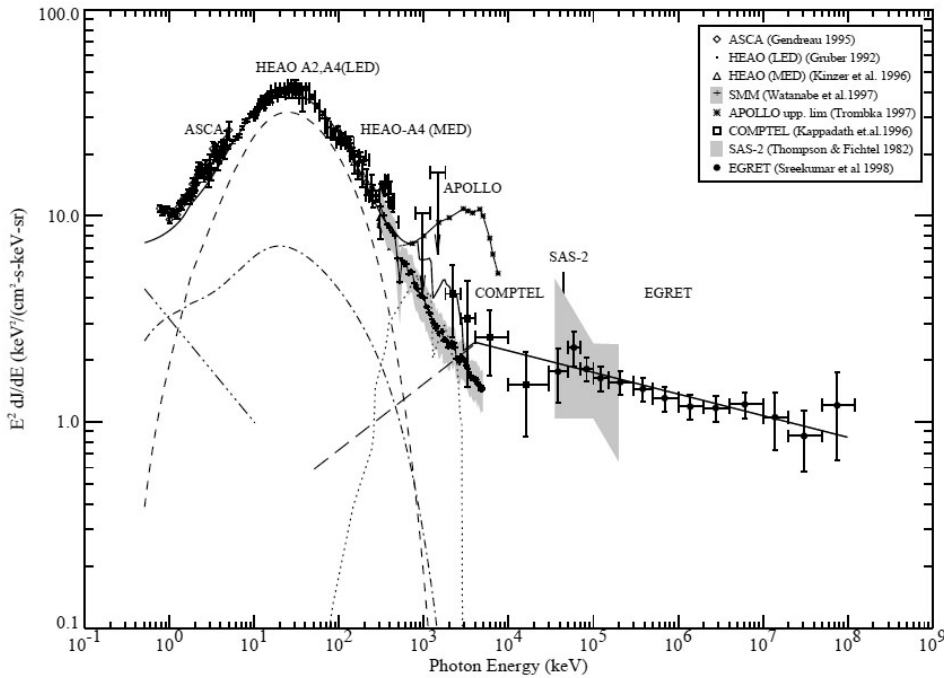


Figure 1.8: The spectrum of extragalactic diffuse gamma-ray [8]. The dot-dashed line and dashed line are estimated contributions from Seyfert I and Seyfert II, respectively. The triple dot-dashed line is step-spectrum quasar contribution, and the dotted line is Type Ia supernovae. Also the long dashed line is a possible blazar contribution assuming an average power law index of -1.7 below 4 MeV and -2.15 at higher energies. The solid line indicates the sum of all components.

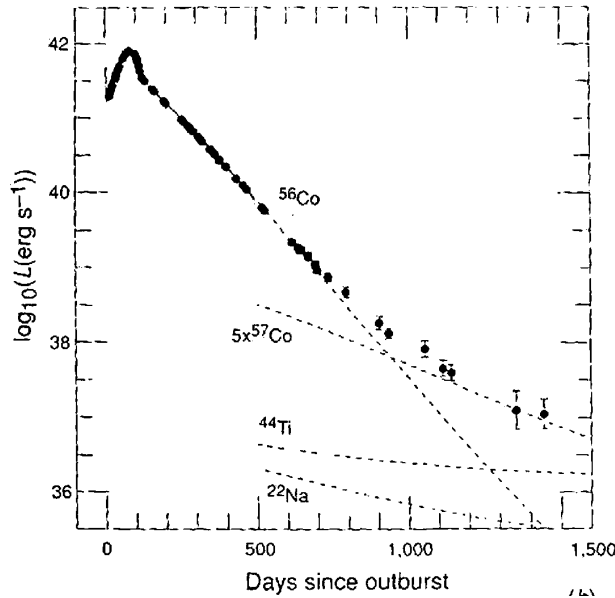


Figure 1.9: The light curve of SN1987A (infrared - ultraviolet) [9]

1.3 Source of Gamma-Rays

1.3.1 Supernova Remnant

The supernova is an important site of the nucleosynthesis, and is considered to create the heavier nuclei than Fe. In the nucleosynthesis process in the supernova explosion, the radio isotopes are also produced, and hence the gamma-ray emission by the decay of those isotopes is a good probe to investigate the nucleosynthesis.

If a binary includes a white dwarf, the material from a companion star gradually accretes onto the white dwarf. Then it makes the pressure in the core of the white dwarf higher. Eventually the white dwarf explodes with the thermonuclear supernova explosion (type Ia supernova). In the type Ia supernova, ^{56}Ni is expected to be produced of which amount is predicted about $0.6 M_{\odot}$, and after the explosion ^{56}Ni decays such as:



The light curve of the type Ia supernova is well explained by the combination of the decay time of those nuclear transitions. In the type II supernova, which is the gravitational collapse of the iron core as the final stage of the stellar evolution of the stars more massive than about $8 - 10 M_{\odot}$, ^{56}Ni is also produced, although the amount is less than that of a type Ia supernova. Figure 1.9 shows the light curve of SN1987A, which is explained by the decay time of ^{56}Co practically. Also the gamma-ray emission due to the ^{56}Co decay was observed from SN1987A.

In the supernova explosion, a lot of neutrons are ejected from the core, the nuclei of the outer shell rapidly capture the neutrons before the transition to a stable states, and changes to neutron-rich isotopes. Since such nuclei are so unstable, they transmit to the stable nuclei through β -decays. This process rapidly proceeds, which are called r-process. The existence of the isotopes in Table 1.1 has been observed in the supernova remnants so far.

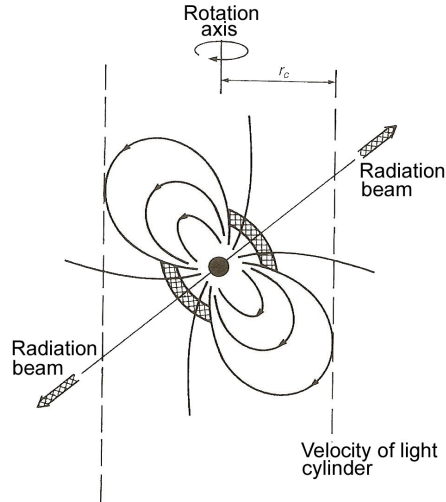


Figure 1.10: The schematic view of pulsar [10]

1.3.2 Spin-Down Pulsars

Gamma-Ray Pulsars

Pulsars radiate a short periodic pulse, and hence are considered to be neutron stars spinning with a high speed. A neutron star also has a strong magnetic field of about 10^{12} G. Because the magnetic axis inlines to the rotation axis generally, as shown in Figure 1.10, the emission near the magnetic poles sweeps around the rotation axis. Since the emission region of the pulsar rotating around the axis is observed from the earth, we see it like a light house. Within thousand pulsars observed so far, the emission of gamma-rays are only observed from several of them (Table 1.2). The multiwave spectra of the gamma-ray pulsars are presented in Figure 1.11.

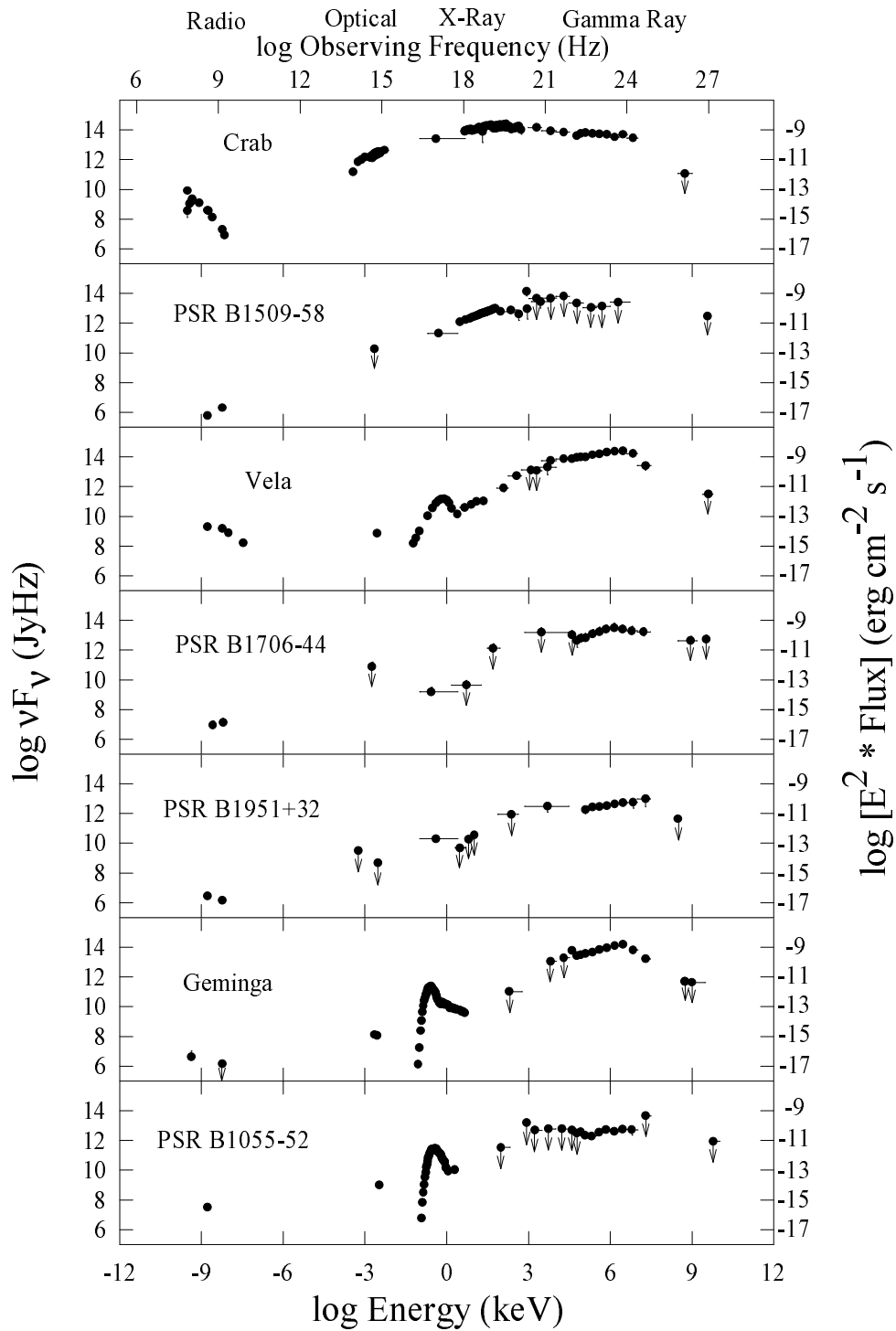
Table 1.2: Gamma-ray Pulsars [5]

Pulsar	Period P [msec]	\dot{P} [10^{-15}]	distance d [kpc]
Crab	33.34	421.2	2.0
PSR B1509-58	150.65	1537	4.4
Vela	89.29	124.3	0.5
PSR B1706-44	102.4	93.0	1.8
PSR B1951+32	39.53	5.849	2.5
Geminga	237.1	10.98	0.16
PSR B1055-32	197.1	5.8	1.5

Especially, the Crab pulsar was observed from the radio to the GeV gamma-ray, and it is one of the most famous pulsars. Figure 1.12 are light curves in each energy region. These figures say that the sub MeV to the MeV energy bands have 2 features:

- Although the first peak is dominant in other energy bands, the dominant in this band varies to the second peak.
- The pulse profile has the ‘Bridge’ structure between the first and the second peak.

The study of the emission from the pulsar is still underway, and these features in the MeV band have not been explained.



DJT, May, 1998

Figure 1.11: The spectra of gamma-ray pulsars [11]

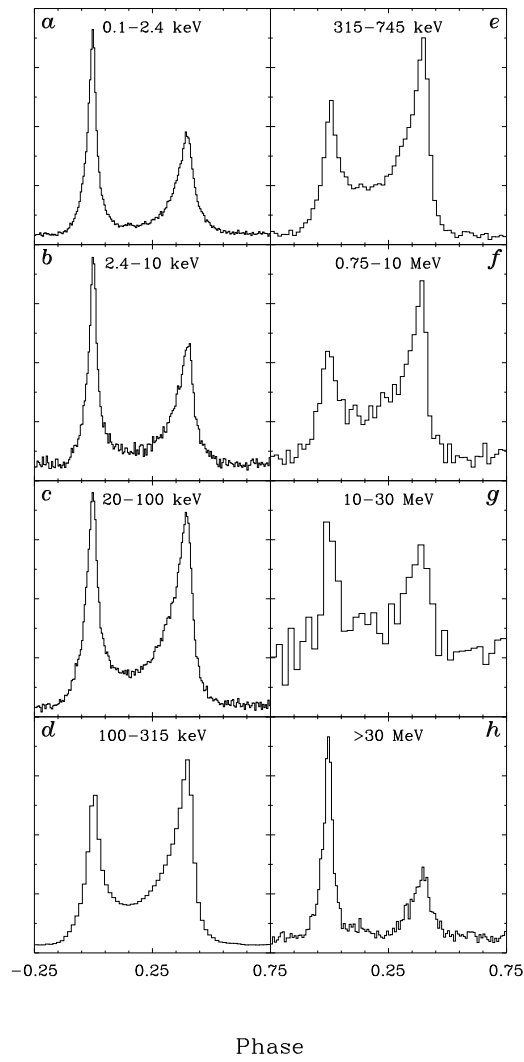


Figure 1.12: The pulse profile of crab pulsar [12]

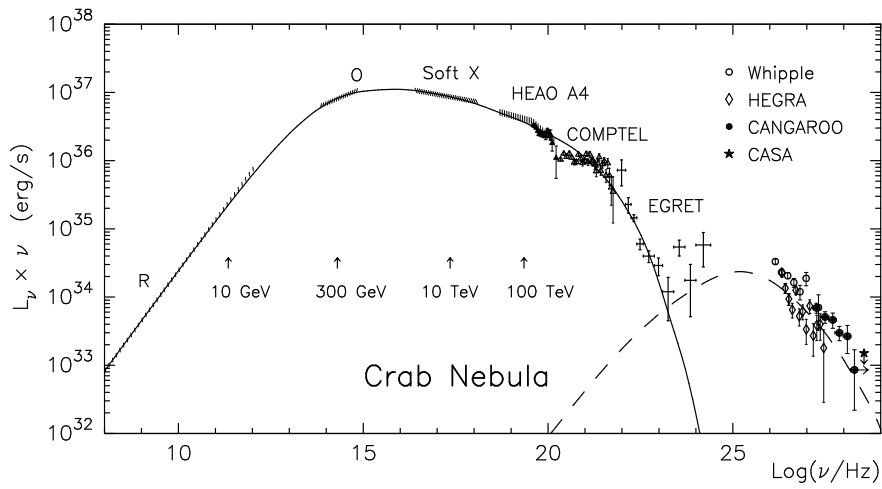


Figure 1.13: The spectrum of crab nebula (solid line: synchrotron radiation, dashed line: inverse Compton scattering) [13]

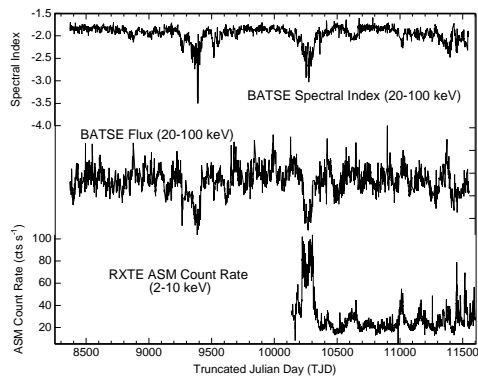


Figure 1.14: The light curve of Cyg X-1 [14]

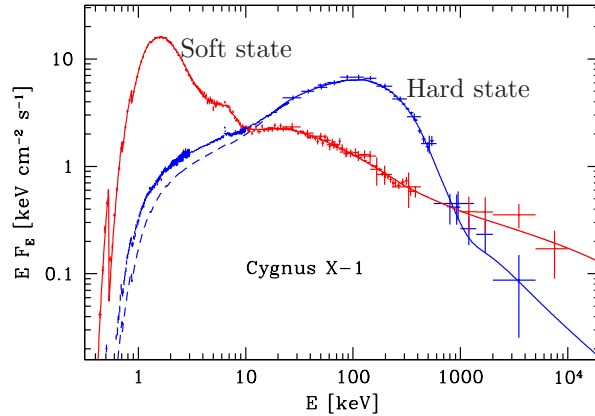


Figure 1.15: The spectra in Soft state and Hard state (Cyg X-1) [14]

Pulsar Nebula

Crab pulsar has a nebula around it. The nebula is observed from the radio to the TeV gamma-ray as a non-pulsed emission. Figure 1.13 shows the multi-wave spectrum of the Crab nebula. The spectrum is explained by the combination of synchrotron radiation and inverse Compton scattering. Also in the MeV band, the emission from the Crab nebula was observed by COMPTEL and OSSE, and it is suggested that the emission is due to synchrotron radiation.

1.3.3 Black Hole

In the final evolution of a heavy star with a mass above $30M_{\odot}$, the core is considered to collapse to a black hole after a type II supernova. A black hole has a boundary line, which is called ‘event horizon’, from where the electromagnetic wave can’t escape. However if a black hole makes a binary system with a star, an accretion disk is created similar to the white dwarf because the matter from the companion star flows onto the black hole. This accretion disk radiates photons in wide band including X-rays and gamma-rays. Until now, there is no solid evidence for the existence of a black hole.

Although the existence of the black hole is not established, there are several ‘black hole candidates’, which are inferred with its mass and the size. Cygnus X-1 is the most prominent black hole candidate. Those black hole candidates commonly indicate a violent time profile, as shown in Figure 1.14. Another feature of the time variability is that the energy spectrum changes suddenly between Soft state and Hard State at time. Figure 1.15 shows the spectra of the Soft/Hard state of Cyg X-1.

The emission model of the Soft state is depicted in Figure 1.16, and the model of the Hard state in Figure 1.17. In the soft state, the disk is bright in the X-ray region, in which the blackbody radiation from the accretion disk and the Compton scattering by the non-thermal electron are dominant in this state. On the other hand, the hard state has a peak at a few hundred keV, and the dominant component is the Compton scattering by the thermal electron. In addition, both states look to have the component of Compton reflection with the cold disk [14].

Near the event horizon, ions accelerate up to 100 MeV by the strong gravitational potential, and hence surely π^0 must be created. Therefore, a thermal radiation of π^0 , which makes a peak at 70 MeV, is expected to be observed. Such radiation may be an evidence for the existence of black hole.

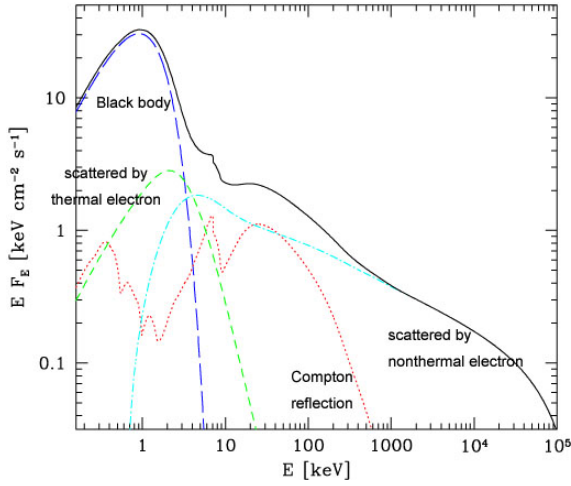


Figure 1.16: The emission model of Soft(High) State [14]

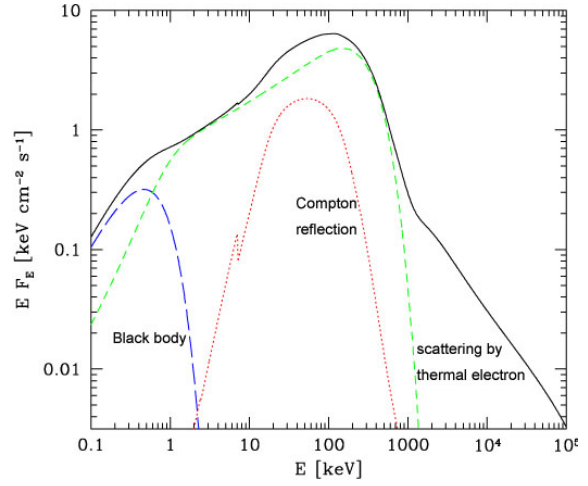


Figure 1.17: The emission model of Hard (Low) State [14]

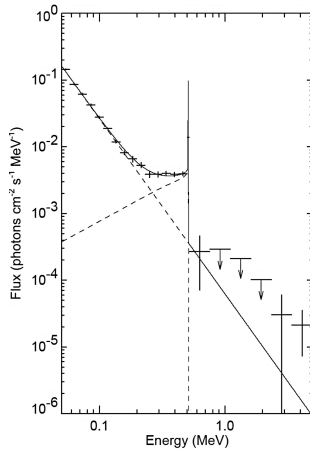


Figure 1.18: The spectrum of Galactic Center by OSSE [15]

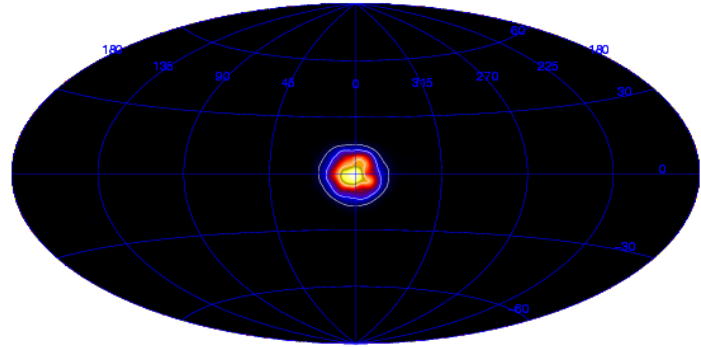


Figure 1.19: The map of Galactic Center at 511 keV by SPI/INTEGRAL [16]

1.3.4 Galactic Center

When an electron meets a positron, two or three gamma-rays are produced by the annihilation. When the annihilation occurs at rest, the photon energy is 511 keV equal to the rest energy of an electron (section 1.1.5). Actually, OSSE observed the 511 keV from the Galactic Center in Figure 1.18, which says that the annihilation in the Galactic Center exists certainly.

The distribution of 511 keV was broad in the Galactic Plane. The 511 keV emission means the existence of the positron, and the positrons are produced by the β^+ decay of radioactive isotopes, which are provided by the nucleosynthesis in the supernovae and heavy stars.

At the Galactic Center, the existence of a black hole with the mass of $\sim 3 \times 10^6 M_\odot$ is strongly considered [17]. Therefore, if there is a mass accretion, the MeV gamma-ray radiation due to π^0 decay is also expected.

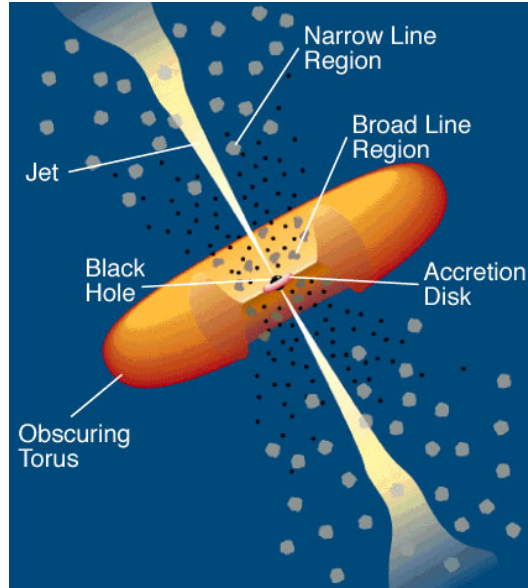


Figure 1.20: The schematic view of AGN [18]

1.3.5 Active Galactic Nuclei (AGN)

The Active Galaxy is a galaxy with the strong emission from its nuclei, and the nuclei of such a galaxy is called Active Galactic Nuclei. At the Active Galactic Nuclei, the existence of a black hole with the mass of $10^6 - 10^9 M_{\odot}$ is considered. Figure 1.20 shows the schematic view of AGN. Radio wave observation indicates that many AGN have jets, which is emitted with a narrow beam from the center. If the radiation from the jets is stronger than the radiation from the accretion disk or the thermal radiation of the near disk, the obtained multiwave spectrum is explained by the combination of synchrotron radiation and inverse Compton scattering (Figure 1.21, 1.22).

There are 10 AGNs detected by COMPTEL and 94 AGNs by EGRET, respectively. Thus, AGNs are also the important observable sources in the sub-MeV/MeV gamma-ray bands.

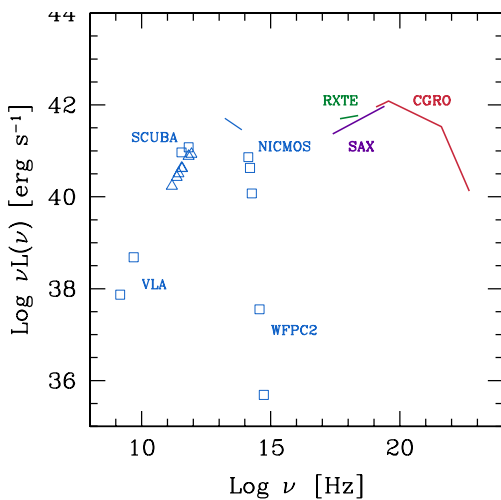


Figure 1.21: The multiwave spectrum of Centaurus A [19]

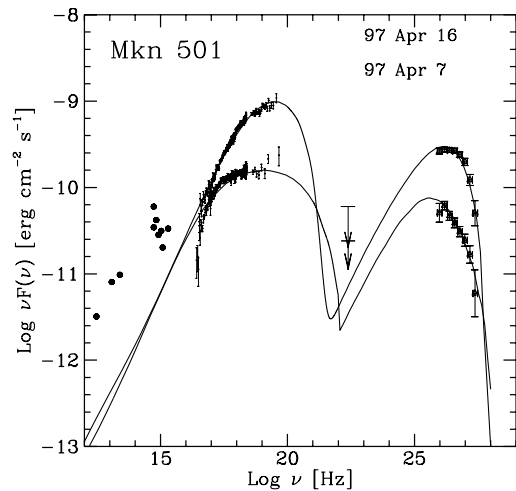


Figure 1.22: The Spectrum of Blazar Mkn501 [20]

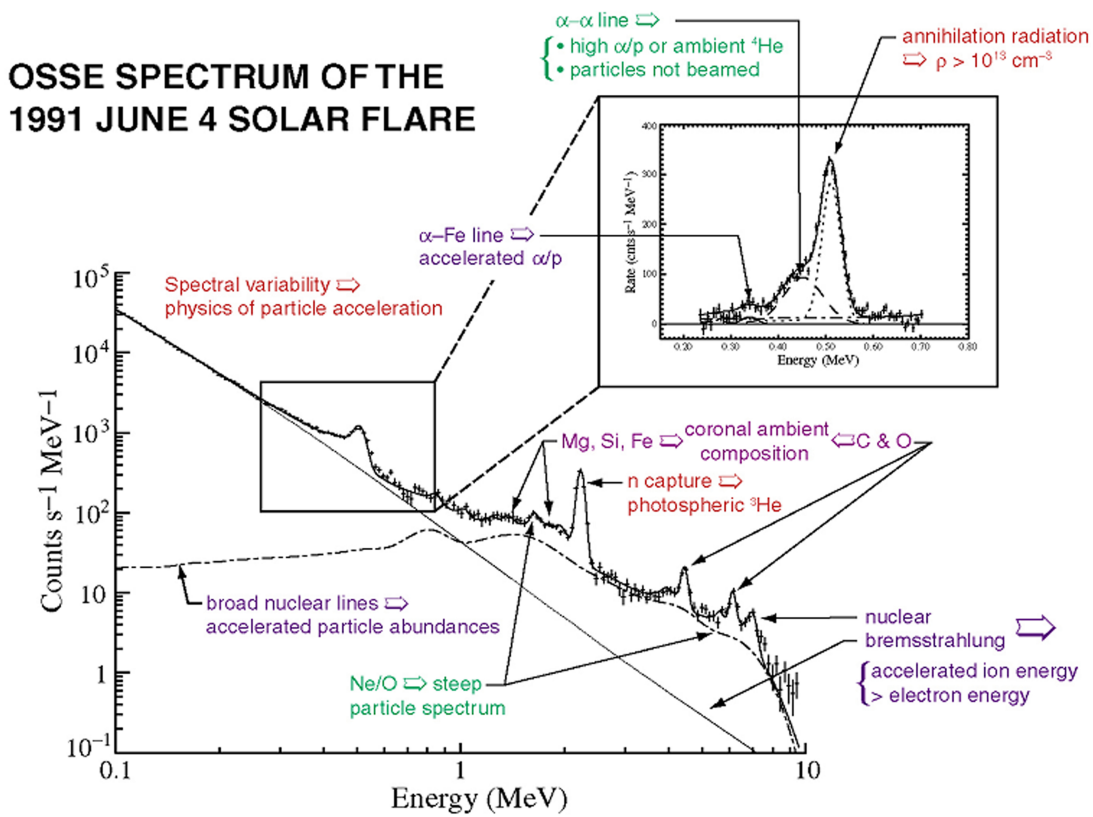


Figure 1.23: The spectrum of Solar Flare (June 4, 1991) [21]

1.3.6 Solar Flare

The Sun, the most familiar celestial object, also radiates gamma-rays. From 1970's, a few line gamma-rays have been known to be emitted in the solar flare sometimes.

Figure 1.23 shows the spectrum of the solar flare. By these measurements, many of the neutron and positron are expected to be produced in the region of flare. Moreover, by the acceleration and the heating of the particles in the corona at the time of solar flare, the accelerated electrons emit X/gamma-ray with bremsstrahlung. Because the Sun is the nearest star, it is the most detailed observable star and is a very important gamma-ray source.

1.3.7 Gamma-Ray Burst

The Gamma-Ray Burst (GRB) was discovered by the Vela satellite in early 1970's. It is a transient phenomenon that gamma-rays arrival from specified direction suddenly. GRB has a violent time profile, and the bursting time is very short, but spread in several orders (Figure 1.24).

Until now, many observations such as HETE-2 and SWIFT have been carried out, and our understanding for GRB is dramatically recovered: GRB is a very giant burst at the distance of cosmology, and GRB has a mother galaxy. The obtained spectrum can be explained with synchrotron radiation, in MeV gamma-ray (Figure 1.25). BATSE on CGRO discovered 2700 GRBs, and the distribution is flat in the all sky (Figure 1.26). But GRB is a puzzle, that is not understood of even the central engine until now.

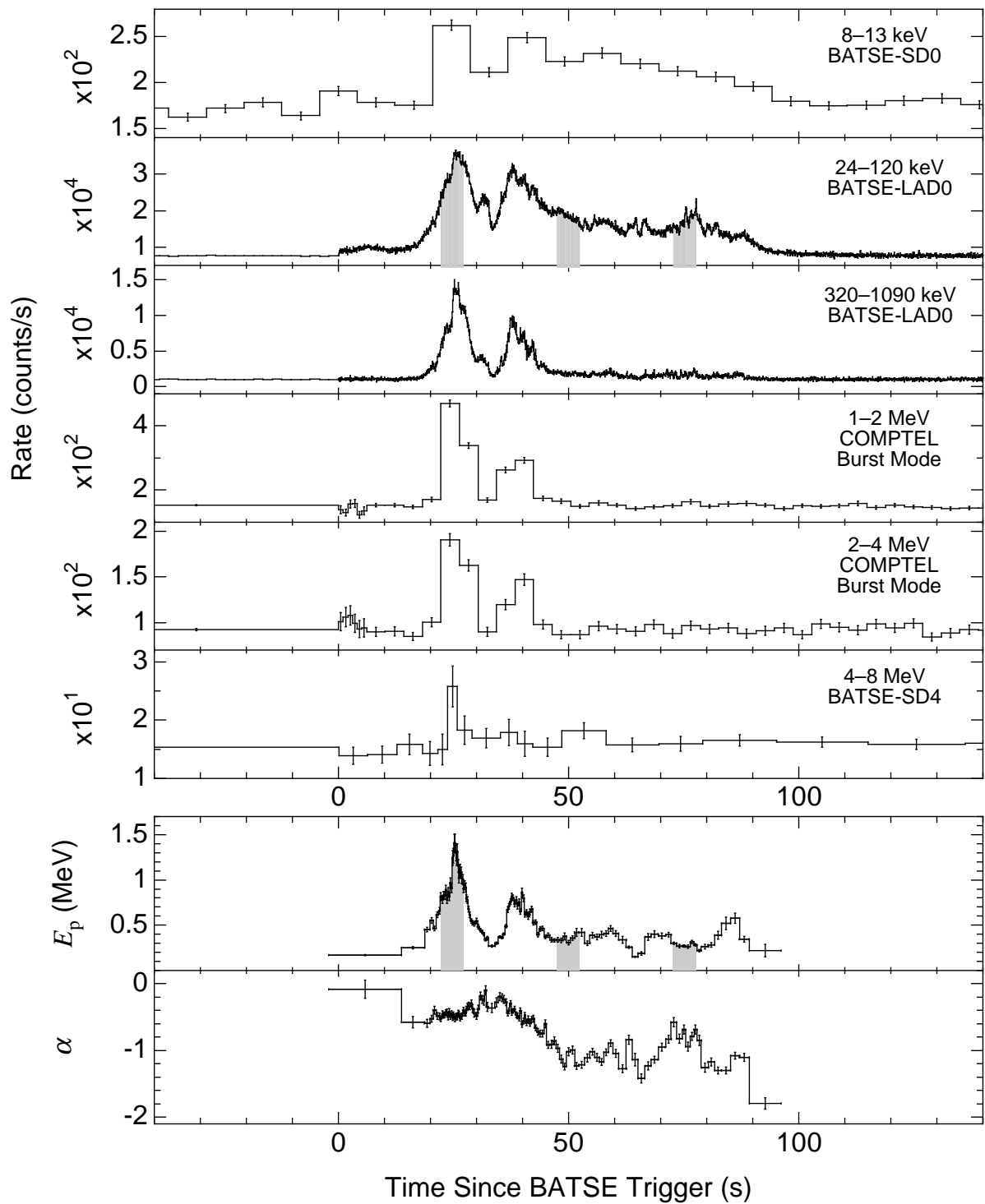


Figure 1.24: light curve of GRB by BATSE and COMPTEL [22]

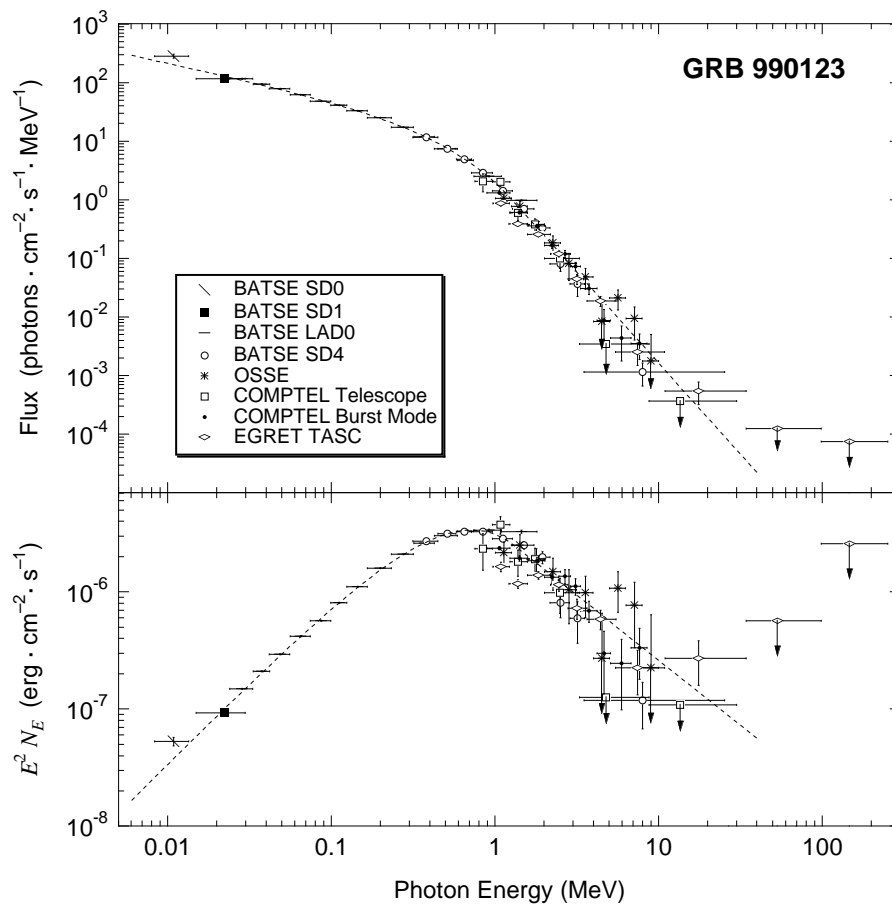


Figure 1.25: The spectrum of GRB [22]

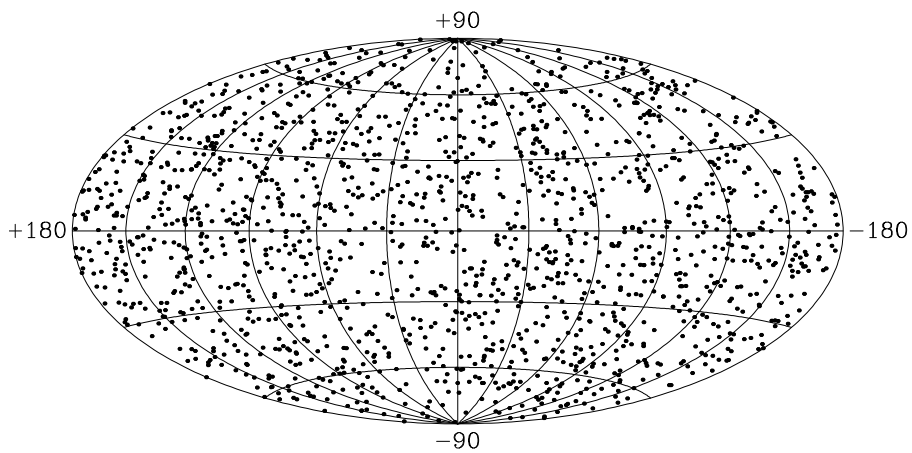


Figure 1.26: The all sky map of GRB by BATSE [23]

Chapter 2

Detection of Gamma-Rays

2.1 Interaction of Gamma-Rays and Matter

Because photons are electrically neutral, they can't ionize the material. However, once high energy photons interact with material, an electron is emitted via several processes depending on their energy. The ionization of the surrounding material by such an electron enables us to detect X-rays and gamma-ray.

There are three processes in the interaction between X/gamma-rays and the matter: photoelectric absorption, Compton scattering and pair creation. The cross sections of these interactions depend on the energy of X/gamma-rays and the atomic number Z of the matter. Figure 2.1 shows each cross-section of the interaction with Argon, and Figure 2.2 shows which interaction is dominant.

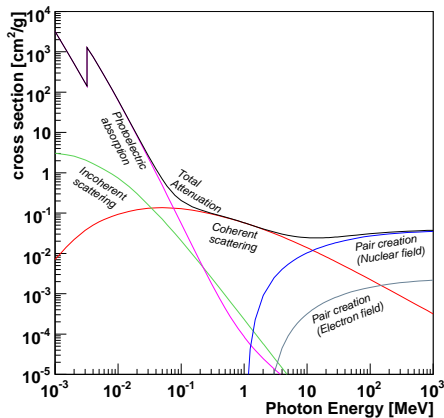


Figure 2.1: The cross-section of the interaction of gamma-rays and matter (Argon) [24]

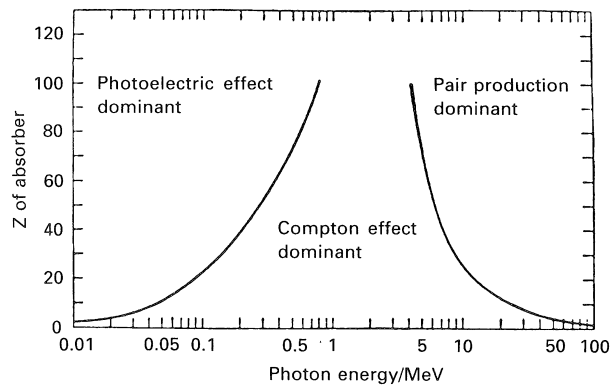


Figure 2.2: The significant interaction of gamma-rays and matter [25]

2.1.1 Photoelectric Absorption

The photoelectric absorption is a dominant interaction of photons with the energy less than 100 keV. In this process, a photon provides all energy to a electron in the atom, and then this electron, called photoelectron, is ejected from the atom. When a photon of the energy E_0 makes a photoelectron, the kinetic energy of the photoelectron is as follows,

$$K_e = E_0 - E_{\text{bind}}, \tag{2.1}$$

where E_{bind} is the binding energy of the photoelectron in the atom. If E_0 is higher than the binding energy of the K shell, the probability of the interaction with an electron in K shell is highest. Then the cross section of the photoelectric absorption of a K shell electron is:

$$\sigma_K = 4\sqrt{2}Z^5 \left(\frac{8\pi}{3}r_e^2\right) \left(\frac{e^2}{4\pi\epsilon_0\hbar c}\right)^4 \left(\frac{m_e c^2}{E_0}\right)^{7/2}, \quad (2.2)$$

where σ_K is proportional to Z^5 and $E_0^{-7/2}$, and r_e is the classical electron radius: $r_e = \frac{e^2}{4\pi\epsilon_0 m_e c^2}$. If E_0 is less than the binding energy of K shell, the photon interacts with an L shell electron. Therefore, near the K shell binding energy, the energy dependence of the cross section has a large discontinuity edge (Figure 2.1). Simultaneously a binding electron in the higher energy level trends to transit to the empty level by an emitting X-ray. The energy of the emitted X-ray is equal to the energy difference of those two levels. Also sometimes an electron of the nearly same energy is ejected instead of the X-ray emission, which is called Auger electron.

2.1.2 Compton Scattering

In the energy band from a few hundred keV to 10 MeV, the dominant interaction is the Compton scattering, which is an elastic scattering of a gamma-ray and an electron. When a gamma-ray makes Compton scattering, the gamma-ray provides a part of the initial energy to an electron, then the recoil electron runs away, and simultaneously the gamma-ray is scattered as its energy becomes lower. When the gamma-ray in the energy of E_0 makes Compton scattering with a free electron, the energy of the scattered gamma-ray is

$$E' = \frac{E_0}{1 + \frac{E_0}{m_e c^2}(1 - \cos \phi)}, \quad (2.3)$$

and the energy of the recoil electron is

$$K_e = E_0 - E' = \frac{\frac{E_0}{m_e c^2}(1 - \cos \phi)}{1 + \frac{E_0}{m_e c^2}(1 - \cos \phi)} E_0, \quad (2.4)$$

where ϕ is a scattering angle. The angular distribution of the scattered gamma-rays is represented by the differential scattering cross section as follows,

$$\frac{d\sigma}{d\Omega} = Zr_e^2 \left(\frac{1}{1 + k(1 - \cos \phi)}\right)^2 \left(\frac{1 + \cos^2 \phi}{2}\right) \left(1 + \frac{k^2(1 - \cos \phi)^2}{(1 + \cos^2 \phi)[1 + k(1 - \cos \phi)]}\right), \quad (2.5)$$

where σ is the cross section, Ω is the solid angle and $k = \frac{E_0}{m_e c^2}$. Then the cross section is proportional to Z . The angular distribution is shown in Figure 2.3, where you note that the forward scattering is dominant when E_0 is higher.

In a real detector, electrons do not rest and they have the finite momentum of the orbit. Therefore, the gamma-ray scattered at the fixed angle from a monoenergetic source have some fluctuation in their energy (the ‘‘Doppler broadening’’, see section 3.3).

2.1.3 Pair Creation

If the gamma-ray energy exceeds twice of the rest mass of the electron, a pair of an electron and a positron are created with the interaction between the photon and an electric field around the nucleus. This process is called a pair creation, which is a dominant interaction of the photons above 10 MeV. The energies of an electron and a positron emitted from the photon of the energy E_0 must be satisfied with the following equation,

$$E_0 = E_- + E_+ + 2m_e c^2. \quad (2.6)$$

The cross section is proportional to Z^2 .

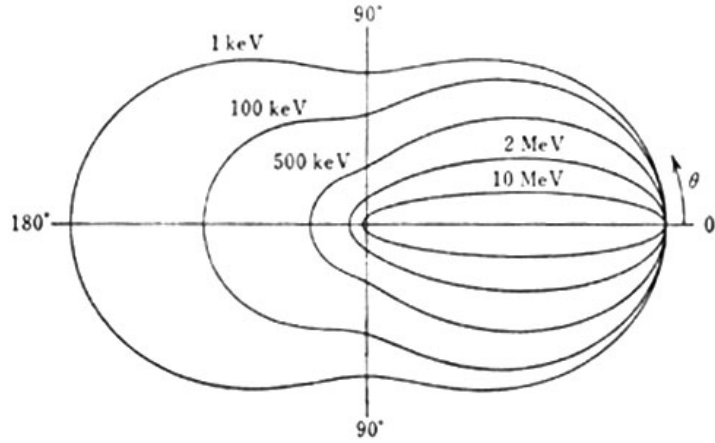


Figure 2.3: The angular distribution of Compton scattering [25]

2.2 Sub-MeV/MeV Gamma-Ray Imaging

In general astronomy, it requires both measurements of the energy and the incident direction of photon for imaging. For the X-ray imaging, the photons can be focused by reflection. Figure 2.4 is a schematic view of an X-ray focusing. Only when an X-ray comes to the mirror at a very shallow angle, the X-ray makes reflection. The mirror is Al or glass coated by Au generally. Because the focusing is a mapping from the direction to the position, we can get the energy and the incident direction of each photon at the same time using a 2-dimensional position sensitive detector on the focal plane. However the limit of the energy in focusing by reflection is order of

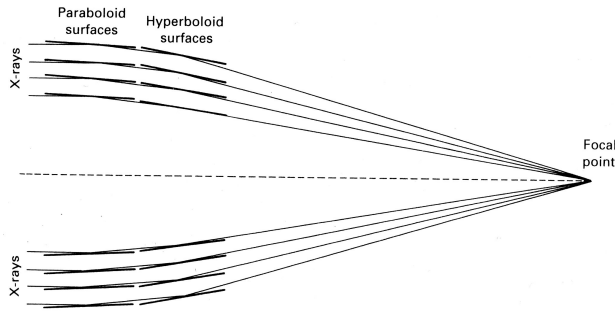


Figure 2.4: The schematic view of an X-ray focusing [26]

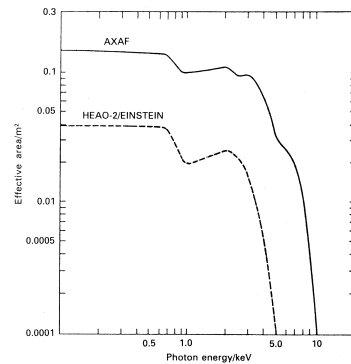


Figure 2.5: The effective area of X-ray telescopes [26]

10 keV, and the reflection ratio falls suddenly in the higher energy (Figure 2.5). For this reason, the focusing of sub-MeV/MeV gamma-rays by reflection is impossible, and the other techniques are necessary.

On the other hand, around a satellite, lots of MeV gamma-rays are generated by the excitation of the nuclei in the material of the satellite by the cosmic-rays, and furthermore such a MeV gamma-ray is scattered several times by Compton process. Therefore, the observations of the MeV gamma-rays in space severely suffer from huge background gamma-rays.

2.2.1 Active and Passive Collimators

For getting the incident direction of a photon, the simplest method is the collimation of the Field Of View (FOV). The camera consists of a position sensitive detector and collimators, as shown in Figure 2.6. By collimators, the detected photons are expected to come from the inside of FOV of the collimator. However, for higher energy photons, some photons are scattered in the collimator or come through the collimator. Thus, gamma-rays sources outside of FOV make many background, and obstruct the detection of a faint source in FOV.

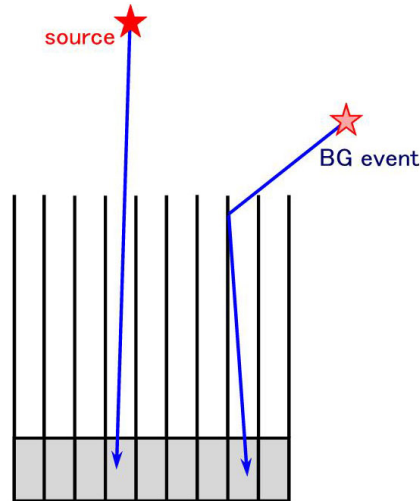


Figure 2.6: The schematic view of passive collimator

For surely rejecting gamma-rays from the outside of FOV, there are two possible improvements. One is the simple method: using a thicker collimator. The collimator becomes thicker, the higher stopping power the collimator has. But, in this way, FOV is narrower, effective area is smaller and the collimator is heavier. Because the observations of MeV gamma-ray in astronomy require the measurements on the satellite-borne or balloon-borne, these deprivations make large demerits for the actual detector-construction. The other way is using an active collimator. For the rejection of the reaction in the collimator, a veto-counter having sensitivity for gamma-rays, like a high- Z scintillator, is useful. The background events, scattering in the collimator, can be rejected by the anti-coincidence of the veto-counter. On the other hand, the camera may become more sensitive for intrinsic background and the dead time of the measurement may increase. Therefore, the observation with collimator is not so sophisticated but quite simple and conventional in astronomy.

Until now, OSO-3, SMM and OSSE were based on this method, and HXD loaded on Suzaku is also a telescope of this kind.

2.2.2 Coded Aperture Imaging

Now, the practical imaging method is the Coded Aperture Imaging, which was adopted in SIGMA, INTEGRAL and SWIFT. The detector of coded aperture imaging consists of a position sensitive detector and a coded mask which carries out a mapping from the incident direction to the image of the mask's shadow. The coded mask consists of the optical thin material and the optical thick material, and the mask can be described with a matrix:

$$M_{ij} = \begin{cases} 1 & \text{: the optical thin part,} \\ 0 & \text{: the optical thick part.} \end{cases} \quad (2.7)$$

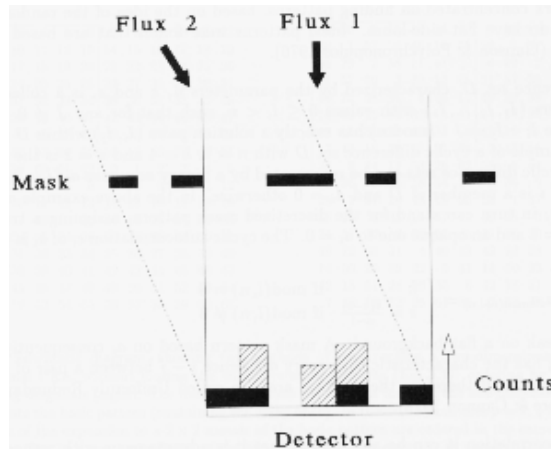


Figure 2.7: Coded mask [27]

When the gamma-rays come from the direction of j with the intensity of s_j , the direction is projected to the image of mask's shadow, and the photon number of $M_{ij}s_j$ arrive to the detector of the position i , as shown in Figure 2.7. Therefore, in the detector of position i , the detected photon number is:

$$d_i = \sum_j M_{ij}s_j + b_i, \quad (2.8)$$

where b_i is the number of the background photons detected in the position i , because the photons from the outside of FOV is the background. Although the incident direction s_j is obtained by resolving this formula, there are two unknown parameters of s_j and b_i , so that the estimation of background is very important.

The angular resolution and the FOV depend on the distance between the coded mask and the detector. For the same mask and the same detector, the camera has a larger FOV in the shorter distance of them, while it has a better angular resolution in the longer distance. IBIS loaded on INTEGRAL used the full coded FOV of $9^\circ \times 9^\circ$ and obtained the angular resolution of 0.2° in FWHM [1].

The coded mask is a kind of a collimator, and it is expected that the mask ideally absorbs the gamma-ray completely. But, because the cross section of the photoelectric absorption is decreased in proportion to $E^{-7/2}$, the Coded Aperture Imaging is not so good for the imaging of the high energy photons basically. The imaging of high energy photons is required of the thicker mask. Actually, the mask of IBIS (20 keV - 10 MeV; INTEGRAL) is made of a 1.6 cm thick tungsten plate, and SPI (3 keV - 8 MeV; INTEGRAL) has a 3 cm thick tungsten mask. Still, there remains another problem, that gamma-rays scattered in the mask are detected as background.

2.2.3 Gamma-Ray Lenses

Although gamma-rays can't be focused by reflection, there are two focusing methods for MeV gamma-rays. These focusing methods are called Gamma-Ray Lenses. One makes use of Laue diffraction, and the other makes use of a phase Fresnel lens. Generally, the focusing has the high angular resolution, but the FOV is narrow. Besides, the focusing can reduce the intrinsic background, because the detection volume is quite smaller than other imaging methods.

Laue Lenses

The focusing by Laue diffraction is called Laue lens. Although the Laue lenses give us a very good angular resolution, they focus only the gamma-ray of specific energy due to the principle of the Bragg scattering as follows,

$$2d \sin \theta = n\lambda. \quad (2.9)$$

Then it is impossible to get the wide band energy spectrum using this lens. Here d is the crystal plane spacing, θ is the diffraction angle, n is the reflection order and λ is the wavelength. The lens of CLAIRE, which was launched in the balloon experiment in 2001, has the FOV of $45''$, the energy band of 169 - 171 keV and the focal length 3 m [28].

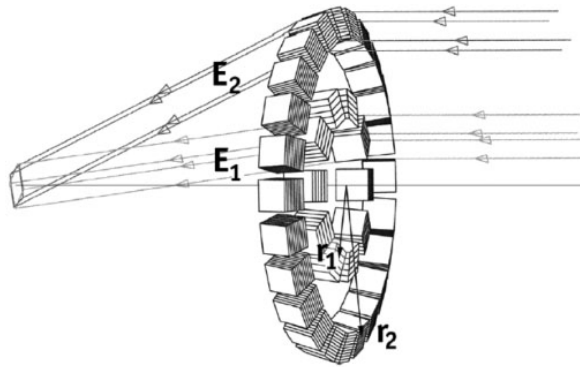


Figure 2.8: The schematic view of Laue Lens [29]

Fresnel Lenses

The other method is a phase Fresnel lens. Because the refraction index for gamma-ray in matter is slightly lower than 1, it is possible to focus gamma-ray. The Fresnel lenses have the angular resolution limit in the μarcsec , but they require a very long focal length of 10^9 m. Therefore it is difficult to realize this method currently.

2.2.4 Compton Imaging

When the gamma-ray makes Compton scattering in a detector, it is hard to detect the total photon energy because the scattered gamma-ray brings out some part of the incident photon energy. Then, the Compton scattering is a hard process in an usual detector, although it is the most dominant interaction in the sub-MeV and MeV energy regions.

If the information of both the scattered gamma-ray and the recoil electron are detected, the energy and the direction of the incident gamma-ray can be reconstructed. This imaging method is called ‘‘Compton Imaging’’. The detector based on Compton imaging has a large FOV because no collimator is required. In actual, COMPTEL loaded on CGRO had a FOV of 1 steradian [30].

Compton imaging is an unique imaging method to detect both the energy and the direction for photon by photon, in the sub-MeV/MeV band. Therefore this imaging is an attractive method, and many detectors are in development: MEGA, NCT, LXeGRIT, TIGRE and so on.

Classical Compton Imaging

The Classical Compton Imaging used in COMPTEL makes use of the first Compton scattering in the material. A classical Compton imaging camera consists of two Z detectors of which materials are light (low- Z) and heavy (high- Z), respectively. A low- Z position sensitive detector is placed forward, and a high- Z position sensitive detector is placed backward. Figure 2.9 is a schematic view of a classical Compton imaging camera. An incident gamma-ray makes a Compton scattering in the low- Z detector, and the scattered gamma-rays are absorbed in the high- Z detector. From these detectors, the following information are measured,

- the low- Z detector: the recoil electron energy E_1 , and the Compton Point (scattering point)
- the high- Z detector: the scattered gamma-ray energy E_2 , and the absorption point of the scattered gamma-ray

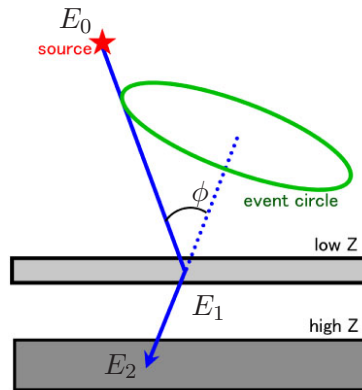


Figure 2.9: The schematic view of Classical Compton Imaging

Then, using E_1 and E_2 , the incident gamma-ray energy E_0 and the scattering angle ϕ are calculated

$$E_0 = E_1 + E_2, \quad (2.10)$$

$$\cos \phi = 1 - m_e c^2 \left(\frac{1}{E_2} - \frac{1}{E_1 + E_2} \right). \quad (2.11)$$

The direction of the scattering gamma-ray is also obtained by connecting the Compton point and the absorption point, although the two parameters of the direction of the recoil electron is not measured. Therefore the reconstructed direction of the incident gamma-ray is limited in a circle (called an event circle as shown in Figure 2.9).

For getting the direction of the gamma-rays source, the detector requires at least 3 photons, as shown in Figure 2.10, where the source position is determined fully by piling up circles (the right figure of Figure 2.10). Although COMPTEL rejected background by using the time of flight between the up and down detectors [30], the signal to noise ratio was not high, and FOV is limited.

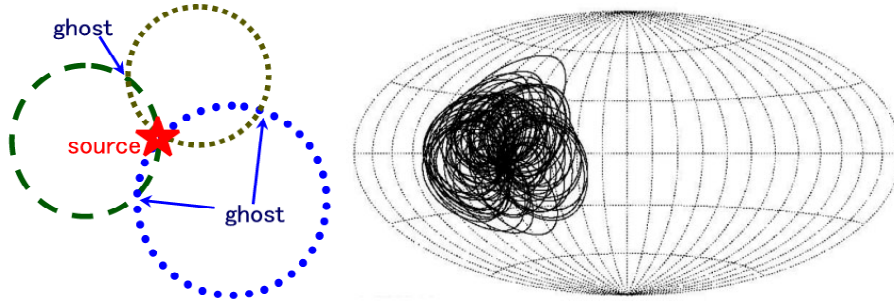


Figure 2.10: The Imaging of Classical Compton and the detection of GRB with COMPTEL (GRB910505 [31])

Multiple Compton Imaging [32]

For the classical Compton imaging, a good process to obtain the correct direction of an incident gamma-ray is one Compton scattering in the forward detector and a perfect photoelectric absorption in the backward detector. However, sometimes the gamma-ray scattered in the forward detector makes also a Compton scattering in the backward detector, and the second scattered gamma-ray escapes. Then such as multiple Compton scattering event becomes background for the classical Compton imaging.

The Multiple Compton Imaging is an advanced method to resolve this problem. Figure 2.11 is a schematic view of a detector for the multiple Compton imaging, and the detector consists of layers of several thin position-sensitive detectors. The semiconductor detectors, such as CdTe or Si/Ge strip detector, are used as a thin detector. When a gamma-ray makes more times Compton scattering in the detector, the incident gamma-ray energy E_0 , the first scattering angle ϕ_1 and the second scattering angle ϕ_2 are absolutely obtained

$$E_0 = E_1 + \frac{E_2 + \sqrt{E_2^2 + \frac{4m_e c^2 E_2}{1 - \cos^2 \phi_2}}}{2}, \quad (2.12)$$

$$\cos \phi_1 = 1 - m_e c^2 \left(\frac{1}{E_2 + E_3} - \frac{1}{E_1 + E_2 + E_3} \right), \quad (2.13)$$

$$\cos \phi_2 = 1 - m_e c^2 \left(\frac{1}{E_3} - \frac{1}{E_2 + E_3} \right). \quad (2.14)$$

where E_1 , E_2 , E_3 are the deposit energies of the first, the second and the third interaction, respectively. These equations say that it can detect the incident gamma-ray energy even if the final scattered gamma-ray escapes from the detector. Also this method may reduce background due to the improvement of the efficiency. On the other hand, the reconstructed direction remains an event circle same as the classical Compton imaging. Besides, in the reconstruction of an event, there is a problem of sorting the detected points in the interaction order.

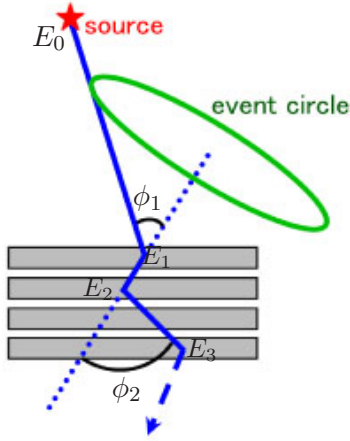


Figure 2.11: The schematic view of a Multiple Compton camera

Nuclear Compton Telescope (NCT) is an example of the multiple Compton imaging. NCT consists of some 3-dimensional position sensitive germanium detectors, and it measured the background of 200 - 800 keV on balloon experiment in 2005 [33].

Electron Tracking Compton Imaging

In comparison to the multiple Compton imaging, which is an improvement method on the energy information, the Electron Tracking Compton Imaging aims to improve the measurement of the direction of the incident gamma-ray. In the classical/multiple Compton imaging, only the energy and the position of the recoil electron is measured, which makes it hard to specify which part of the event circle the gamma-ray comes from.

The camera based on the electron tracking Compton imaging consists of a tracker, which detects the track and energy of the recoil electron, and an absorber, which detects the absorption point and the scattered gamma-ray energy (Figure 2.12). By the detection of the direction of the recoil electron, we obtain the fully ray-traced gamma-ray image.

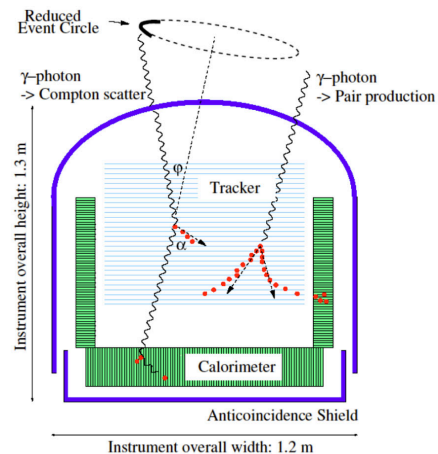
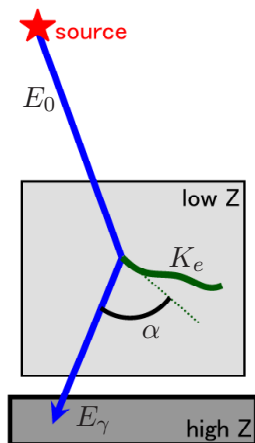


Figure 2.12: The schematic view of an Electron Tracking Compton camera Figure 2.13: The schematic view of MEGA [34]

The angle α between the recoil electron and the scattering gamma-ray is measured for each gamma-ray geometrically, and also this angle is obtained by the calculation using the energy of

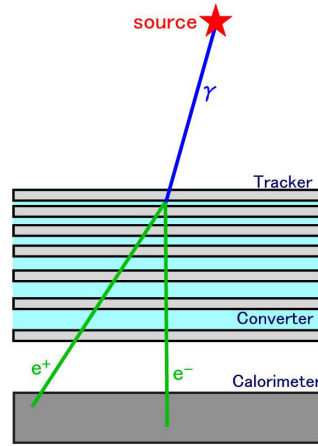


Figure 2.14: The schematic view of pair tracking camera

recoil electron and scattered gamma-ray kinematically. Therefore we can select the good events of which the kinematic calculated angle is consistent with the measured one. Because of the background rejection by the angle α , the electron tracking Compton imaging fits for the MeV gamma-ray astronomy, whose serious problem is the obstruction by background.

Medium Energy Gamma-ray Astronomy (MEGA) is an example of the advanced Compton camera. Figure 2.13 is the schematic view of MEGA. The tracker consists of the stack of the silicon strip detector and the absorber is CsI scintillator. MEGA detects gamma-ray with classical Compton imaging below 2 MeV, with electron tracking Compton imaging in 2 - 8 MeV [34]. But the accuracy of α is low because MEGA uses the solid tracker.

2.2.5 Pair Tracking

Above 10MeV, a pair creation becomes a dominant interaction, and the pair tracking camera consists of a tracker, a converter and a calorimeter, as shown in Figure 2.14. When the gamma-ray comes in the camera, it makes a pair creation in the converter made of the tungsten sheets. The created electron and positron run through the tracker, and stop in the calorimeter. By measuring the tracks in the tracker and deposit energies in the calorimeter, respectively, the momenta of the electron and the positron are measured. Then the momentum of the incident gamma-ray is obtained by the sum of them. SAS-2, COS-B and EGRET were pair tracking telescopes using a spark chamber, and LAT of GLAST is also one of similar detectors using the silicon tracker.

The pair tracking camera is very similar to the advanced Compton camera. In actual, MEGA makes use of pair tracking for the detection of gamma-ray above 8 MeV.

2.2.6 Summary of MeV Gamma-Ray Imaging

I summarize the characters of each sub-MeV/MeV gamma-rays imaging method in Table 2.1. This table says that there is no ‘all-rounder’. Therefore, the selection of suited method for the observation target is required, for example, Laue Lenses fits for observation of the radioactive isotopes distribution in the supernova remnant, Advanced Compton Imaging is suited to the all sky survey.

Table 2.1: The summary of MeV gamma-ray imaging

	with Collimator		Focusing		Compton Imaging		Pair Tracking
	Collimator	Coded Mask	Laue	Fresnel	Classical	Multiple	
energy band	≤ 100 keV	\leq MeV	fixed energy	fixed energy	100 keV - 10 MeV		≥ 100 MeV
true imaging	\circ	\times	\circ	\circ	\times	\times	\circ
limitation for 1 photon	opening angle	can't limit	point	point	circle	circle	point
specify incident direction	\circ	\times	\circ	\circ	\triangle	\triangle	\circ
detect for point source	\triangle	\circ ¶(\triangle †)	\circ	\circ	\triangle	\triangle	\circ
detect for spread source	\times	\times	\circ	\circ	\triangle	\triangle	\circ
field of view	\times	\circ	\times	\times	\circ	\circ	\circ
Angular resolution	\times	\circ	\circ	\circ	\triangle	\triangle	\circ
minimum photon	1	0.5 \times pixel number	1	1	3	3	1
background rejection	\times	\times	\times	\times	\times	\triangle	\triangle
escape event	\times	\times	\times	\times	\times	detect	reject

¶: Full coded, †: Partial coded.

Table 2.2: The properties of some gamma-ray telescopes [1]

Parameter	OSSE	COMPTEL	EGRET	SPI	IBIS
Satellite		Compton Gamma-Ray Observatory			INTEGRAL
Energy range¶	0.1 - 10	1 - 30	20 - 3 $\times 10^4$	0.02 - 8	0.015 - 10
Imaging method	Passive collimator	Classical Compton	Pair Tracking		Coded Mask
Energy resolution	6.8 % @ 1 MeV	6.5 % @ 3 MeV	~ 20 %	2 keV @ 1 MeV	10 % @ 1 MeV
Field of View	3.8° \times 11.4°	1 str			9° \times 9° (19° \times 19°)
Angular resolution		1.25°		2.5°	12 arc min
Narrow-line sensitivity†	2 - 5 $\times 10^{-5}$	0.3 - 3 $\times 10^{-5}$		5 $\times 10^{-6}$ @ 1 MeV	4 $\times 10^{-4}$ @ 1 MeV
Continuum sensitivity‡	2 $\times 10^{-4}$ @ 1 MeV	1.7 $\times 10^{-4}$ @ 1 - 3 MeV	5 $\times 10^{-6}$ @ > 100 MeV	$\sim 10^{-4}$	5 $\times 10^{-4}$
Location accuracy	10 arc min	8.5 arc min	5 - 10 arc min	$\sim 1^\circ$	30 arc sec

 ¶: in unit of MeV, †: 3σ for 10^6 sec and the unit is $\gamma/\text{cm}^2/\text{sec}$, ‡: 3σ for 10^6 sec and the unit is $\gamma/\text{MeV}/\text{cm}^2/\text{sec}$.

2.3 Low Energy Gamma-Ray Observatories

In this section, I briefly summarize several detectors loaded on the satellites for the low energy gamma-ray observation so far.

2.3.1 CGRO

NASA's Compton Gamma-Ray Observatory (CGRO) was operated from April 1991 to June 2000. Its mission was the first all sky survey in the wide energy bands between Sub-MeV and GeV. CGRO had 4 telescopes: OSSE, COMPTEL, EGRET and BATSE. In these instruments, BATSE was a gamma-ray camera for GRB observations. The main properties of OSSE, COMPTEL and EGRET are listed up in Table 2.2, and the detected sources with COMPTEL and EGRET are listed in Table 2.3.

OSSE

The Oriented Scintillation-Spectrometer Experiment (OSSE) used the active and passive collimators. Figure 2.15 shows the schematic view of the one detector of OSSE, in which there were 4 identical detectors on CGRO. The main detector is a phosphor-sandwich (phoswich) detector consisting of the NaI(Tl) crystal (diameter: 33 cm, thickness: 10.2 cm) and the CsI(Na) crystal (thickness of 7.6 cm). In front of the NaI(Tl) crystal, a passive tungsten collimator was mounted. Around the main detector and the tungsten collimator, there was the annular shield of 8.5 cm thick NaI(Tl) crystal for the anticoincidence. For the rejection of charged particles, a thin plastic scintillator (0.6 cm thick) was placed on the collimator. OSSE had an energy range from 0.1 MeV to 10 MeV and had a FOV of $3.8^\circ \times 11.4^\circ$.

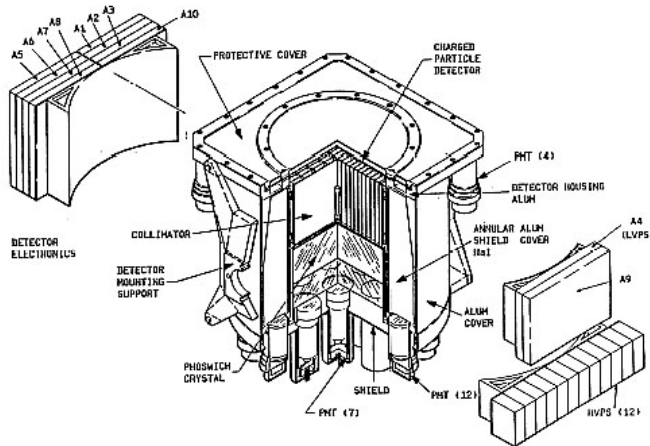


Figure 2.15: The schematic view of OSSE [1]

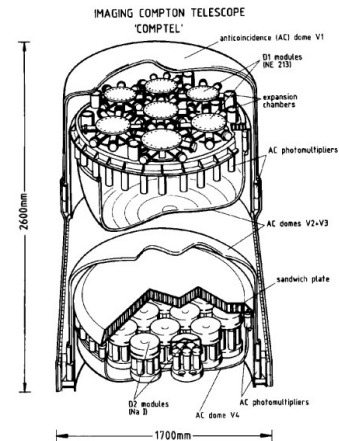


Figure 2.16: The schematic view of COMPTEL [30]

COMPTEL

The COMPTEL was the first Compton telescope launched on a satellite and was based on classical Compton imaging. The schematic view of COMPTEL is shown in Figure 2.16. The low- Z detector of it was a liquid organic scintillator NE213A (geometrical area: 4188 cm^2), and the high- Z detector was a NaI(Tl) crystal (geometrical area: 8744 cm^2). For the rejection of charged particles, each detector was surrounded by an anticoincidence counter dome. For the background rejection, COMPTEL used the time of flight between the low- Z detector and the high- Z detector. COMPTEL had an angular resolution of $\sim 1.25^\circ$ for 10 MeV gamma-ray.

Table 2.3: The detected sources with COMPTEL and EGRET [1, 5]

Type of source	COMPTEL	EGRET
Spin-Down Pulsars	3 Crab, Vela, PSR 1509-58	6 Crab, Vela Geminga, PSR 1786-44, PSR 1055-52, PSR 1951+32
Other Galactic sources $ b < 10^\circ$	7 Cyg X-1, Nova Persei 1992, GRO J1823-12, GRO J2228+61, GRO J0241+6119, Crab Nebula, Carina/Vela region	2 Cen X-3, Crab Nebula
Normal Galaxies		1 LMC
Active Galactic Nuclei	10 Cen A, etc.	77 Cen A, etc.
Gamma-Ray Line Source	7 SN191T (^{56}Co), SNR RX J0852-4642 (^{44}Ti), Cas A (^{44}Ti), Vela (^{26}Al), Carina (^{26}Al), Cyg region (^{26}Al), RE J0317-853 (2.223 MeV)	
Unidentified Sources	5	186
Total Number	32	273
Gamma-Ray Burst	31	4

As shown in Table 2.3, EGRET detected about 270 gamma-ray sources. On the other hand, COMPTEL detected only about 30 steady sources. It seems the reason is that COMPTEL could not reject backgrounds completely by the TOF of both detectors. Therefore, the actual sensitivity of COMPTEL was lower than the design sensitivity.

EGRET

The Energetic Gamma-Ray-Experiment Telescope (EGRET) was based on pair tracking imaging detector. The schematic view of EGRET is shown in Figure 2.17. The central unit of EGRET was a multilevel wire-grid spark chamber with interleaved tantalum conversion layers. The trigger counter consists of the plastic scintillator sheets inserted into the lower part of the spark chamber, and the calorimeter consists of NaI(Tl) crystal with the thickness of 20 cm. For rejection of charged particles, the anticoincidence hood with the 2 cm thick plastic scintillator surrounded the spark chamber.

2.3.2 INTEGRAL

The INTERNational Gamma-Ray Astrophysics Laboratory (INTEGRAL) mission of the ESA was launched in 2002. INTEGRAL has two gamma-ray telescopes: SPI and IBIS, and also has

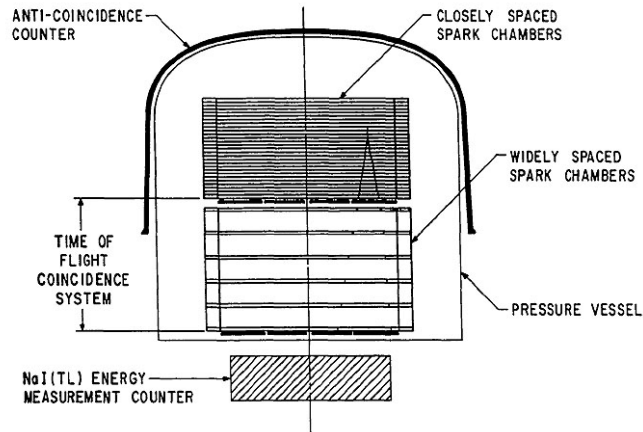


Figure 2.17: The schematic view of EGRET [1]

two additional monitor instruments: JEM-X, an X-ray instrument between 3 keV and 35 keV, and OMC, an optical telescope observing at 500-850 nm. The main properties of SPI and IBIS are listed up in Table 2.2.

SPI

The SPECTrometer on INTEGRAL (SPI) is based on coded aperture imaging. The detector of SPI consists of the array of 19 Ge crystals cooled to 85 K, and thus, SPI has a good energy resolution of 2 keV for 1 MeV. The mask of SPI is made by the 3 cm thick tungsten, and the distance between the mask and the detector is 1.71 m. The whole detector is surrounded by the active BGO shield of mass of 511 kg viewed by 181 PhotoMultiplier Tubes (PMT). Due to the high energy resolution, the SPI's sensitivity for narrow-line gamma-rays is improved at least by a factor of 10 better than other gamma-ray telescopes.

IBIS

The Imager on Board of the INTEGRAL Satellite (IBIS) also uses a coded aperture imaging. The coded mask of IBIS is the 16 mm thick tungsten mask. The detector consists of 2 layers. The lower layer is the array of 4096 CsI scintillators viewed by the silicon PIN photodiodes (each CsI size: $9 \times 9 \times 30 \text{ cm}^3$, total area: 3318 cm^2), named PICsIT. The upper layer is the array of 16384 CdTe pixels (pixel size: $4 \times 4 \times 2 \text{ mm}^3$, total area: 2621 cm^2), named ISGRI. ISGRI detects from 15 keV to 400 keV, and PICsIT covers from 200 keV to 10 MeV. The detector layers are surrounded by the BGO active shield, and a passive tungsten collimator is placed between the mask and BGO shield. The distance between the tungsten mask and the upper layer detector is 3.2 m, so that IBIS has a good angular resolution of 12 arc sec.

Chapter 3

Advanced Compton Imaging

3.1 Imaging by Electron Tracking Compton Method

The electron tracking Compton imaging measures both the energy and the direction of the incident gamma-ray by obtaining with the energy and direction of the scattered gamma-ray and the recoil electron. In Figure 3.1, the energy and direction of the scattered gamma-ray are E_γ and \vec{g} , the energy and direction of the recoil electron are K_e and \vec{e} , the scattering angle is ϕ , the recoil angle is ψ and the differential angle between \vec{g} and \vec{e} is α , where \vec{g} and \vec{e} are the unit vectors. Then, the incident energy E_0 and the incident direction \vec{s} of the initial gamma-ray are described, respectively:

$$E_0 = E_\gamma + K_e, \quad (3.1)$$

$$\vec{s}_{\text{rcs}} = \left(\cos \phi - \frac{\sin \phi}{\tan \alpha} \right) \vec{g} + \frac{\sin \phi}{\sin \alpha} \vec{e}, \quad (3.2)$$

$$= \frac{E_\gamma}{E_\gamma + K_e} \vec{g} + \frac{\sqrt{K_e(K_e + 2m_e c^2)}}{E_\gamma + K_e} \vec{e}. \quad (3.3)$$

where the scattering angle is ϕ , which is written as follows,

$$\cos \phi = 1 - \frac{m_e c^2}{E_\gamma + K_e} \frac{K_e}{E_\gamma}, \quad (3.4)$$

and the recoil angle ψ is

$$\cos \psi = \left(1 + \frac{m_e c^2}{E_\gamma + K_e} \right) \sqrt{\frac{K_e}{K_e + 2m_e c^2}}. \quad (3.5)$$

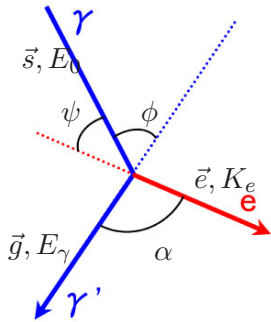


Figure 3.1: The parameters in Electron Tracking Compton Imaging

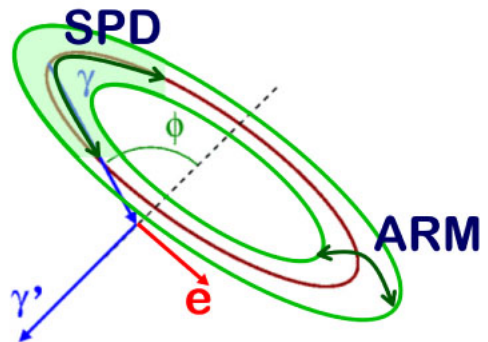
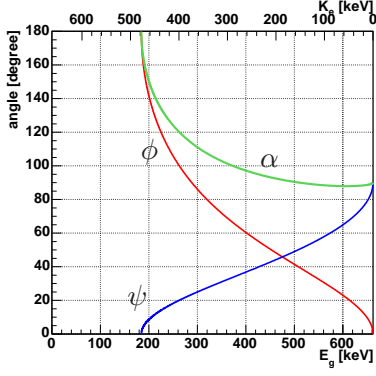
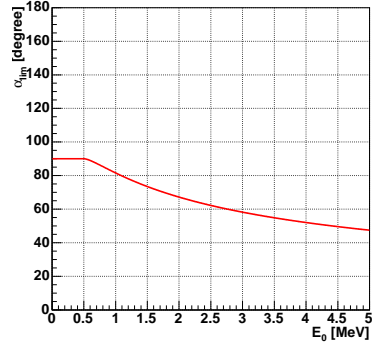


Figure 3.2: The definition of ARM & SPD


 Figure 3.3: The E_γ dependence of ϕ , ψ , α ($E_0 = 662$ keV)

 Figure 3.4: The E_0 dependence of α_{lim}

The differential angle α between \vec{g} and \vec{e} is described by the definition:

$$\cos \alpha_{geo} = \vec{g} \cdot \vec{e}. \quad (3.6)$$

On the other hand, α is described with E_γ and K_e by the Compton kinematics:

$$\cos \alpha_{kin} = \left(1 - \frac{m_e c^2}{E_\gamma}\right) \sqrt{\frac{K_e}{K_e + 2m_e c^2}}. \quad (3.7)$$

The angle α has a minimum value depending on the energy of the incident gamma-ray, and the minimum is described:

$$\cos \alpha_{lim} = \begin{cases} 0 & (k < 1) \\ \frac{k-1}{k+2} \sqrt{\frac{k^2-1}{k(k+2)}} & (k \geq 1) \end{cases} \quad k = \frac{E_0}{m_e c^2}. \quad (3.8)$$

Figure 3.3 shows the dependence of ϕ , ψ and α on E_γ , and Figure 3.4 shows the dependence of α_{lim} on E_0 , respectively.

The angle α is a characteristic parameter of the electron tracking Compton imaging. The α makes it possible to select the Compton scattering events from the backgrounds. The α is obtained from the equation (3.6) and (3.7), where (3.6) depends on only the geometrical information, and (3.7) depends on only the kinematic information. Thus, the α_{geo} is independent from the α_{kin} . For this reason, we can select good events, in which Compton scattering occurs in the tracker and scattered photon absorbs perfectly in the absorber, by requiring the follows

$$\alpha_{geo} = \alpha_{kin}. \quad (3.9)$$

In the Electron Tracking Compton Imaging, the accuracy of the event reconstruction is estimated using two parameters. One is the Angular Resolution Measure (ARM), which is the accuracy of the scattering angle:

$$\Delta \phi_{ARM} = \arccos(\vec{s} \cdot \vec{g}) - \arccos\left(1 - \frac{m_e c^2}{E_\gamma + K_e} \frac{K_e}{E_\gamma}\right). \quad (3.10)$$

The other is Scatter Plane Deviation (SPD), which is the accuracy of the determination of the scattering plane:

$$\Delta \nu_{SPD} = \text{sign}\left(\vec{g} \cdot \left(\frac{\vec{s} \times \vec{g}}{|\vec{s} \times \vec{g}|} \times \frac{\vec{s}_{rcs} \times \vec{g}}{|\vec{s}_{rcs} \times \vec{g}|}\right)\right) \arccos\left(\frac{\vec{s} \times \vec{g}}{|\vec{s} \times \vec{g}|} \cdot \frac{\vec{s}_{rcs} \times \vec{g}}{|\vec{s}_{rcs} \times \vec{g}|}\right). \quad (3.11)$$

where \vec{s} is the real direction, and \vec{s}_{rcs} is the reconstructed direction of the incident gamma-ray. Thus, the error region of one event is a sector shape, as shown in Figure 3.2.

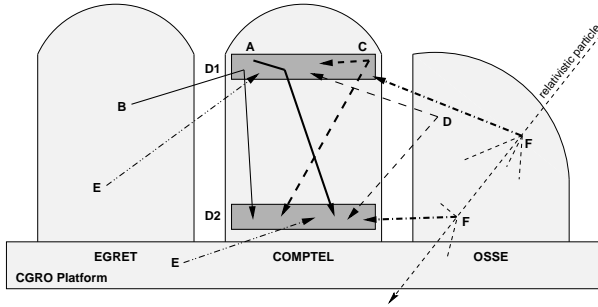


Figure 3.5: The various background of COMPTEL [35]

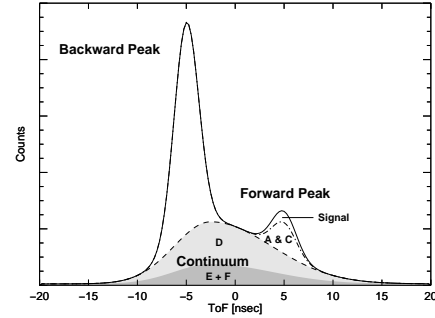


Figure 3.6: The TOF distribution [35]

3.2 Background Rejection

MeV gamma-rays are produced by various processes such as a de-excitation of nuclei, hadron interactions and a decay of radioactive nuclei. Actually, COMPTEL had various backgrounds as shown in Figure 3.5, of which detail was described in [35]. Each process is:

- A Internal Single Photon: Gamma-rays, which are produced at the inside of the detector by neutron capture or by radioactive isotopes (like ^{40}K), may make Compton scattering in the forward detector, and its scattered gamma-rays are absorbed in the backward detector.
- B External Single Photon: Gamma-rays are produced at another detectors or the satellite platform by neutron capture, decay of radioactive isotopes and scattering, and then they may make Compton scattering in the forward detector and its scattered gamma-rays are absorbed in the backward detector.
- C Internal Multi-photon: Multi-photons are produced by the interactions, like $^{27}\text{Al}(n,\alpha)^{24}\text{Na}$ or $^{27}\text{Al}(n;n',\dots)^{27}\text{Al}$. Then some photons may hit the forward detector and also the backward detector simultaneously.
- D External Multi Photon: In another detectors or the satellite platform, some gamma-rays may be created by the same processes of C, and some photons may hit the forward detector and also the backward detector simultaneously.
- E Random Coincidence: Sometimes, the different photons produced by the independent interactions hit the forward detector and also the backward detector accidentally.
- F Cosmic-Ray Interaction: When cosmic-ray comes into the satellite, it interacts with material at the different positions, generates some photons simultaneously. Then those photons hit both the forward and backward detectors.
- Other Process: As the other backgrounds, neutron, electron and atmospheric gamma-rays were measured.

COMPTEL rejected the backgrounds using the time of flight (TOF) between both detectors. Figure 3.6 shows the distribution of TOF by simulation. Although the most events are backward events in which gamma-ray interacts in the backward detector and then in the forward detector, these events can be easily rejected using the timing above 1 MeV. But D, E and F events make continuum component, and the forward peak includes the one third of them. Since the interaction of A and B events are the real Compton interaction, they are the intrinsic background and can't be rejected. Moreover, if there is a decay in the forward detector, C events have no difference in TOF distribution. Therefore, even if we pick up the forward peak, the most of the selected events are still background events as shown in Figure 3.6.

In comparison with classical Compton imaging, electron tracking Compton camera can reduce the background using the angle α . Because of this kinematic fit, we can enhance the correct events, and C, D, E and F events can be rejected. Therefore, signal to noise ratio becomes better than classical Compton imaging.

3.3 Doppler Broadening

In the previous sections, we suppose that Compton scattering occurs with a free electron. That process is called unbound Compton scatter. However, in actual detectors, electrons are bounded in the potential energy of the nuclear or molecular orbits. Thus, electrons have a kinematic energy before the Compton scattering, and the actual scattering (bound Compton scattering) is affected as follows,

- scattering cross section:
Especially, for the low energy photon under 100 keV, the cross section is slightly increased.
- distribution of scattering angle:
In comparison with (2.5), the forward/backward scattering is reduced slightly.
- energy of scattered gamma-ray and recoil electron:
Because the electron before the scattering has a finite energy, the energy of scattered gamma-ray that are scattered at a fixed angle from a monoenergetic source has a narrow distribution around the estimated energy from an unbound Compton scattering. This effect is called Doppler broadening.

In Compton imaging, the scattering angle is obtained by the energy of scattered gamma-ray and the energy of recoil electron. Therefore, the accuracy of the scattering angle (ARM) is certainly affected by Doppler broadening, and Doppler broadening makes the intrinsic limit for the angular resolution of the ARM.

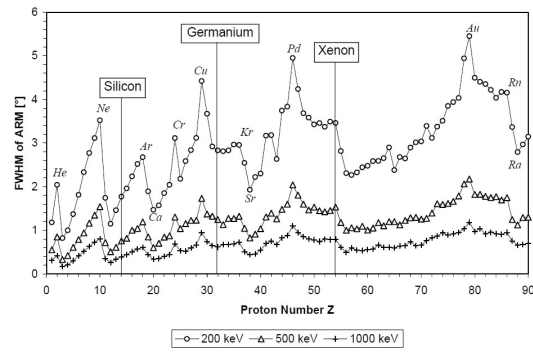
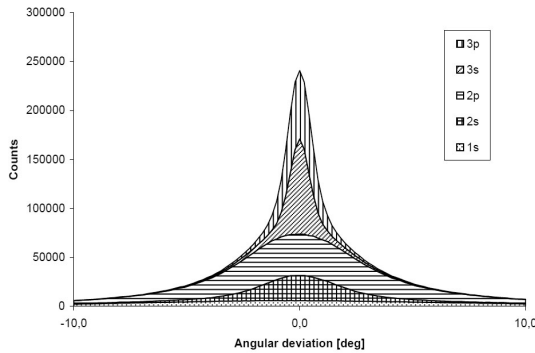


Figure 3.7: The ARM distribution of each electron orbit ($E_0 = 200\text{keV}$, Si) [36] Figure 3.8: The Z dependence of the ARM [36]

Since Doppler broadening is caused by the motion of the electron before the scattering, the energy distribution of scattered gamma-ray is changed at which orbit the electron recoils. Figure 3.7 shows the uncertainty of the ARM of each orbit. Because the electron at the outer orbit has the lower kinematic energy, the effect of Doppler broadening is smaller, and the uncertainty of the ARM is the smaller. The dependence of the uncertainty of the ARM on Z is shown in Figure 3.8. When Z of target material is larger, Doppler broadening makes a larger uncertainty of the ARM. Figure 3.9 shows the energy dependence of Doppler broadening. The energy of an incident gamma-ray is higher, the effect of Doppler broadening is smaller because the initial energy of an electron is smaller enough.

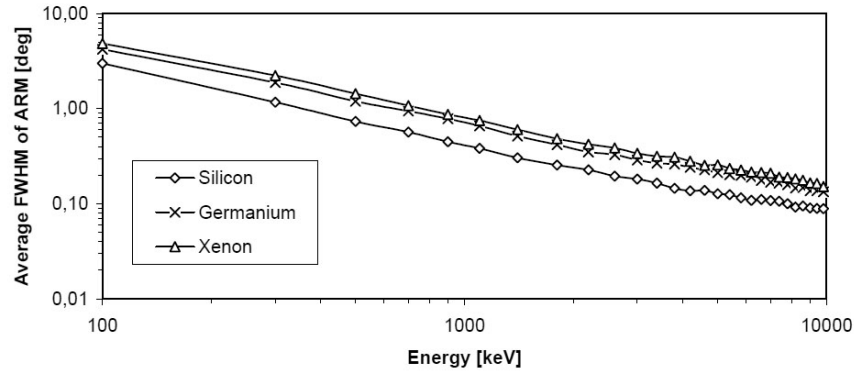


Figure 3.9: The energy dependence of Doppler broadening [36]

3.4 Multiple Scattering

The electron tracking Compton camera can determine the scatter plane using the direction of the recoil electron, and the incident gamma-rays are reconstructed specifically. The scatter plane is determined from the scattered gamma-ray direction \vec{g} and the recoil electron direction \vec{e} . The accuracy of \vec{g} depends on the distance between two detectors and the position resolutions of them. On the other hand, the recoil electron loses the directional information \vec{e} because of the multiple scattering in the material of the tracker. Thus, multiple scattering is an intrinsic limit of SPD.

The uncertainty of the scattered angle is described by Moliere theory, which approximates to a Gaussian for the small angle scattering [37]. At the range x , the scattered angle is:

$$\theta_{\text{rms}} = \frac{13.6\text{MeV}}{\beta c p} \sqrt{\frac{x}{X_0}} \left[1 + 0.038 \ln \left(\frac{x}{X_0} \right) \right], \quad (3.12)$$

where βc , p and X_0 are the velocity of an electron, the momentum and the radiation length, respectively. Figure 3.10 shows the scattered angle depending on the electron energy, and Figure 3.11 shows the dependence on the range.

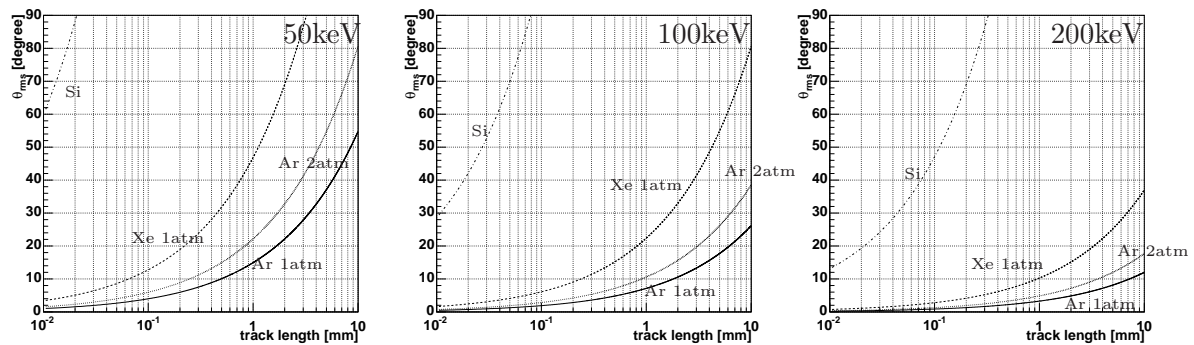


Figure 3.10: The scattered angle depending on electron energy (left: 50keV, center: 100keV, right: 200keV; gas temperature: 20°C)

If the tracker consists of the stack of silicon strip detectors, the recoil electron should pass via a few silicon layers for the determination of the recoil direction. Generally, the thickness of the silicon strip detector is 300 - 500 μm . When the recoil electron has an energy of 500 keV, the scattered angle is about 60°, so that it is hard to determine the recoil direction. On the other

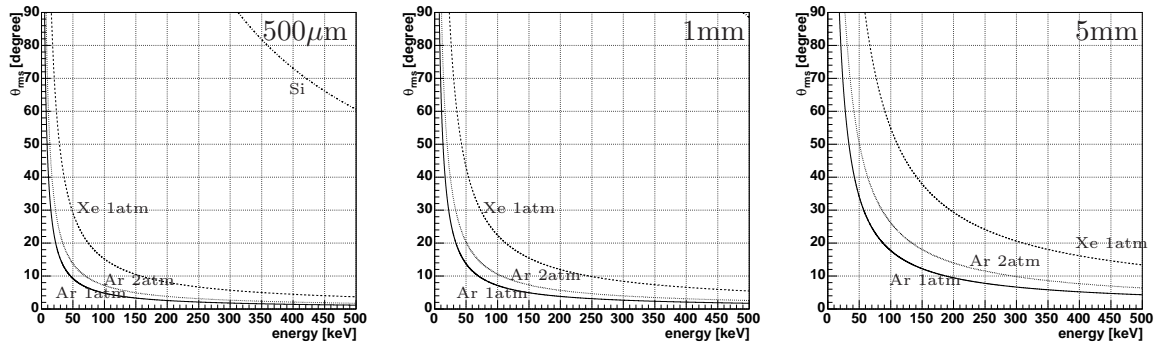


Figure 3.11: The scattered angle depending on range (left: $500\mu\text{m}$, center: 1mm , right: 5mm ; gas temperature: 20°C)

hand, with a tracker using argon gas at 1 atm, if the recoil direction is obtained determinable at 1 mm, the scattered angle is $\sim 15^\circ$ and the SPD accuracy becomes well than that of the silicon tracker. Therefore, a gaseous detector is selected as a tracker.

3.5 Composition of Advanced Compton Camera

3.5.1 Goal for Next Generation Telescopes

After COMPTEL, there is only INTEGRAL launched as the satellite of gamma-ray observatories, and LXeGRIT, NCT and CLAIRE are balloon experiment with short observation time. Since SPI and IBIS on INTEGRAL uses a coded aperture imaging, the sensitivity for the continuum spectrum is worse than that of COMPTEL, as shown in Figure 3.12. Therefore, the developments of the detector with a higher sensitivity and observations using such a camera are wished. Then, we set the goal of our detector to ‘ten times better sensitivity than COMPTEL’.

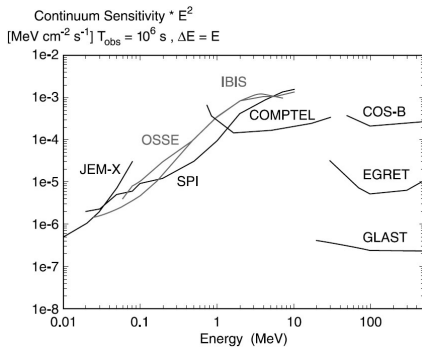


Figure 3.12: The continuum sensitivities of X/Gamma-ray observatories [38]

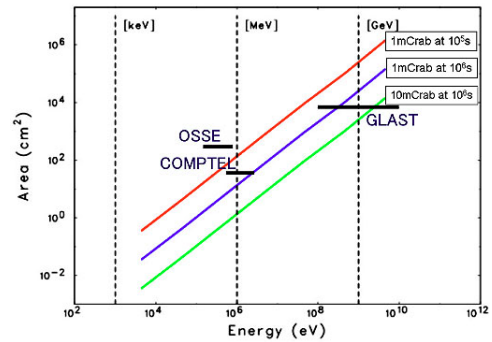


Figure 3.13: The effective area of X/gamma-ray observatories [39]

Figure 3.13 shows the effective area of various observatories. This figure says that COMPTEL had been expected to achieve 1 mCrab source detection in 10^6 sec observation time if there were no background. However, actually, the background rejection power of COMPTEL was limited, as shown in Figure 3.6, and the signal to noise ratio was quite worse than expected. Therefore, the electron tracking Compton camera, even if its effective area is as same as COMPTEL, is expected to reach the goal by the improving the signal to noise ratio.

3.5.2 Requirements for Tracker and Absorber

A camera based on electron tracking Compton imaging consists of a tracker and an absorber, so I explain the requirements on each detector.

A tracker, which is the target of Compton scattering and detects the momentum of the recoil electron, requires the accuracy of the recoil direction. Hence a gaseous detector looks better as a tracker than a solid state detector. On the other hand, since the density of solid is higher by 3 order than that of gas, a solid detector has a larger cross section per unit volume than a gaseous detector. However, a gaseous detector with a large volume is easily made. Figure 3.14 is the energy dependence of Compton scattering probability. This figure says that Xe gas of $50 \times 50 \times 50 \text{ cm}^3$ at 1 atm which has an effective area of $\sim 30 \text{ cm}^2$, which is nearly equal to that of COMPTEL ($\sim 40 \text{ cm}^2$) for 1 MeV gamma-ray. Therefore, a gaseous detector can become a good Compton scattering target. As a Compton scattering target, lower Z material is better, because lower Z material has a wider energy band of Compton scattering dominance, and has less effect of Doppler broadening (see Figure 2.2 and 3.8). Besides, for the detection of the recoil direction with an enough accuracy, the determination of the direction within a few mm length from the Compton point is required. Since the energy of the recoil electron is in the range from $\sim 50 \text{ keV}$ to several hundred keV, the energy loss of the recoil electrons are minimum ionizing during a few mm from the Compton point. For this reason, the tracker must trace the recoil electron with several points within a few mm. In summary, a tracker requires the following features.

- Large volume gaseous detector : Gas has little impact of multiple scattering, and large volume makes up for a small cross section.
- Compton scattering dominant gas : A gas, which consists of the low Z atoms but have a lot of electron per a molecule, is good as a scattering target of Compton process, for example CF_4 and CH_4 .
- Fine Minimum Ionizing Particle (MIP) tracing : The determination of the recoil direction with a good accuracy requires a fine position resolution and fine sampling with a sub-mm pitch.

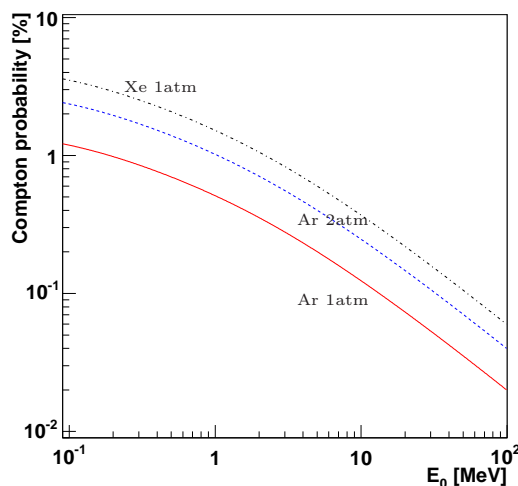


Figure 3.14: The probability of Compton scattering (depth of 50cm)

Absorbers for the scattered gamma-rays are placed around the tracker. In the tracker, gamma-rays are scattered in various directions. Then an absorber is required to cover the large

area. Besides, the scattered gamma-rays often have most energy of the incident gamma-rays in the Compton process, because the probability of the forward scattering is higher than that of the backward scattering. Therefore a high Z absorber is better for the detection of the scattered gamma-rays, of which energy is from hundred keV to a few MeV. The energy and position resolutions of the absorber are strongly related with the resolution of the ARM. In principle, the ARM has a limit due to Doppler broadening. Then the uncertainty by each resolution is wished less than that of Doppler broadening. If an Ar gas is used in a tracker, the uncertainty of the

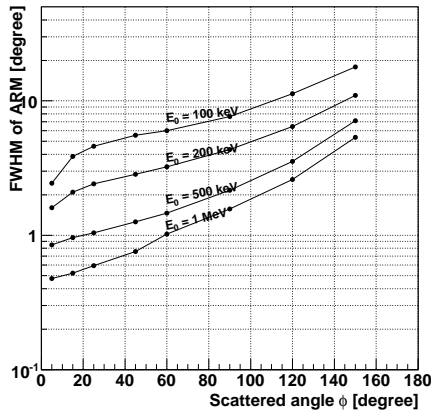


Figure 3.15: The dependence of ARM uncertainty by Doppler broadening on scattering angle (E_0 : energy of incident gamma-ray, GEANT4 simulation)

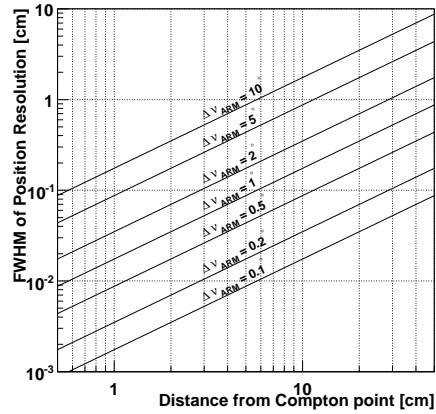


Figure 3.16: The ARM uncertainty ($\Delta\nu_{\text{ARM}}$) depending on position resolution and distance from Compton point

ARM by Doppler broadening behaves as shown in Figure 3.15. From this figure, the uncertainty of the ARM for 500 keV gamma-rays with the scattering angle of 20° is $\sim 1^\circ$ at FWHM. On the other hand, Figure 3.16 shows the variations of the ARM uncertainty depending on the position resolution and the distance from the Compton point, respectively. Figure 3.16 shows that the absorber should have the spacial resolution under 1 mm for the ARM uncertainty of 1° . The requirement of the energy resolution is determined from Figure 3.17. In Figure 3.17, the solid lines means that the uncertainty due to Doppler broadening is equal to the uncertainty due to the energy resolution when the scattering angle is constant. This figure says that the absorber

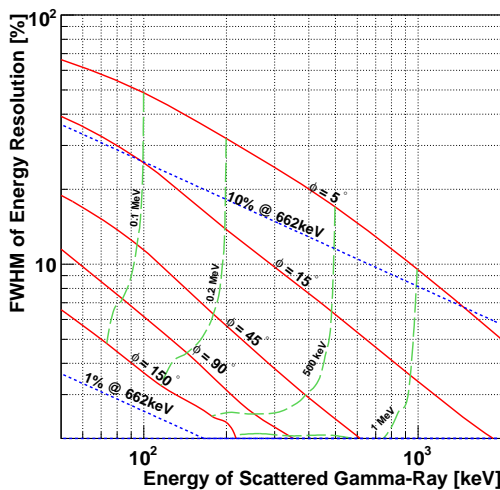


Figure 3.17: The requirement of energy resolution for absorber. The solid line means the ARM uncertainty by energy resolution, equal to the uncertainty by Doppler broadening with constant scattering angle, and the dashed line is such condition with constant energy of incident gamma-ray. The dotted line is typical energy resolution of real detectors (energy resolution [%] $\propto 1/\sqrt{\text{energy}}$).

should have an energy resolution of a few percents at least. For summarize, the absorber requires the following features.

- Large effective area: An absorber is required to surround the tracker.
- High stopping power: Absorber must have a mass enough to stop the scattered gamma-rays.
- Fine Position resolution: Absorber should have a position resolution of ~ 1 mm so that the uncertainty of scattered direction must be smaller than that due to Doppler broadening.
- Good Energy resolution: Absorber should have an energy resolution of several percent for hundreds keV.

3.5.3 Advanced Compton Camera with Gaseous Electron Tracker

From above-mentioned requirements, we constructed an advanced Compton camera with the ability of the electron tracking. As the tracker, an usual multi-wire proportional counter does not fit, because the required fine pitch is not realized in a wire chamber. As an absorber, semiconductor detectors are difficult to use, because its use is not reasonable for a large effective area, although they has a fine energy resolution.

Therefore, we have developed an advanced Compton camera consisting of μ -TPC and a scintillation camera. μ -TPC is a Time Projection Chamber (TPC) based on μ -PIC, which is our original gaseous micro-pattern detector having both a fine position resolution and a large detection area. The scintillation camera is realized at the reasonable cost, although it has a worse energy resolution than that of the semiconductor detectors. Then we got a good absorber to make large and thick detection area. An electron tracking Compton camera is comprised from μ -TPC and the position-sensitive scintillation camera, as shown in Figure 3.18. As a final goal, we aim at the ten times better sensitivity than COMPTEL for MeV gamma-rays by developing this detector.

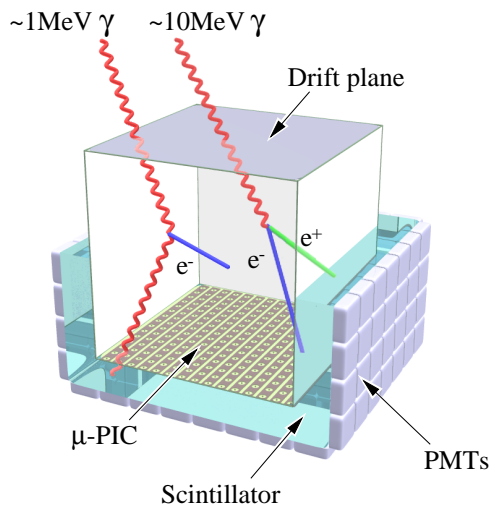


Figure 3.18: The schematic view of Advanced Compton Camera with Gaseous Electron Tracker

Chapter 4

μ -PIC, μ -TPC & Scintillator

4.1 μ -PIC (Micro Pixel Chamber)

The key of the electron tracking Compton camera is the development of the tracker having an enough position resolution for the recoil electrons. Since an electron is easy to lose the recoil direction information by the multiple scattering, a high position resolution of a few hundred μm is required for the tracker. As such a tracker, we have developed μ -TPC consisting of a micro pattern detector, μ -PIC.

4.1.1 Introduction of μ -PIC

Micro Pixel Chamber (μ -PIC), which has been developed from 2000, is a kind of Micro Pattern Gaseous Detector (MPGD) [40]. Figure 4.1 is the schematic view of μ -PIC. The μ -PIC has a pixel electrode like a sliced proportional counter. The substrate is made by polyimide, and the electrodes are Cu coated with Ni. μ -PIC is manufactured by the print circuit board technology, and thus the device with a very large area can be easily developed. Actually, the large μ -PIC of $30 \times 30 \text{ cm}^2$ is now working. Each pixel is aligned with the pitch of $400 \mu\text{m}$. μ -PIC has ~ 65000 pixels in an area of $10 \times 10 \text{ cm}^2$ and $\sim 6 \times 10^5$ pixels in an area of $30 \times 30 \text{ cm}^2$, respectively. The anode and cathode electrodes are connected on the strip, respectively, and these electrodes run perpendicularly. Therefore, μ -PIC has a 2 dimensional position sensitivity with a fine position resolution.

The small pixel structure causes a high gas gain (20000 at maximum, and 6000 in stable operation) and a long stability (1000 hours with gain of 6000), because the pixel electrode is hardly damaged by discharge, which was a serious problem for Micro Strip Gaseous Chamber. Also μ -PIC can work under the high intensity of $\sim 10^7 \text{ count}/(\text{sec cm}^2)$ by the smallness of the pixel.

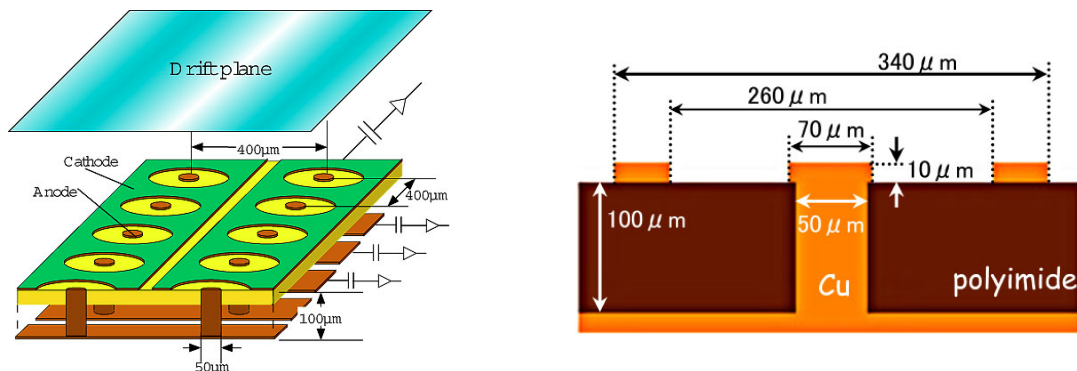


Figure 4.1: The structure of μ -PIC

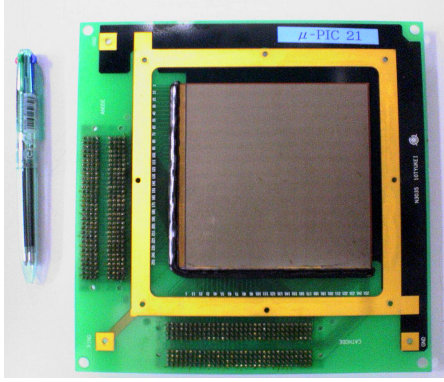


Figure 4.2: $10 \times 10 \text{ cm}^2$ μ -PIC

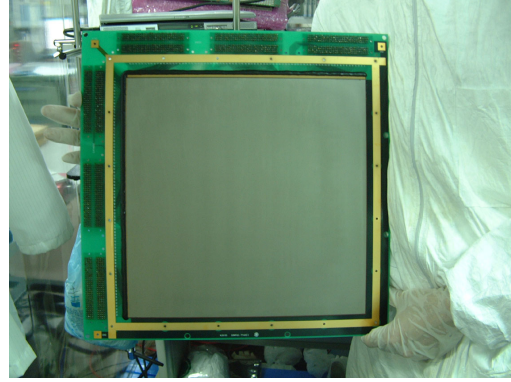


Figure 4.3: $30 \times 30 \text{ cm}^2$ μ -PIC

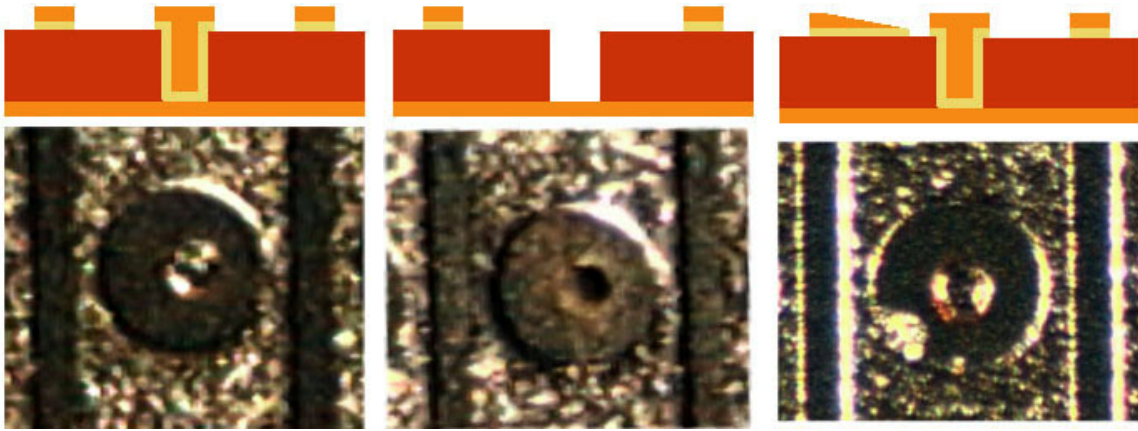


Figure 4.4: 3 types of pixels: good pixel (left), dead pixel (middle), bad pixel (right)

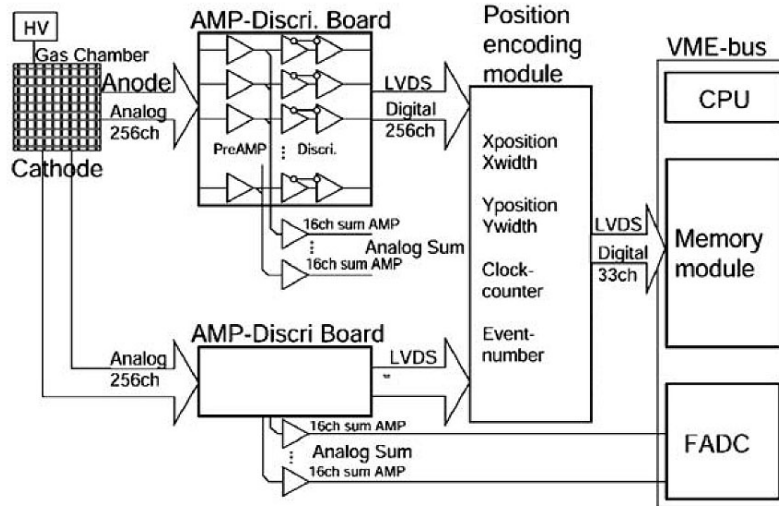
4.1.2 Morphology of Pixels

The pixel electrode of μ -PIC is manufactured by the following process. The first process is the electroless plating for creating the seeds of via-fill plating. Next is the via-fill plating, in which the anode-holes are filled up, and the polyimide substrate are coated with copper. Then, copper is etched to obtain a flat surface. Finally, the pixel electrodes are created by etching.

The created pixels are classified into the three groups by eye scan.

1. Good pixels: The structure of the pixel is ideal, as shown in the left of Figure 4.4 and these pixels make the stable operation. The majority of the pixels is classified into this type.
2. Dead pixels: The dead pixels are due to the miss-plating. The anode hole of the dead pixel is not filled up by copper, as shown in center of Figure 4.4, and the electric field does not concentrate to the center of the pixel. Then there is no electron avalanche and no signals.
3. Bad pixels: The bad pixels are due to miss-etching. The bad pixel has a protrusion on the edge of the cathode electrode, as shown in the right of Figure 4.4. On the surrounding of the protrusion, the electric field is too strong to suppress the discharge.

A dead pixel has no signal, even if a high voltage is supplied. Thus, a dead pixel is no problem for the stable operation. However, if there are many dead pixels in a small area, the image is broken naturally. A $10 \times 10 \text{ cm}^2$ μ -PIC has few dead pixels at present ($< 10^{-3} \%$). But a 30×30

Figure 4.5: Data Acquisition System for μ -PIC [41]

cm^2 μ -PIC at the first production had 0.1% dead pixels in the whole area. Especially in the worst area, the pixels of 40 % in $3 \times 5 \text{ cm}^2$ were dead pixels.

A bad pixel causes discharges, which obstructs the stable operation. The bad pixels distribute into the whole area at random. The existence ratio is less than 0.01 % in $10 \times 10 \text{ cm}^2$ μ -PIC and that is less than 0.1 % in $30 \times 30 \text{ cm}^2$ μ -PIC. The reduction of dead pixels is the first priority of μ -PIC improvement.

4.1.3 Readout Circuit

Since a μ -PIC has a lot of readout strips (a $10 \times 10 \text{ cm}^2$ μ -PIC has 512 ch, and a $30 \times 30 \text{ cm}^2$ μ -PIC has 1536ch), we have developed a readout system for μ -PIC. The schematic view of this system is shown in Figure 4.5.

Each of all strips connects to a preamplifier chip one by one, and the amplifier feeds both an analog signal and a discriminated digital signal. The analog signal is summed with every 16 channels on the board, and the wave form is digitized by Flash ADC (FADC). The digital signal is fed to the position encoder one by one. The position encoder takes the coincidence of the anode signals and the cathode signals, and then it calculates the position of the hit strips. The number of the hit electrode is sent from the position encoder to a memory module on a VME system. This hit pattern readout system is rapid, because a CPU on the VME reads only the hit strip numbers and the clock counter of the coincidence.

High Voltage Supply Board

In a μ -PIC, a positive High Voltage (HV) is supplied on the anodes via the high voltage supply board, as shown in Figure 4.6, and the right of Figure 4.6 shows the circuit diagram. The board supplies a high voltage to 256 anode strips. For a $30 \times 30 \text{ cm}^2$ μ -PIC readout, three boards are needed for x or y coordinates readout. In this board, 256 strips are gathered into 16 groups, and each group is connected to the HV supply via a register of $1 \text{ G}\Omega$, then one group is almost insulated from other groups. Thus, even if the leak current flows in one group, the pixels of other groups can be operated safely. In one group, a high voltage is supplied to every 4 strips, so that effective area is not reduced with the current flow of one group.

This HV supply board also works as a part of the feedthrough, as shown in Figure 4.7. The readout of the signals from all strips with the usual vacuum feedthrough connectors is very hard.

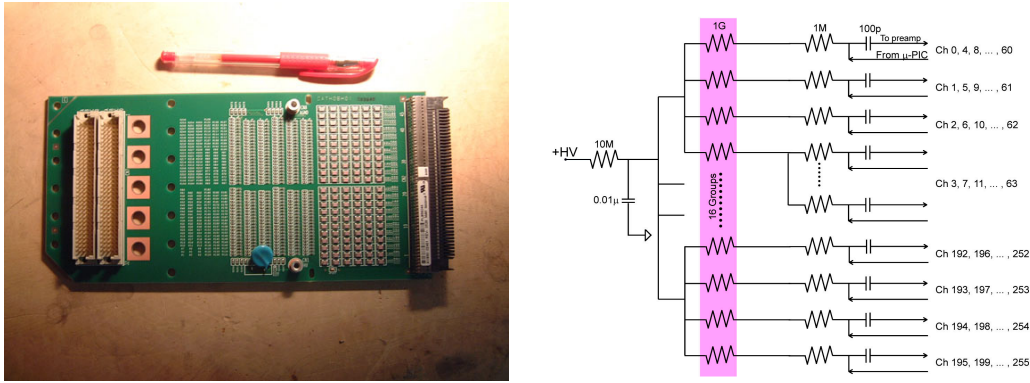


Figure 4.6: The photograph and the circuit diagram of the high voltage supply board

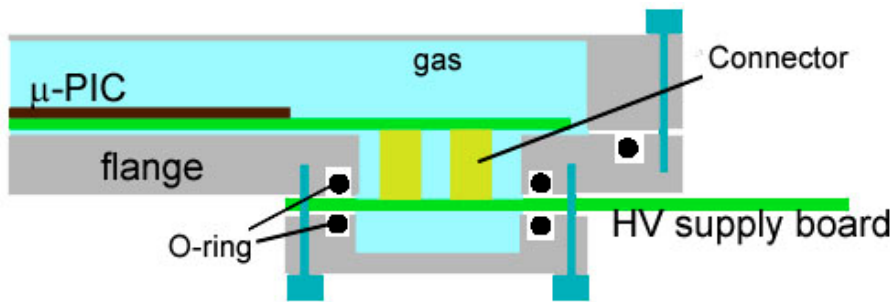


Figure 4.7: The schematic view of the connection of a μ -PIC and a HV supply board

The raw signals before a preamplifier is too small to be transferred using a long cable. By this feedthrough system, we can easily get signals from the vacuum vessel without the deterioration of the signal to noise ratio.

ASD Bread Board & Rack

As a preamplifier for μ -PIC, we use ASD (Amplifier-Shaper-Discriminator) chips, which were developed by KEK for Thin Gap Chamber of ATLAS experiment in LHC at CERN [42]. The ASD chip has 4 input lines per 1 chip. Each line has a preamplifier, main-amplifier, discriminator, analog output and digital outputs. The preamplifier has a time constant of 16 nsec, and the analog signal is an output of this preamplifier output signal. The digital outputs are the discriminator outputs in LVDS.

We use this ASD chip on the bread board shown in Figure 4.8. This board has 64 inputs and 16 ASD chips per 1 board. All analog signals are summed once in every 16 channels, and also 32 channels are summed using the 16 channels summing signals. Thus, we get 4 analog outputs of summing 16 channels or get 2 analog outputs summing 32 channels. Also, all of the digital output of ASD chips are fed one by one.

The ASD bread board is inserted in the rack, as shown in Figure 4.9. The rack includes 4 bread boards and a common threshold level supply for the discriminator of 4×16 ASD chips. We can select the internal generation or external-input for the supply of threshold level. At the back plane of the rack, the high voltage supply board is inserted. For the short timing gate of 10 nsec in the position encoder, the difference of the pattern length from the μ -PIC strip readout to the digital outputs is less than 3 nsec.

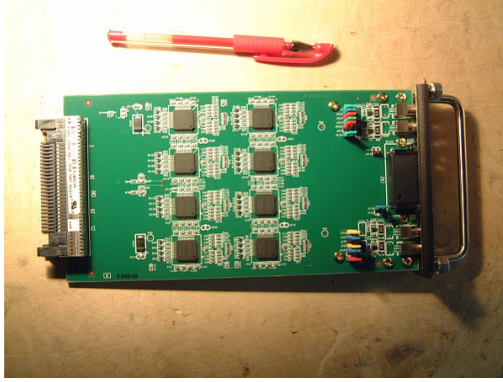


Figure 4.8: ASD bread board



Figure 4.9: ASD Rack

Position Encoder

The digital outputs of the preamplifier bread board are inputted into the position encoder (Figure 4.10). The position encoder consists of 8 FPGAs (Field Programmable Gate Array), and has 1576 LVDS digital inputs, 5 LVDS I/O ports and the memory-writing port. In 8 FPGAs, 6 FPGAs are the same type FPGA for the position calculation, one for the encoding and the other is for the DAQ.



Figure 4.10: Photograph of position encoder

Figure 4.11 shows the block diagram of the position encoder. The position encoder is synchronously operated with the 100 MHz clock generated by FPGA 7. Each FPGA for the position calculation (FPGA 1-6) has 256 LVDS inputs. The Anode hit signals provided by ASD chips are fed into three FPGAs 1-3, and the cathode ones are into FPGAs 4-6. Each FPGA for the position calculation computes the maximum and minimum number among the hit lines in one clock of 100 MHz, and then send the minimum and maximum number to FPGA 7. When FPGA 7 receives the minimum and maximum number of each FPGA for the position encoding, it takes a coincidence of the x -coordinate FPGA 1-3 and the y -coordinate FPGA 4-6 within one clock. When there is a coincidence, FPGA 7 calculates the minimum and maximum ID for both x and y coordinates. After then, FPGA 7 sends these data to the memory module with the count of the clock from the trigger input asynchronously. DAQ-FPGA (FPGA 8) is used for the communication with other modules, like ADCs or CPU. Besides, FPGA 7 also has an I/O port for the communication with other module. Using the I/O ports of FPGA 7 and 8, we will construct even a complicated system compactly.

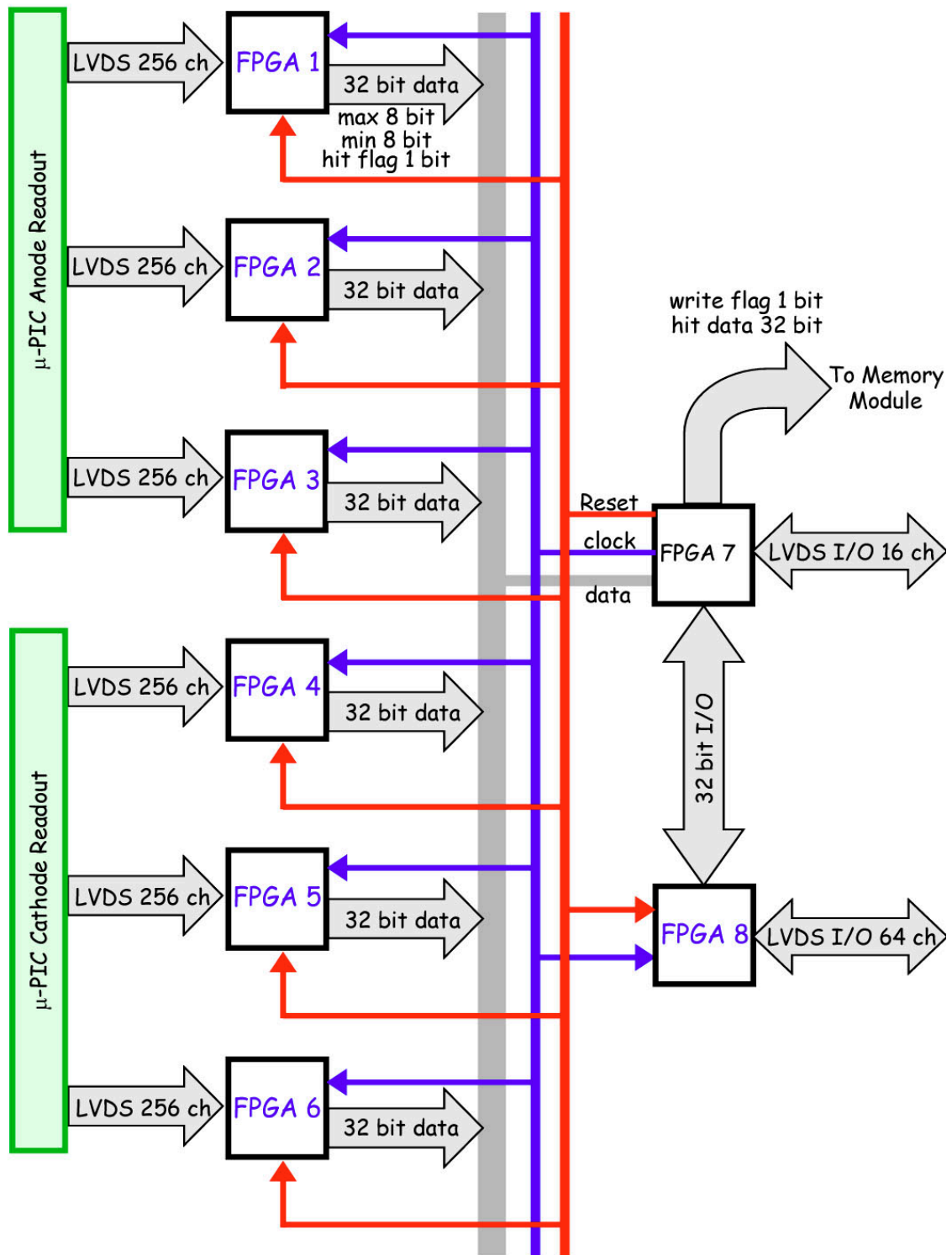


Figure 4.11: The hardware mechanism of the position encoder

4.1.4 Performance of μ -PIC

Gas Gain

μ -PIC gets a signal amplified by gas multiplication like a proportional counter. A fine structure electrode of Micro Pattern Gaseous Detectors (MPGD) suffers from a discharge, since a high voltage at narrow gap of a few hundred μm between an anode and a cathode. In principle, any MPGD has a triplet junction, at which gas, electrode and insulator connect. Such a triplet junction is considered to cause a discharge easily. Therefore the gas gain of MPGD is limited by discharge around the triplet junction. For example, Micro Strip Gas Chamber was able to be used at a maximum stable gain of ~ 1000 .

The gas gain of μ -PIC is shown in Figure 4.12. This figure says that μ -PIC has a maximum gain of ~ 20000 , which is very high gain for MPGD. Also μ -PIC have realized a good stability with the gain of ~ 6000 during more 1000 hours. Thus, μ -PIC is a stable detector having a high gas gain.

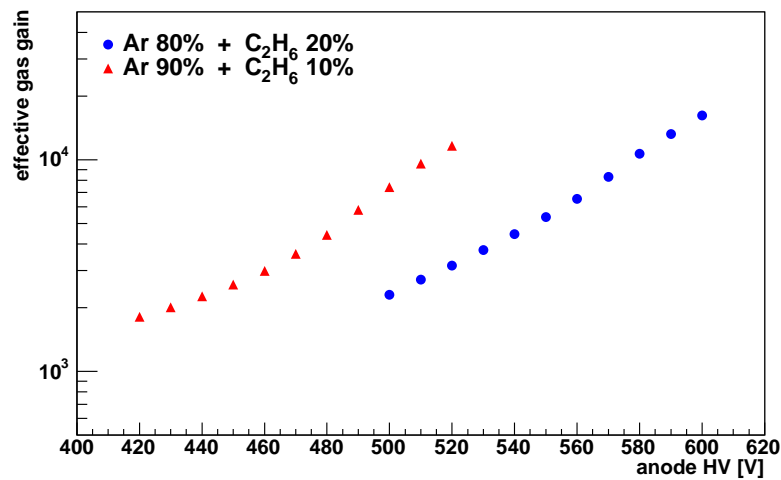


Figure 4.12: The effective gas gain as a function of the anode voltage (SN040223-1)

Uniformity

Since a $10 \times 10 \text{ cm}^2$ μ -PIC has 65536 pixels ($= 256 \text{ ch} \times 256 \text{ ch}$) and a $30 \times 30 \text{ cm}^2$ one has 589824 pixels ($= 768 \text{ ch} \times 768 \text{ ch}$). The non-uniformity of the pixel structure causes a non-uniformity of the gain on μ -PIC.

Figure 4.13 shows the gain map of the $10 \times 10 \text{ cm}^2$ μ -PIC, which surely indicates that μ -PIC has a good uniformity. The Root Mean Square (RMS) of the gain variation on the whole area is $\sim 5 \%$. On the other hand, Figure 4.14 shows the gain map for the $30 \times 30 \text{ cm}^2$ μ -PIC. The ratio of the gain between the minimum gain area and the maximum gain area is 2.2, and the gas gain uniformity is 16.7 % at the RMS.

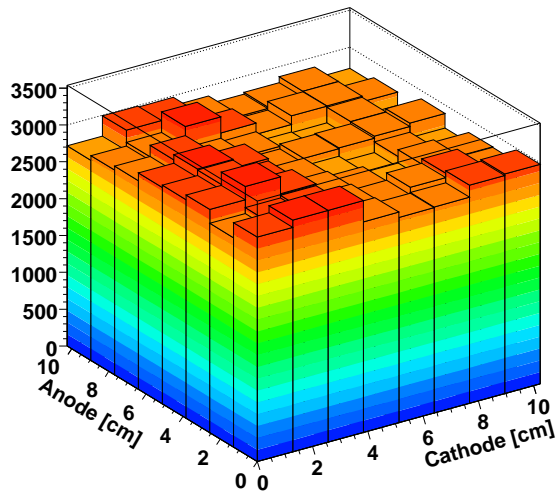


Figure 4.13: The effective gain map of $10 \times 10 \text{ cm}^2$ (SN040426-1)

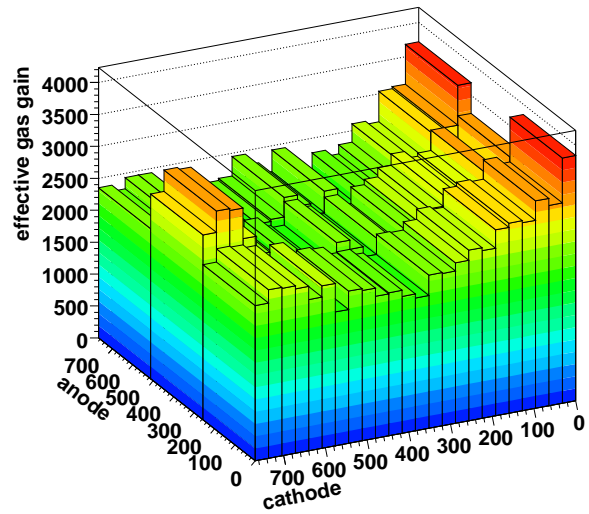


Figure 4.14: The effective gain map of $30 \times 30 \text{ cm}^2$ (SN041129-1)

4.1.5 μ -PIC as an X-ray Imaging Detector

μ -PIC is used as an X-ray imaging detector. Figure 4.15 shows a spectrum of ^{55}Fe measured by $10 \times 10 \text{ cm}^2$ μ -PIC. Because of the good uniformity of a gas gain, the energy resolution for X-rays of 5.89 keV is 30 % at FWHM for the whole area. Figure 4.16 is an X-ray image of a test chart irradiated by the X-ray generator where the shadow of 2 slits per 1mm can be distinguished clearly. Using the image of the edge of this test chart, we obtained the position resolution is $\sim 120 \mu\text{m}$ at σ . This value is quite equal to the predicted one from statistics, which is $\frac{400\mu\text{m}}{\sqrt{12}} \simeq 115 \mu\text{m}$.

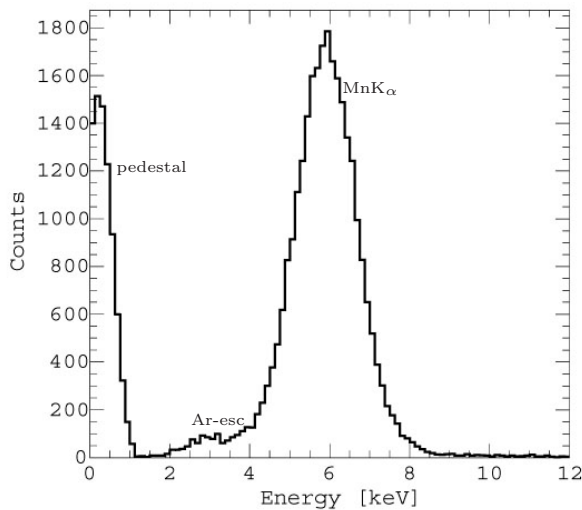


Figure 4.15: The spectrum of ^{55}Fe (whole area of $10 \times 10 \text{ cm}^2$; Ar 90 % + C_2H_6 10 %, 1 atm)

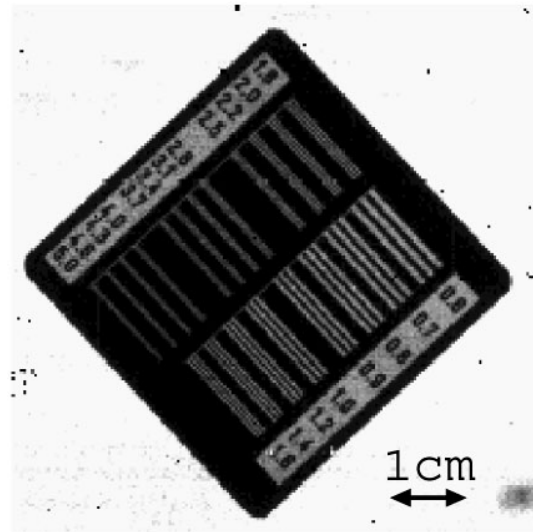
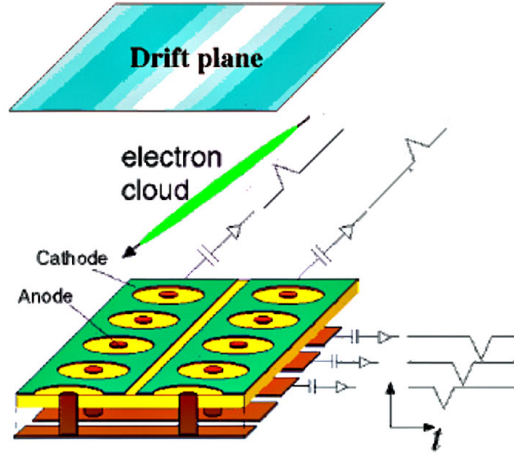


Figure 4.16: X-ray imaging of a test chart with $10 \times 10 \text{ cm}^2$ μ -PIC [43]

Figure 4.17: The schematic view of μ -TPC

4.2 Time Projection Chamber with μ -PIC (μ -TPC)

4.2.1 Structure and Principle of μ -TPC

When a charged particle passes through a gas, the gas around the particle track is ionized, in which a group of ionized electrons are called ‘electron cloud’. If there is an adequate electric field in the gas, the electron cloud drifts toward the electric field with the constant velocity. At this time, the drift time from the ionization point to the termination on the anode can be transferred to the distance between the ionization point and the termination point. Therefore, if we know the start timing of the drift, the distance between the ionization point and the anode is measured by the drift time. Such a system is called a Time Projection Chamber (TPC). A 2-dimensional detector, for example MWPC, is usually used, and the TPC can measure 3-dimensional positions of a track of a charged particle.

μ -PIC is a 2-dimensional gaseous detector, and is surely used as a readout detector of TPC. A TPC with μ -PIC is called μ -TPC, and the schematic view is shown in Figure 4.17. In our advanced Compton camera, this μ -TPC is used as a tracker, which detects a fine recoil electron track.

4.2.2 Gas Electron Multiplier

The energy deposit of MIP in the argon gas is 2.54 keV/cm at the normal pressure, in which a MIP makes about 3.9 electrons per 400 μm . For the detection of MIP tracks, we must detect such few electrons, which is very difficult. The MIP tracking needs a high gas multiplication of 2×10^4 at least with μ -PIC system, but the stable gas gain of μ -PIC is only about 6×10^3 . Then we use a Gas Electron Multiplier (GEM) [44] for the compensating this gain gap.

A GEM was developed by Sauli et al., and it is a polyimide foil with Cu-plated electrodes at both sides, as shown in left of the Figure 4.18. A GEM foil has a lot of small holes as shown in right of the figure. If the different voltage are supplied to Cu electrodes on both sides, a strong electric field is generated inside of this hole. When the seed electron drifts into this hole, the gas multiplication is caused in such a strong electric field. The foil is very thin with the thickness of 50 μm and consists of the low- Z material. But the distance of both electrodes is too short for a GEM foil to get a high gain alone, and hence the typical gain of single GEM is about 100.

We use this GEM foil as a pre-multiplier for μ -TPC (Figure 4.19). A seed electron drifts into the GEM, and the first multiplication is caused by the GEM with the gain of about 10. After that, the multiplied electrons drift to μ -PIC, and second multiplication is caused by μ -PIC with

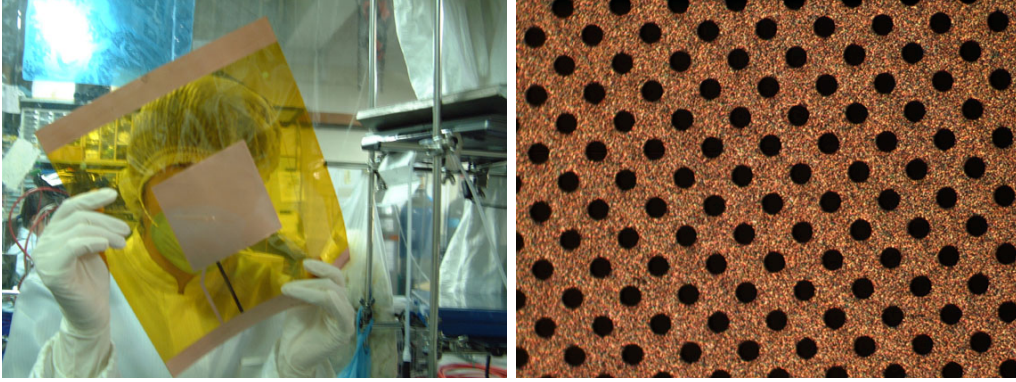


Figure 4.18: The photograph and microphotograph GEM. The hole diameter is $70 \mu\text{m}$, and the pitch of holes is $140 \mu\text{m}$.

a gain of thousands. Therefore, we can take an enough signal with a gas gain of above 2×10^4 . Figure 4.20 shows the gas gain of the GEM + μ -PIC system. In comparison with the gain of a single μ -PIC, the gain of the hybrid system is about 10 times larger than that of a single μ -PIC.

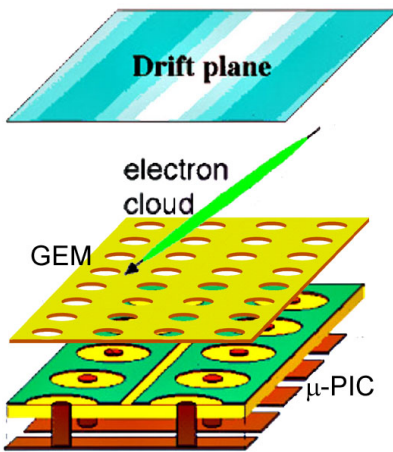


Figure 4.19: The schematic view of μ -PIC + GEM system

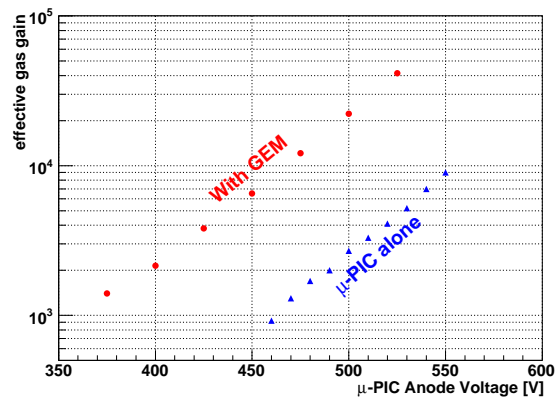


Figure 4.20: The comparison of the gain curve of GEM + μ -PIC and that of μ -PIC alone (SN040922-1, Ar 90 % + C_2H_6 10 %, $\Delta V_{\text{GEM}} = 250 \text{ V}$)

4.2.3 Drift and Diffusion

Electron Drift

In an adequate electric field, the pairs of an electron and an ion, which are ionized by a charged particle, drift with the constant velocity. The ion drift velocity v_+ is described with the electric field intensity E and the gas pressure P : $v_+ = \mu_+ \frac{P}{E}$. Here, the constant μ_+ is the mobility, which depends on the gas.

On the other hand, an electron does not have a constant mobility, and the electron mobility complicatedly depends on both E and P . The electron drift velocity v_- is described such as:

$$v_- = \frac{eE}{m_e} \tau, \quad (4.1)$$

where, τ is the mean free time. Figure 4.21 shows the electron drift velocity as a function of the electric field. Because τ also depends on E/P , v_- depends on E/P . This figure says that the behavior of v_- strongly depends on the type of the gas even at the same E/P .

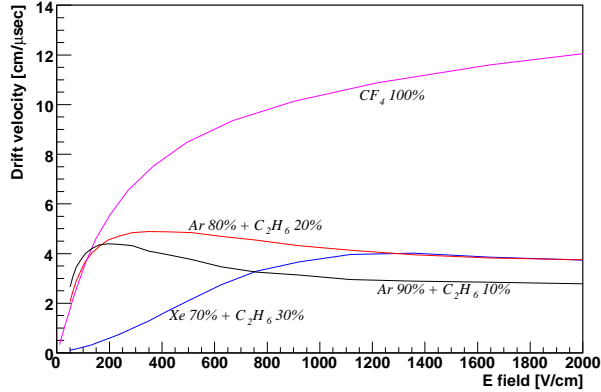


Figure 4.21: The electron drift velocity as a function of the electric field

Diffusion

Drifting electrons, which at first localize in the ionization point at time $t = 0$, gradually diffuse by the collisions with a gas molecule. At the time t and position x , the transverse diffusion of electrons in the width of dx is described by

$$dN = \frac{N}{\sqrt{4\pi Dt}} \exp\left(-\frac{x^2}{4Dt}\right) dx, \quad (4.2)$$

where N is the number of electrons, D is a diffusion constant. The diffusion constant depends on the gas condition, and also it depends on the electric field in the case of an electron. Figure 4.22 shows the standard deviation of the transverse diffusion, and Figure 4.23 shows that of the longitudinal diffusion. Since the diffusion of electrons limits the position resolution for the TPC, the a gas having a small diffusion, like CF_4 , is better as a TPC gas.

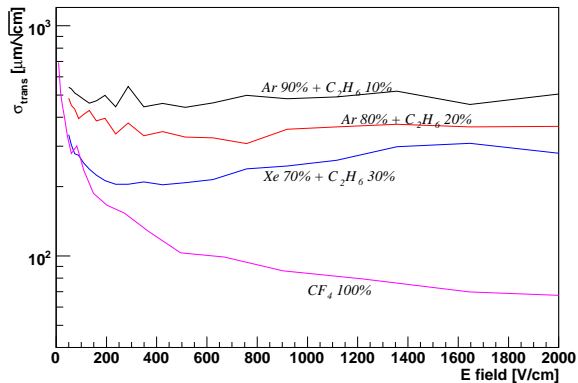


Figure 4.22: The standard deviation of transverse diffusion

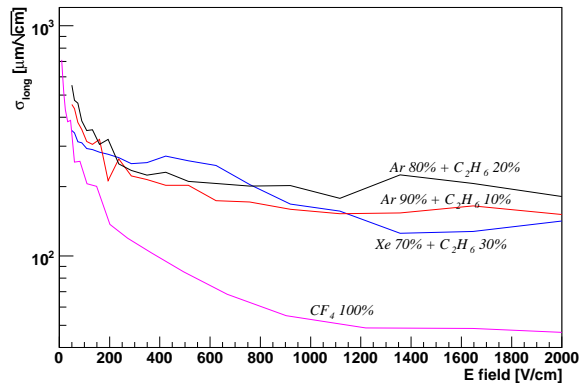


Figure 4.23: The standard deviation of longitudinal diffusion

4.2.4 Spectroscopy

The X-ray spectra were measured by the hybrid TPC with GEM and μ -PIC as shown in Figure 4.24. The signal to noise ratio is better than that with a single μ -PIC due to the higher gain. Since the TPC system has a large gas volume, TPC can detect comparatively high energy X-rays. Also the X-ray spectrum of 60 keV from ^{241}Am is shown in Figure 4.24. The $\text{CuK}\alpha$ fluorescence line is seen in this spectrum due to the irradiation of X-rays to μ -PIC/GEM copper electrodes.

Figure 4.25 shows the dependence of energy resolution on the energy, where the dotted line is got by fitting:

$$\left. \frac{\Delta E}{E} \right|_{\text{FWHM}} [\%] = 5.4 \times 10 \left(\frac{E}{\text{keV}} \right)^{-0.30} . \quad (4.3)$$

This energy resolution of TPC reaches to about 30 % at 6 keV.

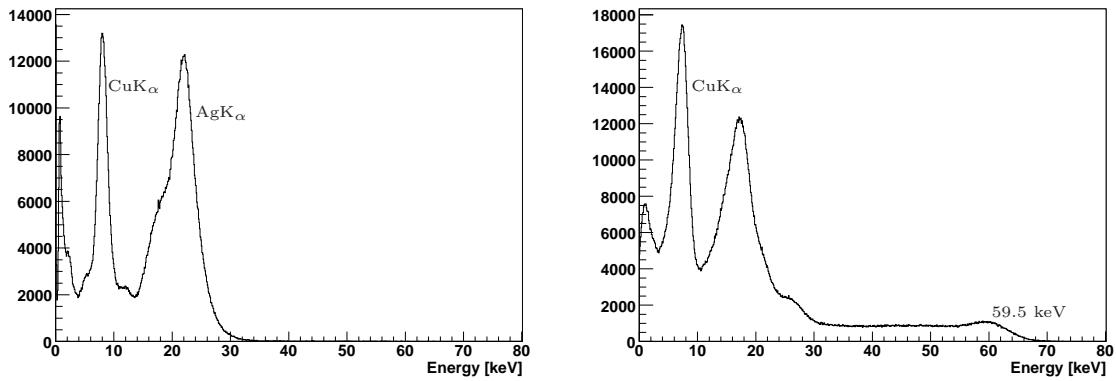


Figure 4.24: The X-ray spectra with μ -TPC (left: ^{109}Cd , right: ^{241}Am ; Ar 90 % + C_2H_6 10 %, 1 atm, gas flow)

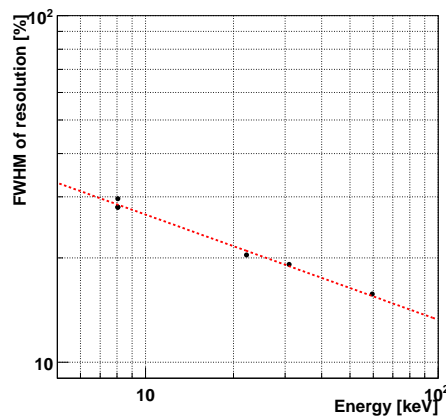


Figure 4.25: The dependence of energy resolution of the μ -TPC on incident photon energy

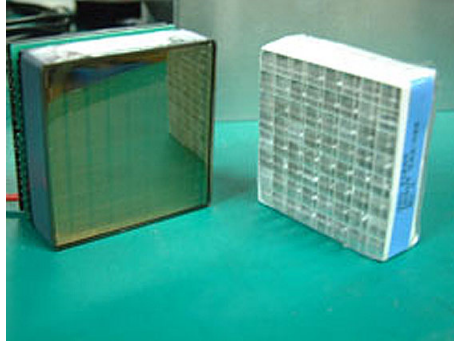


Figure 4.26: Hamamatsu multi-anode PMT H8500 (left) & GSO:Ce pixel array (right)

4.3 Scintillation Camera

Since a scintillator as an absorber of an MeV gamma-ray camera detects both the position and the energy, the stopping power of the absorber limits the detectable energy range of the MeV gamma-ray camera.

As a position sensitive detector, an Anger camera using a monolithic scintillator is a conventional but a powerful method. But if we use a larger and thicker scintillator, the scintillation camera would be a quite large and have huge background, which makes it difficult to coincide with a tracker. Furthermore, for the balloon/satellite loading, a large Anger camera has a high risk that a large monolithic scintillator might be broken by shock.

Another method is using an array of pixel scintillators. For a Pixel Scintillator Array (PSA), the position resolution is determined by the pixel size. PSA separates a large area of the gamma-ray camera to some units. A scintillator has a dead time of a few μsec for each hit. Since the detection area of an Anger camera is the monolithic scintillator, the pileup of the several signals easily happens for a strong irradiation. On the other hand, such a pileup hardly happens using the PSA, and thus the coinciding with a tracker is easy than the use of an Anger camera. Besides, PSA has a low risk for the break of the scintillator due to its divided structure. On the other hand, PSA needs a lot of readout electronics.

From above reasons, we selected a PSA method for our MeV gamma-ray camera, although the low power and compact readout system is necessary.

4.3.1 Scintillator & PMT

Table 4.1 lists the properties of various scintillators. As the scintillator for an absorber, the required properties are a good energy resolution and a high stopping power. For the use of the pixel structure, the scintillator can be easily handled. Also, for the balloon/satellite loading, the scintillator is required a radiation hardness. For these purposes, we selected GSO:Ce scintillator. Table 4.1 says GSO:Ce scintillator has high Z , a high density, a high stopping power, reasonable energy resolution, fast decay time, strong radiation hardness and no hygroscopic. Therefore GSO:Ce matches to PSA as an absorber of our MeV gamma-ray camera.

For a photon sensor of the scintillator, we selected a multi-anode Flat Panel PMT H8500 made by Hamamatsu Photonics (left of Figure 4.26). This PMT has 8×8 pixels with each size of $6 \times 6 \text{ mm}^2$ and geometrical area of $52 \times 52 \text{ mm}^2$, and its effective area thus is 89 %. The gain uniformity of H8500 is not so good, and the ratio of the maximum gain to the minimum one is about 3.

For matching the PMT pixel size with the scintillator pixel size, we selected a $6 \times 6 \text{ mm}^2$ GSO:Ce pixel, where 13 mm height is due to the radiation length of GSO:Ce. A GSO array consists of 8×8 pixels, and a reflector is inserted between each pixel (right of Figure 4.26).

Table 4.1: The properties of various scintillators [45]

scintillator	Density [g/cm ³]	Abs. coefficient [1/cm]	Decay time [ns]	wave length [nm]	light yield (relative)	hydroscopic	radiation hardness [Gray]	refraction index
NaI(Tl)	3.67	0.34	230	415	1	strong	10	1.85
CsI(Tl)	4.53	0.44	1050	550	0.85	weak	10	1.8
CsI(Na)	4.53	0.44	630	420	0.90	strong		1.8
BGO	7.13	0.92	300	480	0.07-0.12	no	10 ²⁻³	2.15
LSO:Ce	7.4	0.87	40	420	0.4-0.75	no	10 ⁵	1.82
YSO:Ce	4.45	0.38	40	420	0.3-0.45	no	10 ⁴	1.79
YAP:Ce	5.35	0.46	28	370	0.4	no	10 ²⁻³	1.94
YAG:Yb	4.57		3	330/500	0.02	no		1.82
GSO:Ce	6.71	0.70	30-60	440	0.18	no	> 10 ⁶	1.85
LGSO	7.2		43	420	0.4	no		
LaBr ₃ :Ce	5.3	0.45	28	385	1.30	strong		1.9
LaCl ₃ :Ce	3.79	0.34	26	385	0.7-0.9	strong		1.9
CWO	7.9	0.92	5000	475	0.3-0.4	no	10	2.3
PWO	8.28	1.15	< 3 < 20	430	0.04	no	10 ⁵⁻⁶	2.2
BaF ₂	4.89	0.48	0.6/620	220/310	5/16	no	10 ⁴⁻⁵	2.2

4.3.2 HV Operation/Readout System

For the reduction of the number of the readout channel, we use the resistor matrix board as shown in Figure 4.27, and obtain the position of a hit pixel using the Center Of Gravity (COG). On this board, the anode of 3 PMTs in horizontal rows and the interval of the edge of the column are connected with $100\ \Omega$ resistor chips respectively. Then, we get a hit position by reading 4 readouts from the corners. These readouts are connected to the preamplifier board, which has 4 preamplifiers having a time constant of $5.4\ \mu\text{sec}$, and the output of the preamplifier is fed into the shaper having a time constant of $0.5\ \mu\text{sec}$. Then the shaping signal is fed to the peak hold ADC. Also the summing signal of 4 preamplifier-outs is used for the generation of the trigger.

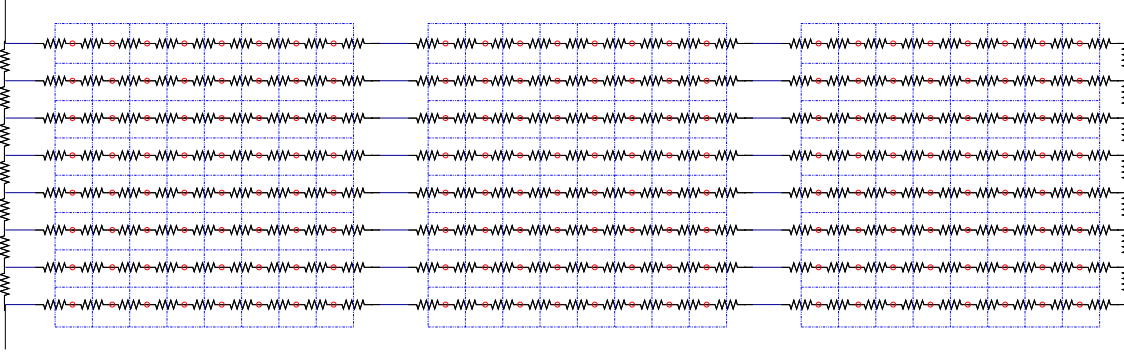


Figure 4.27: The resistor board

For the balloon/satellite loading, a compact high voltage power system for PMTs is inevitable. We selected EMCO Q12N-5 as a DC-HV converter (Figure 4.28), and its specification is listed up in Table 4.2. We control this DC-HV converter by supplying DC level from DAC, which is operated by a VME CPU. We connect this converter to PMT one by one, therefore we can control HV of each PMT individually.

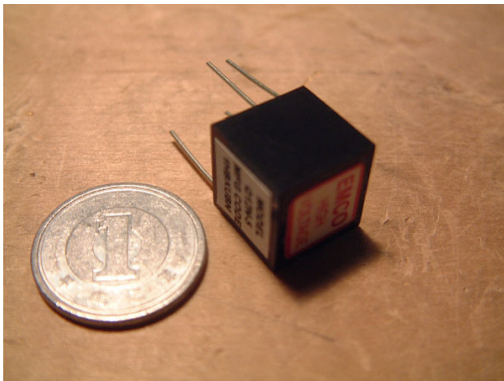


Figure 4.28: DC to HV converter (EMCO Q12N-5)

parameter	value
Input Voltage	0.7 - 5 V
Input Current	< 50 mA (No load) < 175 mA (Full load)
Output Voltage	0 - $-1.2\ \text{kV}$
Output Current	< 0.4 mA
Conversion Factor	$\sim 60\ \%$
Ripple Noise	< 0.25 %
Weight	4 g
Size	$1.27 \times 1.27 \times 1.27\ \text{cm}^3$
Operating Temp.	$-25 - +70\ ^\circ\text{C}$

Finally, we composite a compact GSO-PSA unit shown in Figure 4.29. One unit has 4 ch analog signals, 1 signal output line for the trigger, and 1 D-sub 9 pin power line (3 pairs from DAC and preamp power). By putting several GSO-PSA units around the tracker, a large area absorber are easily constructed.

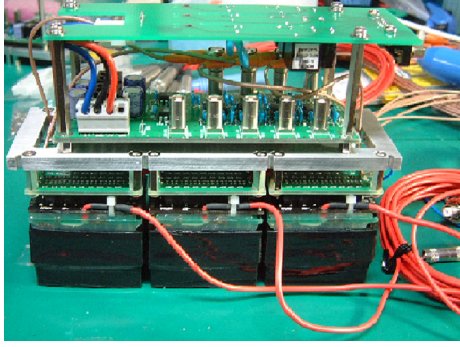


Figure 4.29: The photograph of one PSA unit

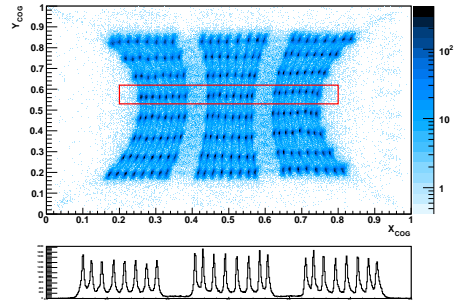


Figure 4.30: The COG image of GSO (upper) and the projection of the box-enclosed area (lower)

4.3.3 Image and Energy Spectrum

By illuminating the whole area of GSO-PSA by a radioactive source, we measure the image of the COG as shown in Figure 4.30, where we can distinguish each pixel clearly.

Figure 4.31 shows the ^{137}Cs spectrum obtained from the whole area of one unit, and the typical energy resolution is 11 % for 662 keV at FWHM. The energy dependence of the energy resolution is shown in Figure 4.32, In this Figure, the dotted line is fitted as

$$\left. \frac{\Delta E}{E} \right|_{\text{FWHM}} [\%] = 3.3 \times 10^2 \left(\frac{E}{\text{keV}} \right)^{-0.52} \quad (4.4)$$

Figure 4.33 shows the distribution of the gain of each pixel, and the RMS is ~ 0.23 . We found that the GSO absorber has a dynamic range of 80 keV - 1 MeV over the whole area.

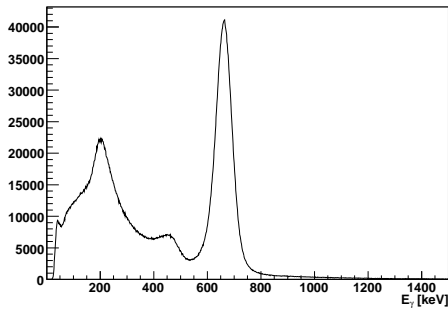


Figure 4.31: The spectrum of ^{137}Cs measured with the GSO-PSA

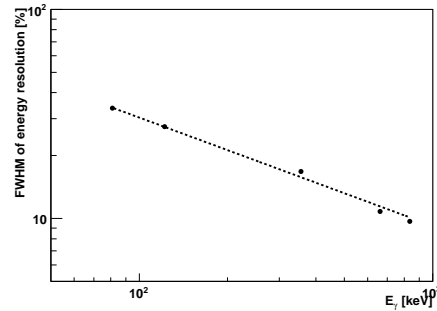


Figure 4.32: The energy resolution depending of the GSO-PSA on energy

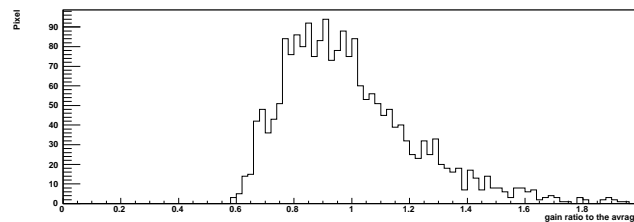


Figure 4.33: The gain distribution of each pixel of the GSO-PSA

Chapter 5

Tracking of Charged Particles

5.1 Tracking of Cosmic Muon

5.1.1 DAQ System for Muon Tracking

For a performance test of the μ -TPC, we measured the tracks of cosmic muons. We put plastic scintillators above and under the μ -TPC as shown in Figure 5.1, and took a coincidence of the upper and lower plastic scintillators as a μ -TPC trigger. This trigger was fed into the position encoder, and the encoder started to count 100 MHz clock from the trigger generating during 4 μ sec. When a μ -TPC signal came in the position encoder, the encoder stored the clock counter and the maximum/minimum number of the hit anode/cathode strip in FIFO of FPGA 7. If there is a coincidence of the anodes and the cathodes during clock counting, the encoder generated an interrupt signal to the VME CPU after the encoder outputs the hit informations to the memory module. After the CPU finished the data taking, CPU sent an acquisition end signal to the encoder, and the encoder cancels the veto signal for the next trigger.

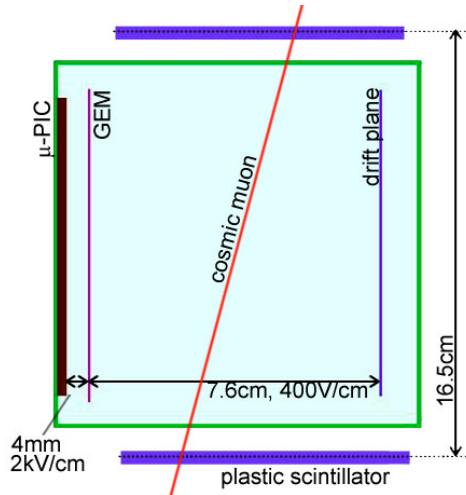


Figure 5.1: The setup for cosmic muon detection

As a gas of the TPC, Ar 90 % + C₂H₆ 10% was used in flow. The hybrid μ -TPC with GEM was operated with the gains of 10 for GEM ($\Delta V_{\text{GEM}} = 250$ V) and 2500 for μ -PIC ($V_{\text{Anode}} = 500$ V), respectively, and hence the total gain of 2.5×10^4 was achieved. The maximum drift length was 7.6 cm, and the electric field in the drift region was ~ 400 V/cm. Also the electric field of the induction from GEM was ~ 2 kV/cm.

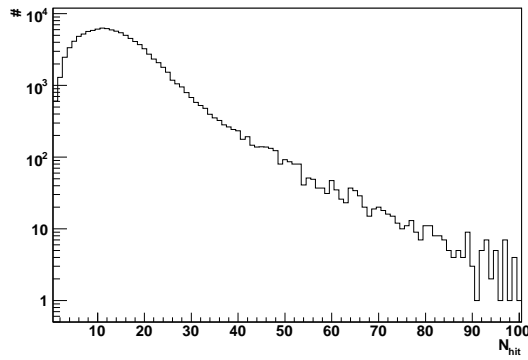


Figure 5.2: The histogram of hit points number N_{hit}

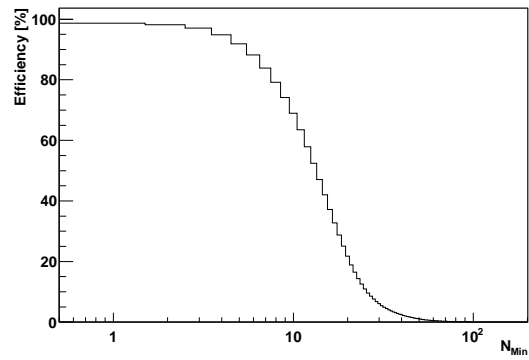


Figure 5.3: The tracking efficiency, which is the ratio of $N_{\text{hit}} \geq N_{\text{Min}}$ events to the trigger number

5.1.2 Tracks of Muon & Track Efficiency

Figure 5.2 is a histogram of the number of hit points (N_{hit}) for one muon track. The average of N_{hit} is 14.8 for a 10 cm muon track.

By considering the geometrical trigger efficiency (0.902), the detection efficiency, which is the ratio of the event number to the trigger number, is measured to be 98.7 %. Figure 5.3 shows the tracking efficiency, which is the ratio of number of $N_{\text{hit}} \geq N_{\text{Min}}$ events to the trigger of the coincidence of the plastic scintillators. The tracking efficiency of $N_{\text{hit}} \geq 3$ is 97.0 %, and that of $N_{\text{hit}} \geq 10$ is 69.0 %. Its reason is as follows. μ -TPC has a poor efficiency for the tracks running vertically or parallel in μ -PIC, and the major cosmic muon passing through the μ -PIC are near in parallel to the μ -PIC. Therefore, the tracking efficiency is not so good in this setup.

Figure 5.4 shows the examples of several tracks of cosmic muons in the μ -TPC. MIPs like cosmic muons create only 4 electrons by ionization during 400 μm , which is the pitch of μ -PIC pixels. Although it is thus difficult to detect MIPs by MPGD, μ -TPC can measure fine tracks of MIPs as shown in Figure 5.4.

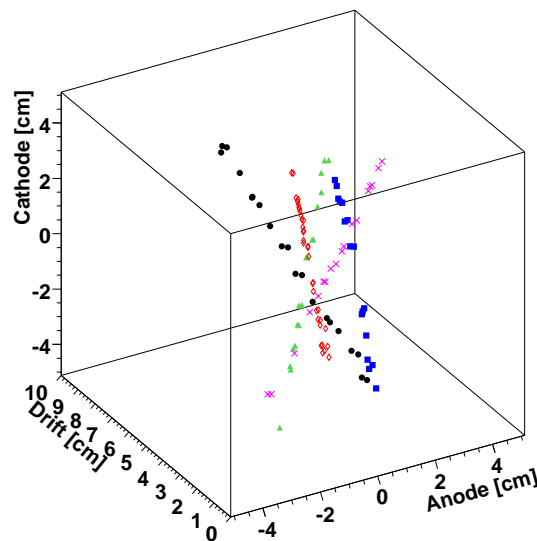


Figure 5.4: The track images of cosmic muons with μ -TPC

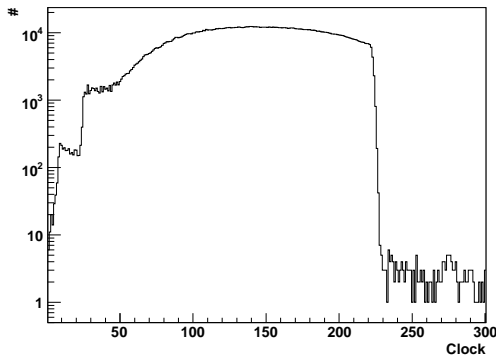
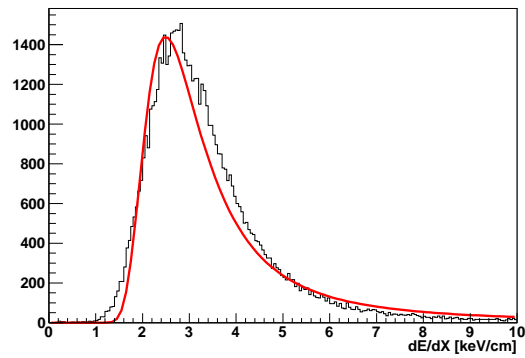


Figure 5.5: The histogram of clock counter

Figure 5.6: The dE/dX spectrum of cosmic muons. The solid curve is the best fit with a Landau distribution

5.1.3 Clock Counter Histogram

Figure 5.5 shows the distribution of the drift time of the μ -PIC. This distribution of the drift time looks to be divided into 4 regions: the clock of 0-8, 9-24, 25-225 and 226-400.

The events in the first region are pre-trigger events. Because the position encoder calculates the hit position in a pipeline processing and several clocks are required for the calculation, there is a few time latency before generating the trigger. The second region is due to the gap events. The seed electrons, which are ionized in the gap between μ -PIC and GEM, do not pass through GEM. Therefore, the gain is lower by a factor ~ 10 , and the signals of these electrons are so small that they hardly exceed the threshold. Then, the amount of gap events are quite less than those events in the drift region. In the third region, the events are generated in the drift region. Good events are ionized in the drift region, and multiplied by both GEM and μ -PIC. The final region consists of the drift-over events. These events are due to the random coincidence completely.

Because the time width of one clock is 10 nsec, the time width of the third region is 2 μ sec. The maximum drift length is 7.6 cm, and we thus get the drift velocity of 3.8 cm/ μ sec at ~ 400 V/cm. This value is consistent to the nominal one for the gas mixture in Figure 4.21.

5.1.4 dE/dX Spectrum

Figure 5.6 is the spectrum of the energy deposit per unit length dE/dX , and the solid curve is the best fit with the Landau distribution. This fitted Landau distribution has a peak of 2.6 keV/cm. On the other hand, the dE/dX of MIP in Ar gas is 2.5 keV/cm. Therefore this spectrum is well consistent to the energy deposit of MIP.

5.1.5 Position Resolution

For the measurement of the position resolution on tracking method, we obtained the distance between the hit points and the track line obtained by fitting. Figure 5.7 shows the distribution of the residuals, where data are fitted with a 2 dimensional Gaussian in circular polar coordinates:

$$P(r)dr = \frac{\sqrt{2\pi}}{\sigma_{\text{res}}^2} r \exp\left(-\frac{r^2}{2\sigma_{\text{res}}^2}\right) dr. \quad (5.1)$$

Obtained σ_{res} is 486 μ m. Although the diffusion constant σ is ~ 1 mm at the drift length of ~ 5 cm, the obtained σ_{res} is smaller than the diffusion σ because we use the center of the minimum hit strip and the maximum hit strip as a hit point.

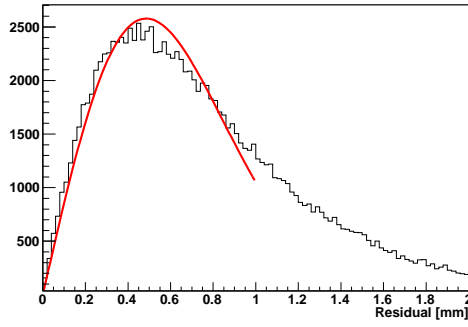


Figure 5.7: The histogram of residual between the obtained points and the fitted straight line. The solid line is obtained by fitting

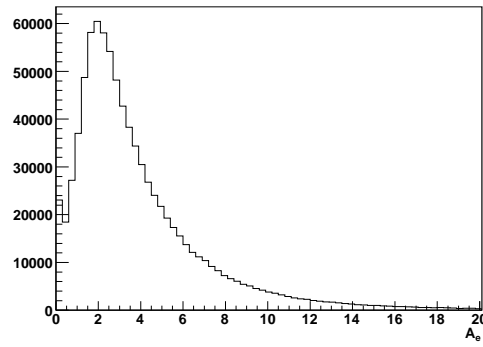


Figure 5.8: The histogram of the electron number for exceeding threshold A_e

5.1.6 Threshold

We estimated how much electrons are required to exceed the threshold in ASD chips. Assuming that the hit width, which is the distance between minimum and maximum hit strip, is due to the transverse diffusion, the number of electrons for exceeding threshold A_e is described as follows,

$$A_e = \frac{\epsilon \Delta l}{w} \int_{\frac{\max - \min}{2} - 0.5\text{strip}}^{\frac{\max - \min}{2} + 0.5\text{strip}} \frac{1}{\sqrt{2\pi}\sigma_{\text{trans}}} \exp\left(-\frac{x^2}{2\sigma_{\text{trans}}^2}\right) dx, \quad (5.2)$$

where ϵ is the energy deposit per unit length, Δl is the track length per clock and w is the average energy required to ionize one electron. Figure 5.8 is the histogram of A_e , and about 2 electrons are required to exceed the threshold.

5.2 Tracking of Recoil Electron

When μ -TPC is used as a tracker of the MeV gamma-ray camera, μ -TPC must track a low energy recoil electrons which is easily scattered in the gas. The electron's track looks winding even in the gas. Therefore it is very difficult to reconstruct a low energy electron track even with a gaseous detector. In this section, we will estimate the efficiency of tracking electron by a GEANT4 simulation. We simulate the electron track in the μ -TPC using the following parameters: the transverse diffusion of $\sigma_{\text{trans}} = 470 \mu\text{m}/\sqrt{\text{cm}}$, the longitudinal diffusion of $\sigma_{\text{long}} = 235 \mu\text{m}/\sqrt{\text{cm}}$, the time constant of preamplifier of 16 nsec and the 100 MHz encoding of the hit positions. Here the electron energy is distributed in the range between 0 - 300 keV. Also the gas is Ar 90 % + C₂H₆ 10 % at 1 atm.

In order to reconstruct the recoil electron track in the Compton camera, following 5 steps are proceeded in the analysis (Figure 5.9).

1. Fixing of the Track Points: In general, a drifted electron cloud extends over several strips. Then we record the five encoded values of a μ -TPC hit data, which consist of the clock counter, the maximum ID and the minimum ID of the anode strip, the maximum ID and the minimum ID of the cathode strip. Therefore we must determine the hit position on the extended hit strips.
2. Connecting: As shown in the left-lower of Figure 5.9, there are several connections between the hit points, and we have to find the correct one (see 5.2.2).

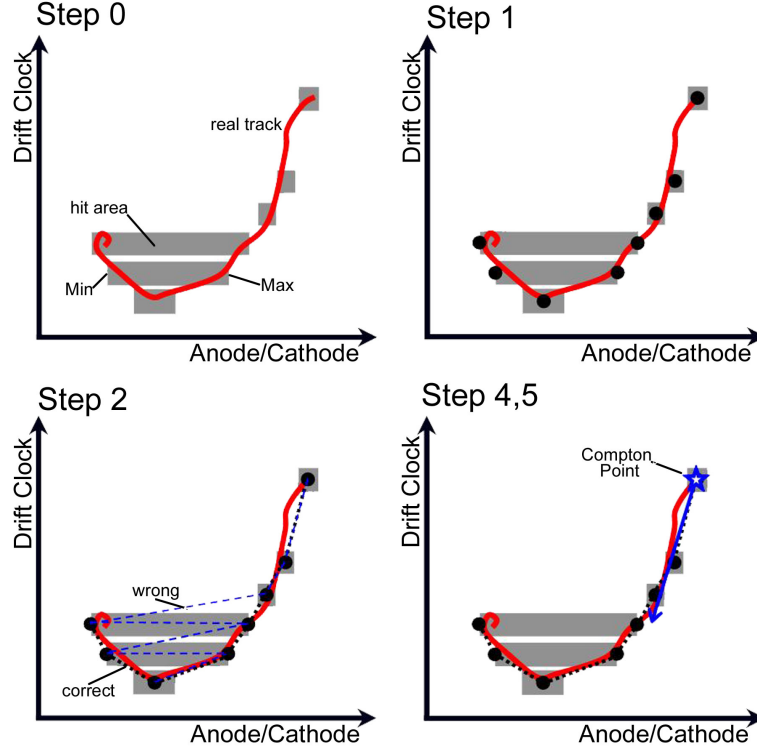


Figure 5.9: The schematic view of the process to reconstruct the recoil electron track. We obtain a minimum and a maximum of the hit strip number (Step 0). The first step is the determination of the track points. Next, we reconstruct the track by connecting the track points. Finally, we determine the initial/end point of the track and the initial direction.

3. Selection of the Stopping Electron: For the reconstruction of the incident gamma-ray, the energy of the recoil electron is needed. However, the recoil electron may escape from the fiducial volume of the TPC. Thus we must select the electron stopping in the μ -TPC.
4. Judgement of the initial/end point of the electron track
5. Determination of the recoil direction: We determine the direction of the recoil electron by fitting the initial part of the track with a straight line.

The analysis of the recoil electron track affects seriously to the efficiency and the angular resolution of the MeV Compton camera. Therefore, the study of the recoil electron tracking is very important for the gamma-ray reconstruction.

5.2.1 Fixing of the Track Points

When the width of the hit strips extends significantly, the extended hit point would include two or more track points. Then, for the electron tracking, we select the real track points under the conditions as follows.

- $\sqrt{(x_{\max} - x_{\min})^2 + (y_{\max} - y_{\min})^2} < 5\sigma_{\text{trans}}$: As a track point, we obtain the center of hit area, $(\frac{x_{\max} + x_{\min}}{2}, \frac{y_{\max} + y_{\min}}{2})$.
- $x_{\max} - x_{\min} < 3\sigma_{\text{trans}}$: We obtain two points, $(\frac{x_{\max} + x_{\min}}{2}, y_{\min})$ and $(\frac{x_{\max} + x_{\min}}{2}, y_{\max})$.
- $y_{\max} - y_{\min} < 3\sigma_{\text{trans}}$: We obtain two points, $(x_{\min}, \frac{y_{\max} + y_{\min}}{2})$ and $(x_{\max}, \frac{y_{\max} + y_{\min}}{2})$.

Here, x_{\min} and x_{\max} are the minimum ID and the maximum ID of the hit anode strip, respectively, and y_{\min} and y_{\max} are the minimum ID and the maximum ID of the hit cathode strip. The discrepancy between the obtained track points and the simulated electron track is shown in Figure 5.10. From this figure, the position resolution of the electron tracks is $\sim 500 \mu\text{m}$, which is nearly equal to the position resolution of the muon tracks (Figure 5.7). Also the ratio of the number of the used hit points (N_{use}) to the number of the all hit points (N_{hit}) is shown in Figure 5.11. This figure says that the events using all hit points are 70 % and the events using ≥ 80 % points are 90 %, by this method.

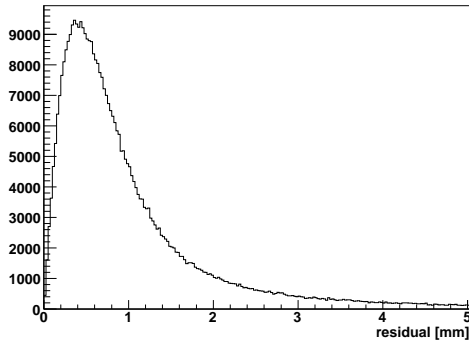


Figure 5.10: The position resolution of the electron tracks

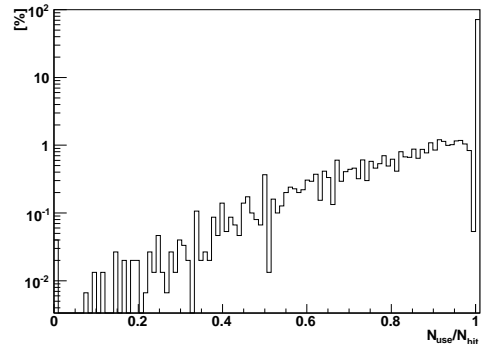


Figure 5.11: The ratio of the number of used hit data (N_{use}) to the number of all hit data (N_{hit})

5.2.2 Connection of the Points

For the search of the Compton point, the roughly sorting of the track points is needed. However, the sorting of the track points in the correct order is a very difficult problem. Then we calculate the nearly minimum length path as the approximate path by the method as follows.

1. Combine the Nearest Point: As the first step of the sorting, we reconstruct the track of $(n + 1)$ points by the combination of the nearest point to the track of reconstructed using n points. We obtain the initial track by the repeat of such point adding.
2. 2-opt and Or-opt: For the improvement of the track, we use the 2-opt method and the Or-opt method, with using the random number.
 - 2-opt: We select two points at random, and reverse the order between the two points, as shown in Figure 5.12.
 - Or-opt: We select two points at random and cut the part track between the two points, and we insert the part track at the random selected point of the residual track, as shown in Figure 5.13.

We select two methods at random, and we compare the length of the new track with that of the previous track. If the length of the new track is shorter than the previous one, we adopt the new track order. We repeat the search of the shorter track until finding no shorter length.

Figure 5.14 shows the absolute value of the correlation coefficient (C_{cor}) between the correct order of the hit points and the obtained one. In this figure, the events of $C_{\text{cor}} > 0.8$ is 75 %. Thus this sorting method looks effectively functional.

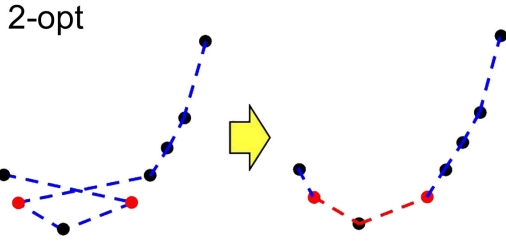


Figure 5.12: The schematic view of 2-opt

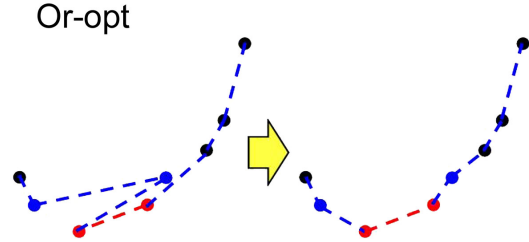


Figure 5.13: The schematic view of Or-opt

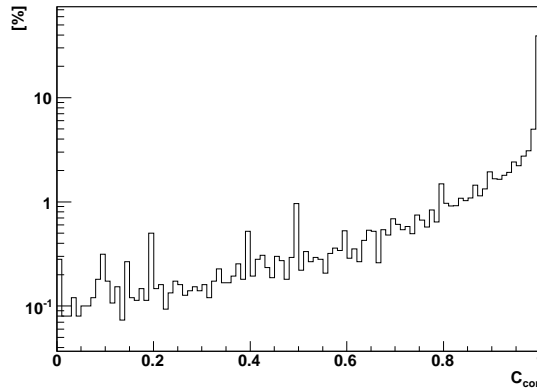


Figure 5.14: The correlation coefficient between the correct rank and the obtained rank

5.2.3 Selection of the Stopping Electron

For the selection of the stopping electron events, we study the correlation between the energy and the track length. Figure 5.15 shows this correlation in an ideal detector. In this figure, the events on the solid line correspond to the dE/dX of MIPs. If the electrons deposit all of the energy in the μ -TPC, such events concentrate along the dashed line. The dashed line is described as

$$L_e[\text{cm}] = 3.60 \times 10^{-3} \left(\frac{K_e}{\text{keV}} \right)^{1.82}, \quad (5.3)$$

where L_e is the electron track length, and K_e is the electron energy.

On the other hand, taking into account of the position resolution and the efficiency of the sorting in the simulation, the correlation between the energy and the track length is changed as shown in Figure 5.16. The solid line and the dashed line are the same as Figure 5.15. Figure 5.16 says that the correlation of the energy and the track length is kept even if the position resolution and the efficiency of sorting are considered. Therefore, the events of the stopping electrons are selected by collecting the events near the dashed line.

5.2.4 Judgement of the Initial/End Point of the Track

For the judgement of the initial/end point of the electron tracks, we use the ratio of the track length to the distance of the edge point and the middle point. Because the effect of multiple scattering increases in the end of the track, this ratio of the end part is expected larger than that of the initial part. The judgement efficiency by this ratio is $\sim 60\%$. Figure 5.17 shows the

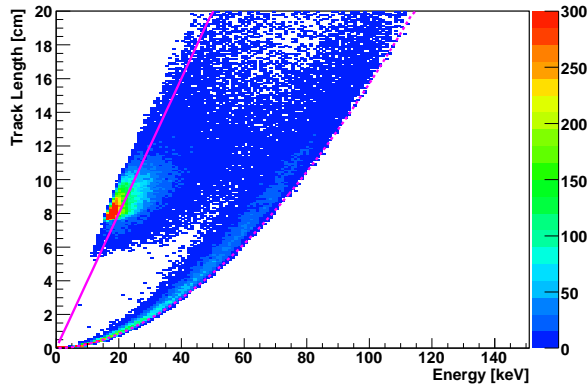


Figure 5.15: The relation of the electron energy and track length in the ideal. The tilt of the solid line means the dE/dX of MIPs. If the electron deposits all of the energy, the relation of the energy and the track length is on the dashed-line.

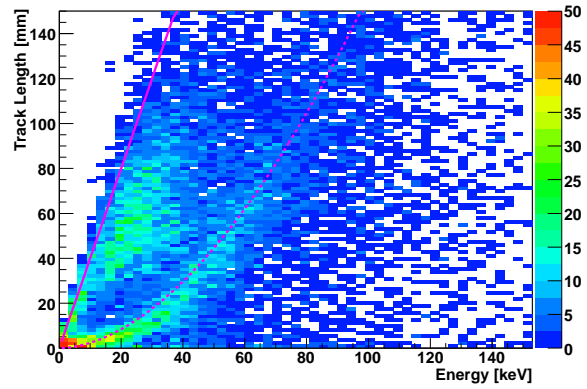


Figure 5.16: The relation of the energy and the track length with the position resolution of the μ -TPC. The tilt of the solid line means the dE/dX of MIPs, and the dashed line means the stopping electrons.

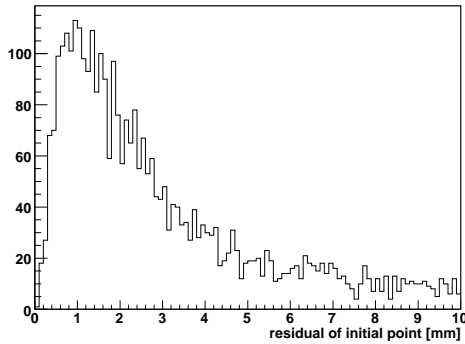


Figure 5.17: The position resolution of the initial point

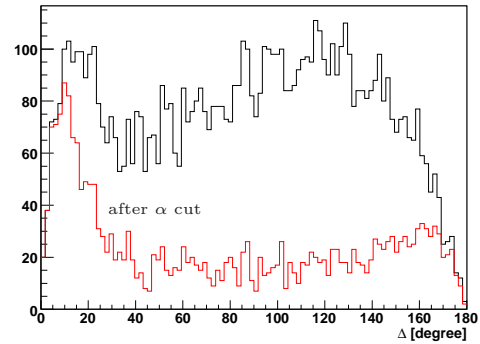


Figure 5.18: The difference angle between the obtained angle and the direction of the electron ejecting.

residuals of the initial point, which has been judged to be the front one by this ratio, and the resolution of the initial point is ~ 1 mm.

5.2.5 Determination of the Recoil Direction

The final step is the determination of the direction of the recoil electron. For obtaining of the direction, we use the initial part of the track consisting of several track points, of which length is less than 1.5 cm, and then we determine the direction with fitting by a straight line. Figure 5.18 shows the difference angle between the obtained direction and the direction of electron ejecting. In the gamma-ray reconstruction, since we require the Compton scattering kinematics (α cut), the events of the correctly obtained direction are selected. The ejected direction of a part of the events is obtained within the angular resolution of $\sim 30^\circ$ in simulation, and hence the resolution of the SPD is expected to be about 60° at FWHM.

Chapter 6

Prototype Camera

6.1 Prototype Setup

In order to investigate a fundamental feature of the electron tracking Compton camera, we constructed a prototype Compton camera consisting of a 10 cm μ -TPC and a GSO-PSA. In this chapter, I describe the system and the performance of the prototype camera.

6.1.1 Absorber & Tracker of Prototype

The specifications of the absorber and the tracker in the prototype camera are summarized in Table 6.1 and Table 6.2, respectively. Also Figures 6.1 and 6.2 are the photographs of the bottom absorber and the side absorber, respectively. Using this absorber and this tracker, we constructed an MeV gamma-ray camera.

Table 6.1: The specification of prototype absorber

Scintillator	GSO:Ce
PMT	Hamamatsu Photonics H8500
Pixel Size	$6 \times 6 \times 13 \text{ mm}^3$
Bottom Camera	$158 \times 158 \text{ mm}^2$ (3×3 PMTs)
Side Camera	$158 \times 52 \text{ mm}^2 \times 4$ surfaces (3×1 PMTs $\times 4$)
Energy Range	80 - 900 keV
Energy Resolution	$\text{FWHM}[\%] = 3.3 \times 10^2 (E_\gamma/\text{keV})^{-0.52}$

Table 6.2: The specification of prototype tracker

Gas	Ar 90 % + C ₂ H ₆ 10 %, gas flow 1 atm
Volume	$10 \times 10 \times 7.6 \text{ cm}^3$
Fiducial Volume	$8 \times 8 \times 7.6 \text{ cm}^3$
Gas Gain	~ 25000
Drift Velocity	3.8 cm/ μ sec
Encoding Clock	100 MHz
Position Resolution	$\sim 485 \mu\text{m}$
Threshold	2 electron
Energy Resolution	$\text{FWHM}[\%] = 5.4 \times 10 \left(\frac{K_e}{\text{keV}}\right)^{-0.30}$
Length of stopped electron	$L_e[\text{cm}] = 3.60 \times 10^{-3} \left(\frac{K_e}{\text{keV}}\right)^{1.82}$

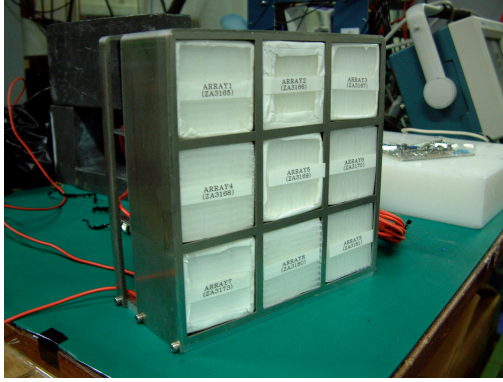


Figure 6.1: The photograph of the bottom absorber

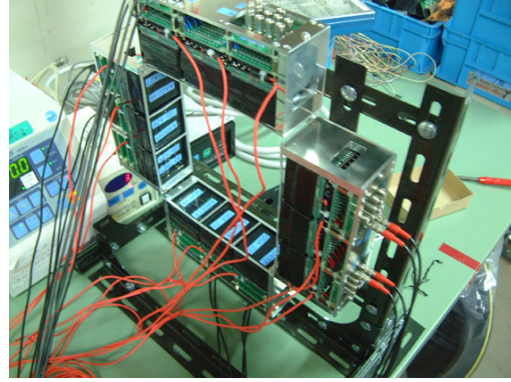


Figure 6.2: The photograph of the side absorber

6.1.2 Alignment of Prototype Camera

When we observe the gamma-rays coming from a quite far point source such as a celestial object, the gamma-ray comes into a detector in parallel. But, in the laboratory, it is very difficult to get the parallel light using a radioactive source. For simulated parallel light ($< 1^\circ$), we have to put a radioactive isotope at ~ 5 m from the detector, and the intensity of gamma-rays is too weak. Then, we put a radioactive isotope at the appropriate distance from the camera, and get an image by taking the cross point of the source plane and the reconstructed line, as shown in Figure 6.3, where we use this distance as a known parameter.

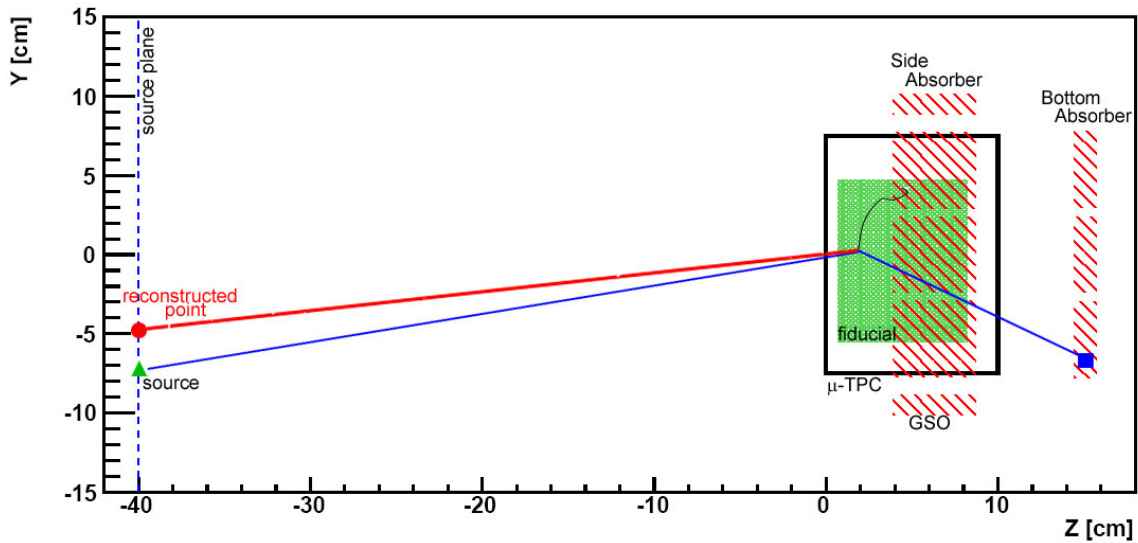


Figure 6.3: The side view of alignment

Figure 6.3 shows the alignment of the prototype camera, and Figure 6.4 is the photograph of the prototype camera. The distance between the camera window and the source plane is ~ 40 cm. Around this camera, there is no shield and no veto counter.

6.1.3 Data Acquisition System of Prototype Camera

Figure 6.5 is the diagram of the data acquisition system for the prototype camera. As a trigger of the data acquisition, we use a sum of the signals from 4 corners of a GSO unit. However,

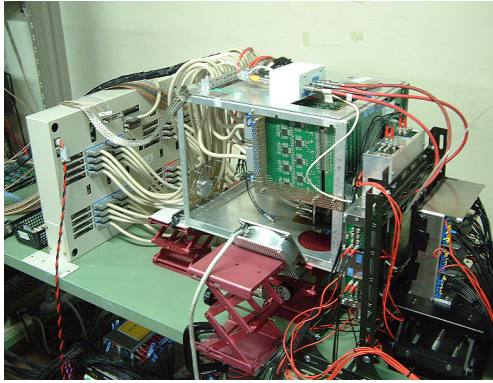


Figure 6.4: The photograph of prototype camera

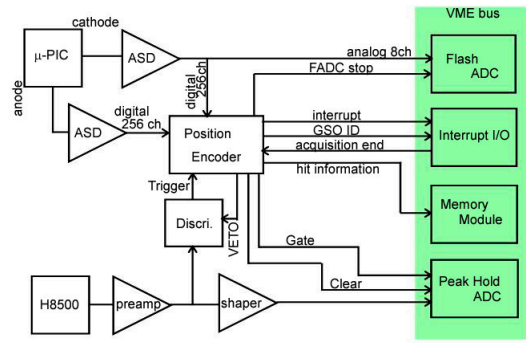


Figure 6.5: The diagram of data acquisition system

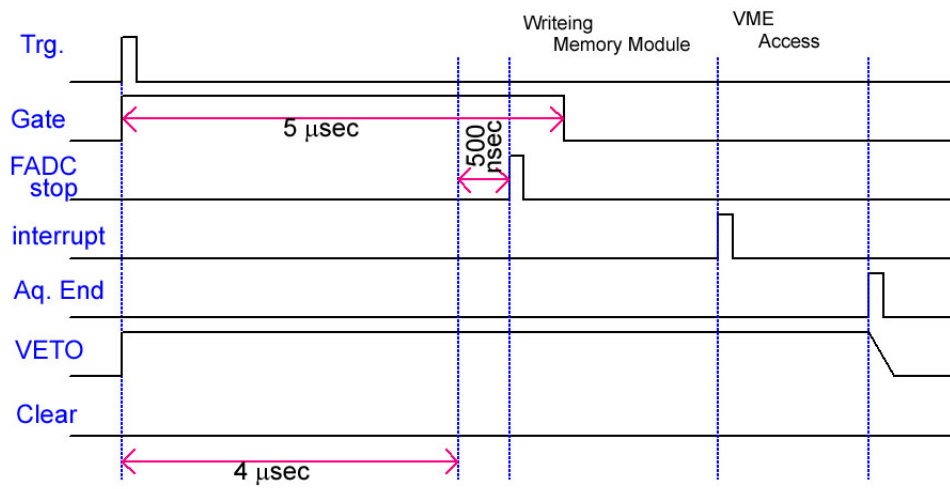


Figure 6.6: The timing chart of various signals in the data acquisition cycle

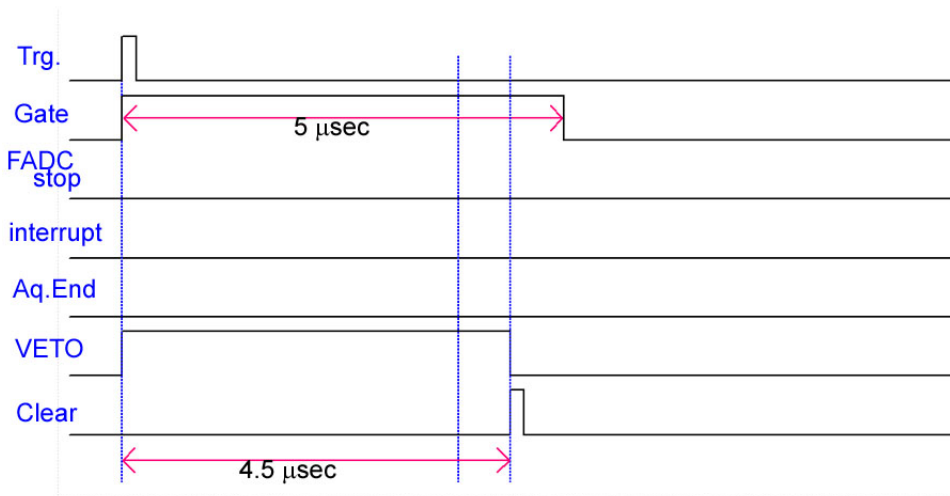


Figure 6.7: The timing chart of various signals in the clear cycle

since the tracker is a gaseous TPC, most of the incident gamma-rays would pass through the TPC and interact with the GSO scintillators. Therefore, the most of the triggered events do not have the TPC data. Then we clear the GSO data when the triggered event does not have a TPC data. The timing charts in the data acquisition cycle and the clear cycle are shown in Figures 6.6 and 6.7, respectively.

A generated trigger is fed to the position encoder. When this trigger comes into the position encoder, the encoder generates a gate signal for the peak hold ADCs, and also starts to count a 100 MHz clock. In counting the clock, the encoder waits the signal from the μ -TPC during 4 μ sec. In the case of no TPC signal, the encoder sends a clear signal to the peak hold ADC for canceling the held data, and then clears the veto signal for a next trigger. On the other hand, in the case of a signal coming, the encoder accumulates the hit information during 4 μ sec from the trigger and sends it to the memory module. Then it sends a stop signal to the Flash ADC at 4.5 μ sec. After the data transfer to the memory module, the encoder makes an interrupt to the VME CPU. Then the VME CPU takes the data of the memory module, peak hold ADCs and flash ADCs. Finally, the CPU sends the acquisition end signal to the encoder. If the encoder catches the end signal, the encoder clears the veto signal for a next trigger. The position encoder also makes the signal about the ID of the hit GSO unit, which let us know which GSO unit made the trigger.

6.2 Reconstruction of Gamma-Ray

6.2.1 Event Selection

When we reconstruct the incident gamma-rays with (3.1) and (3.2), we select the real Compton events by applying the following criteria.

- Number of the Triggered GSO Units: A real Compton scattering event must have one electron track in TPC and one hit GSO unit. Thus, the number of the triggered GSO units is one in each real Compton event. If that number is more than two, the event is due to the background such as a charged particle event, a multiple scattering event or a random coincidence.
- Rejection of Low Energy Electron: Because the electron with the energy less than 15 keV is affected by multiple scattering, the accuracy of the determination of the direction of the recoil electron is very poor. On the other hand, for the determination of the recoil direction, we require three points of the electron track at least. Therefore, we require $K_e > 15$ keV and $N_{\text{hit}} > 3$.
- Fully Electron Contained Events: For the reconstruction of the incident gamma-ray, the energy of the recoil electron is required. However, the radiation length of a gas is so long that the recoil electron may escape from the drift volume of the TPC. Therefore, we must require the containment of the full track of the recoil electron in the μ -TPC. Then, we define the fiducial volume of the μ -TPC and the initial point of the electron track must be contained in it. Also, for the selection of the stopped electron events, we require (5.3).
- Compton Scattering Kinematics: With the reconstruction of the incident gamma-ray, we obtain the scatter angle by (3.4). Because the $\cos \phi$ must be between -1 and 1 , following relation is required,

$$0 \leq \frac{m_e c^2}{E_\gamma + K_e} \frac{K_e}{E_\gamma} \leq 2. \quad (6.1)$$

20050818/per7 track_01-0444

 source: ^{137}Cs 662 keV

 E_0 : 629.9 keV

 α_{kin} : 88.9°

 E_γ : 551.9 keV

 α_{geo} : 79.8°

 K_e : 78.1 keV

 ϕ : 27.7°

 ψ : 61.2°

- : source position
- ★ : reconst. point
- : absorbed point
- ▲ : Compton point

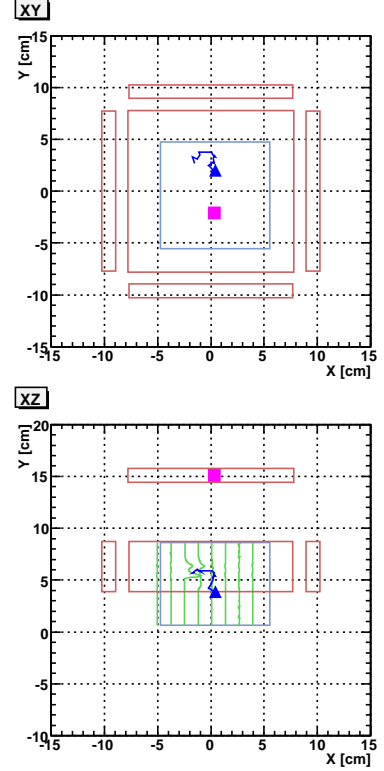
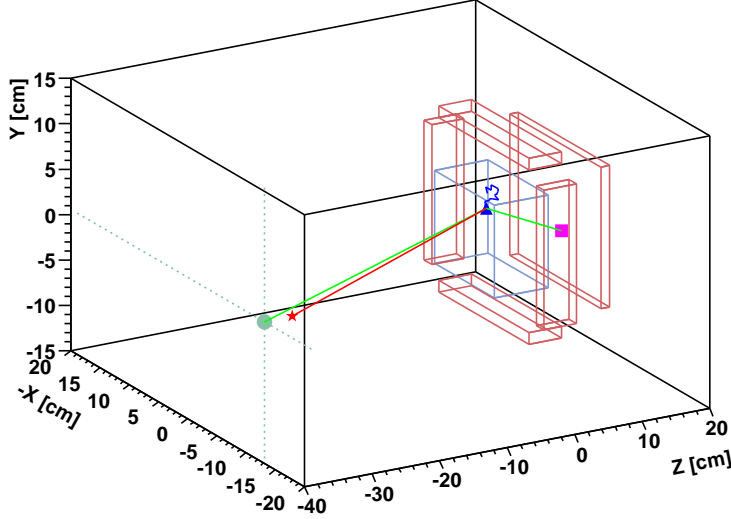


Figure 6.8: The typical event of the reconstructed gamma-ray

For matching to the kinematics of Compton scattering, we select events by α . The incident direction is described by the summing of the momenta,

$$\vec{s}_{\text{kin}} = \frac{E_\gamma}{E_\gamma + K_e} \vec{g} + \frac{\sqrt{K_e(K_e + 2m_e c^2)}}{E_\gamma + K_e} \vec{e}. \quad (6.2)$$

For a real Compton scattering event, \vec{s}_{kin} is a unit vector within the measurement errors. Then, as the α cut, we require the following condition,

$$|\vec{s}_{\text{kin}}| - 1 \leq \Delta. \quad (6.3)$$

6.2.2 Reconstructed Gamma-Rays

Figure 6.8 is an event display for the typical Compton event measured by this prototype detector, where we find the energy and track of the recoil electron, the energy and absorbed point of scattered gamma-ray. We can check that the Compton scattering is reconstructed correctly. Moreover, the source position is also reconstructed accurately.

With changing the source position, we measured the movement of the images as shown in Figure 6.9. All images have a peak near the real source position. On the other hand, Figure 6.10 shows the obtained images of the different energy gamma-rays. It is clearly seen that the peak of the obtained image spreads for the lower energy of the incident gamma-rays.

Two different sources of a ^{137}Cs (662 keV) and a ^{54}Mn (835 keV) were put at (4cm, 4.5cm) and (-4cm, -4.5cm), respectively, and we obtained the spectrum as shown in the left of Figure 6.11. The peaks of 662 keV and 835 keV are clearly seen in this spectrum, and the continuum component of the gamma-rays scattered at the outside of the camera is also seen under 600 keV. On the other hand, the Compton edge is not seen in this histogram, because this camera measures both the recoil electron and the scattered gamma-ray.

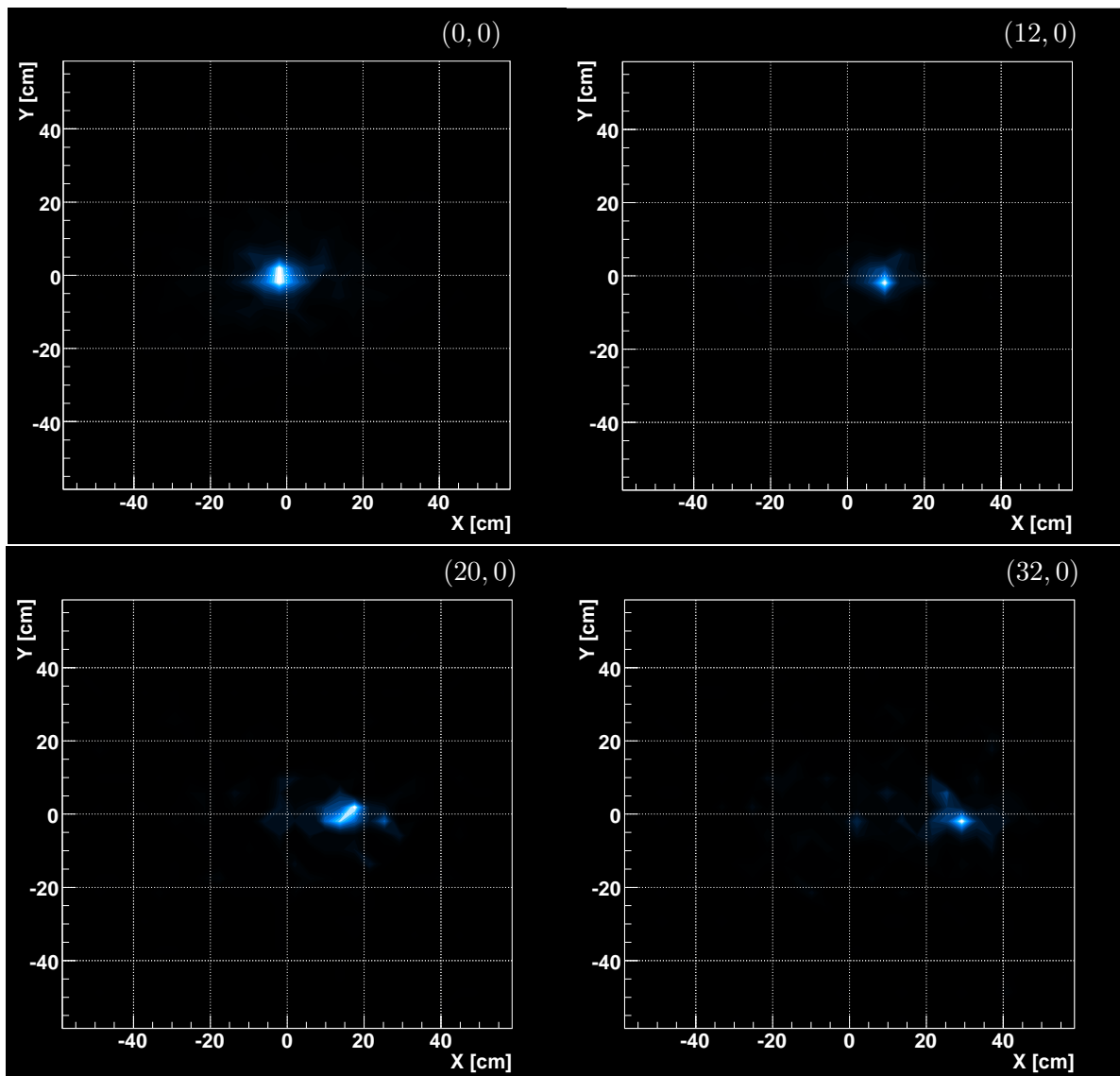


Figure 6.9: The obtained images of the different source positions. The gamma-rays sources of all images are ^{137}Cs , and the energy range is 613 - 711 keV.

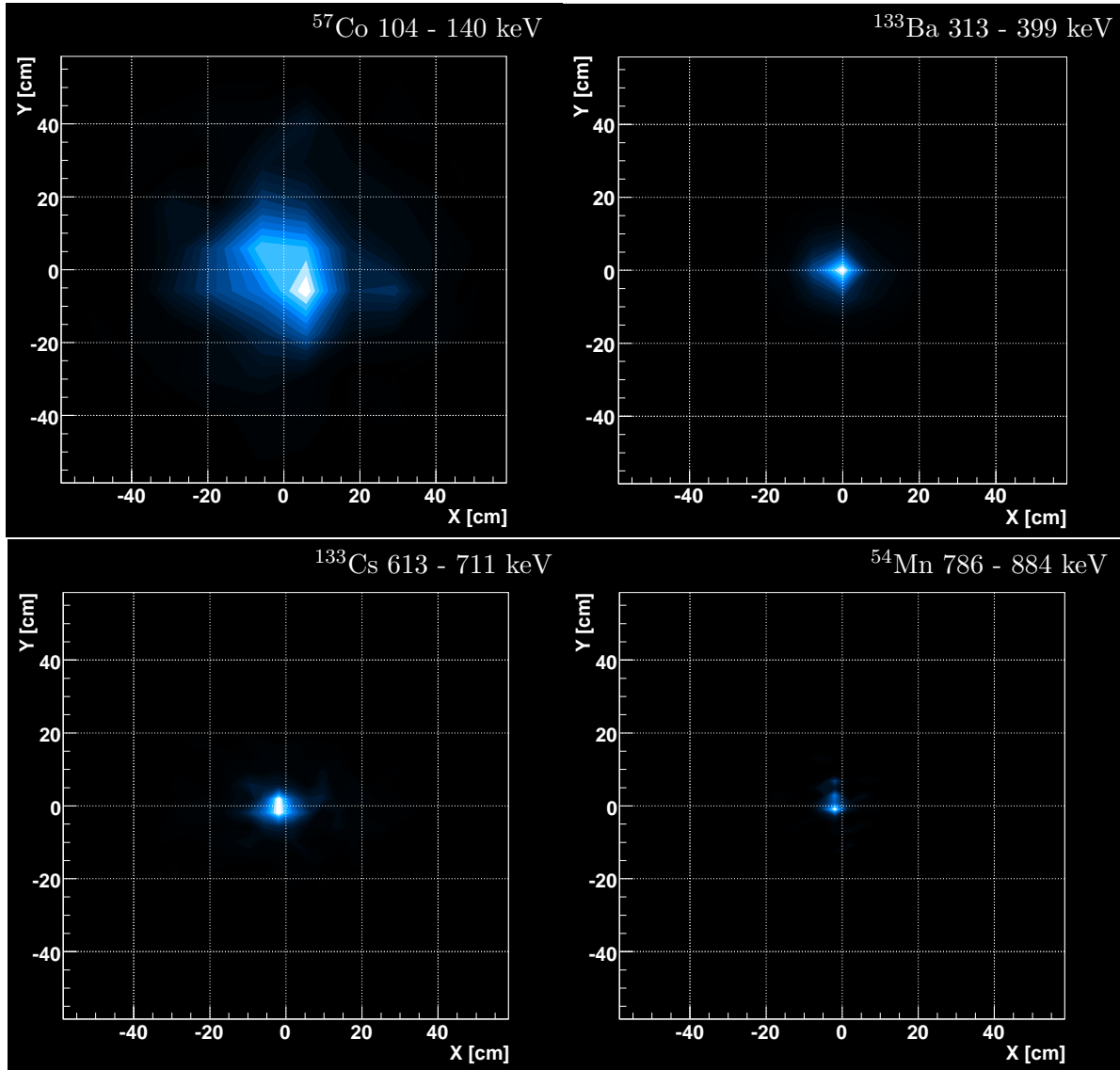


Figure 6.10: The obtained images of several different sources. The source position of all image are (0cm,0cm).

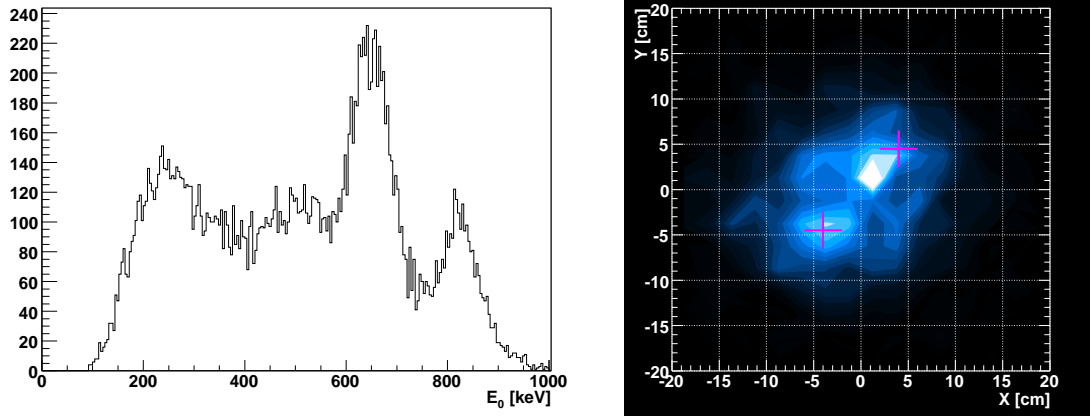


Figure 6.11: The obtained spectrum and the image by the prototype camera. We put a ^{137}Cs (662 keV) and a ^{54}Mn (835 keV) at (4cm, 4.5cm) and (-4cm, -4.5cm), respectively.

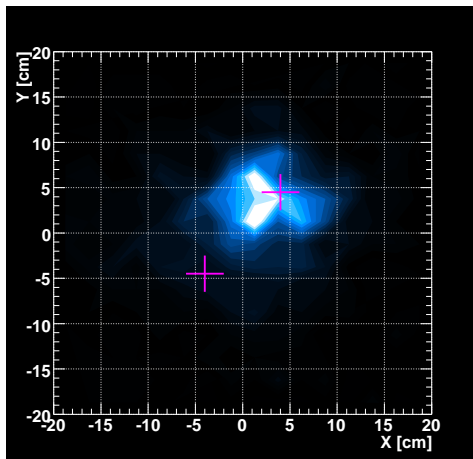


Figure 6.12: The image in the energy range of 613 - 711 keV

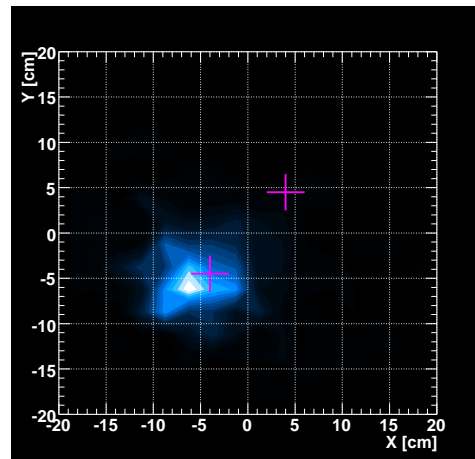


Figure 6.13: The image in the energy range of 785 - 885 keV

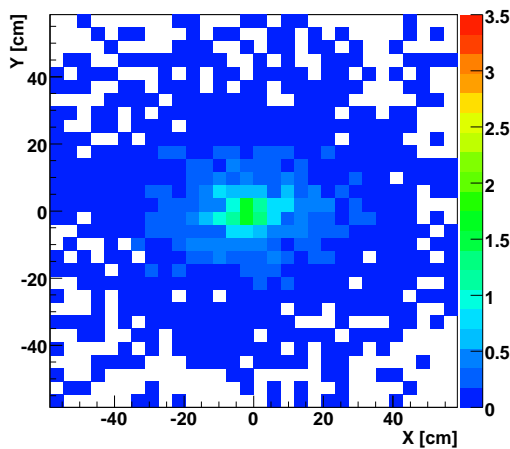


Figure 6.14: The normalized image of ^{137}Cs without α cut (613 - 711 keV)

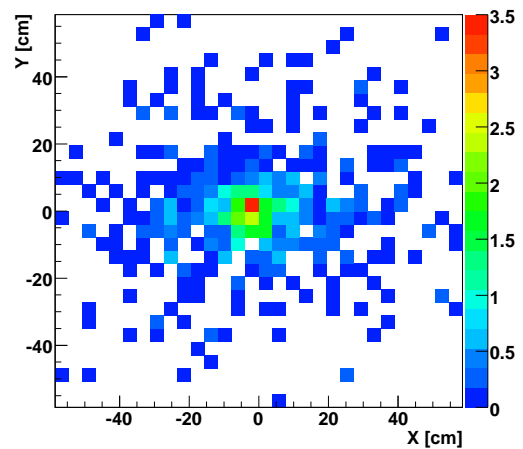


Figure 6.15: The normalized image of ^{137}Cs with α cut (613 - 711 keV)

The right of Figure 6.11 is the obtained image by this measurement. This image has peaks near the ^{137}Cs and ^{54}Mn . On the other hand, by applying the energy cut of 613 - 711 keV and 785 - 885 keV, the obtained images are Figure 6.12 and 6.13, respectively. Both images have an unique peak near the gamma-ray source corresponding to the energy range. Therefore, the prototype camera can separate multi-energy sources using the energy information.

6.2.3 Effect of α Cut

Figures 6.14 and 6.15 are the normalized images before and after α cut, respectively, where the source position is (0cm,0cm). In both images, the white region means 0 photons. Comparing these images, although both images have a peak near the source position, the spread of the image becomes narrow and the signal to noise ratio is quite improved, after applying the α cut.

6.2.4 Comparison with Classical Compton Imaging

For the comparison with the classical Compton imaging, which has no information of the direction of the recoil electron, we analyzed the same data by the classical method and our method. The left of Figure 6.16 is obtained by the classical method, and the right figure is obtained by our method. From these images, it is clearly seen that the image obtained by our method has less background than that obtained by classical method, which indicates the usefulness of the electron tracking.

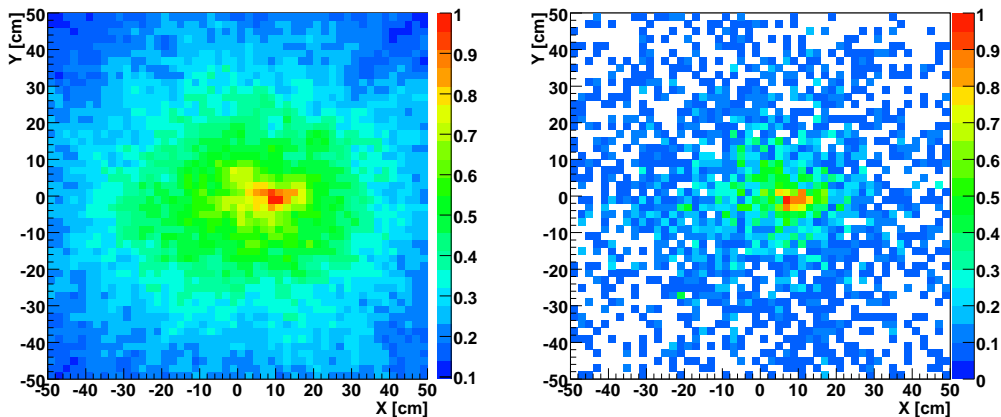


Figure 6.16: The comparison of the image by the classical Compton imaging (left) and the image by the electron tracking Compton imaging (right). The gamma-ray source is ^{137}Cs at (12cm, 0cm).

6.3 Performance of Prototype Camera

Figure 6.17 shows the energy spectrum under each event selection, and Figure 6.18 shows the energy resolutions of the μ -TPC, the GSO-PSA, and the combined one, where the energy resolution of our Compton camera was found to be limited by the that of GSO-PSA.

Figure 6.19 shows the resolution of the ARM $\Delta\phi_{\text{ARM}}$, and Figure 6.20 shows that of the SPD $\Delta\nu_{\text{SPD}}$. We obtained the resolution of the ARM by fitting with a lorentzian, and obtained the resolution of the SPD by fitting with the combination of a gaussian and constant component. Figure 6.21 shows the energy dependence of the resolution of ARM and SPD. The resolution of the ARM becomes better as the energy of the incident gamma-ray increases, because it depends

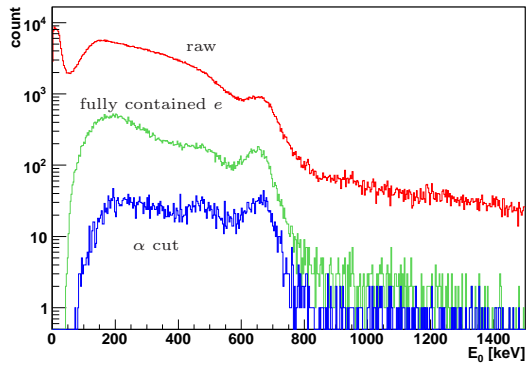


Figure 6.17: The spectra of the sum energy of μ -TPC and GSO-PSA under each event selection (^{137}Cs).

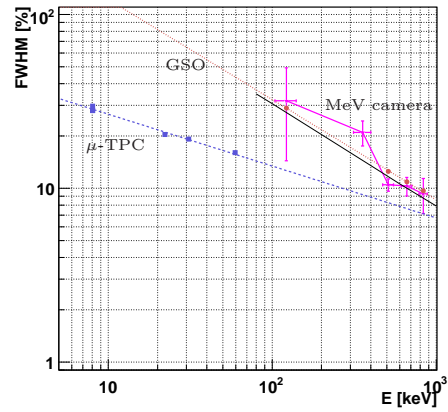


Figure 6.18: The energy resolution of the μ -TPC, the GSO-PSA and the Compton camera.

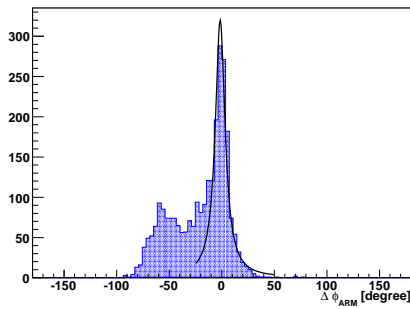


Figure 6.19: The histogram of the uncertainty of ARM (^{133}Ba , 313 - 399 keV). The solid line is obtained by fitting with a Lorentzian.

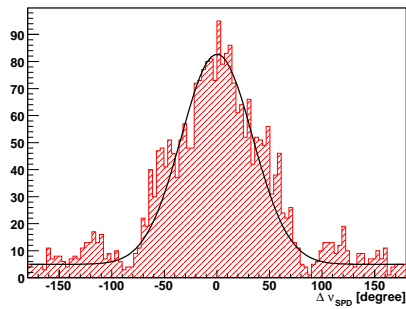


Figure 6.20: The histogram of the uncertainty of SPD (^{133}Ba , 313 - 399 keV). The solid line is obtained by fitting with the combination of a gaussian and constant.

on the energy resolution of the absorber and the tracker. On the other hand, FWHM of the SPD is nearly constant. This reason is that the detectable energy range of the recoil electron has little change with the energy of the incident gamma-rays, because that range is limited by the drift volume.

The detection efficiency of on-axis source is shown in Figure 6.22. The prototype camera has the maximum efficiency of 3×10^{-5} at about 350 keV, and has the energy range from 100 keV to 850 keV. Figure 6.23 shows the dependence of the effective area on the zenith angle. This figure says that the FWHM of the effective area is $\sim 70^\circ$, therefore the FOV of the prototype is about 1 str.

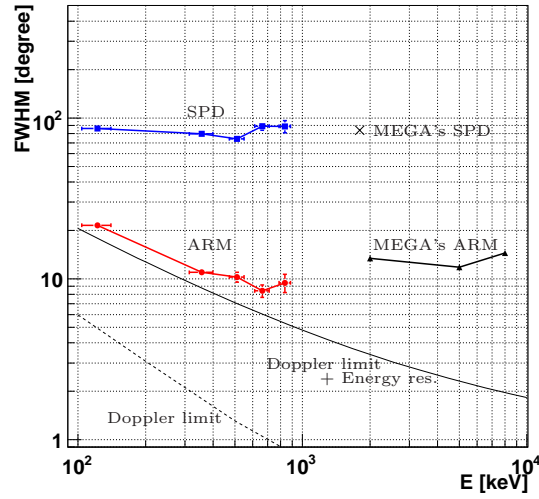


Figure 6.21: The energy dependence of the resolution of ARM and SPD. For the comparison, the resolutions of MEGA detector in the electron tracking mode are also plotted. The circles and the boxes are the FWHM of the ARM and the SPD of our camera respectively, and the triangles are the FWHM of the ARM of MEGA in the electron tracking mode. The cross is the two times of the HWHM of the SPD of MEGA. The dashed-line is the intrinsic limit of ARM by Doppler broadening in an Ar gas. Also, the solid line is the calculated ARM resolution with considering of Doppler broadening and the energy resolution of μ -TPC and GSO.

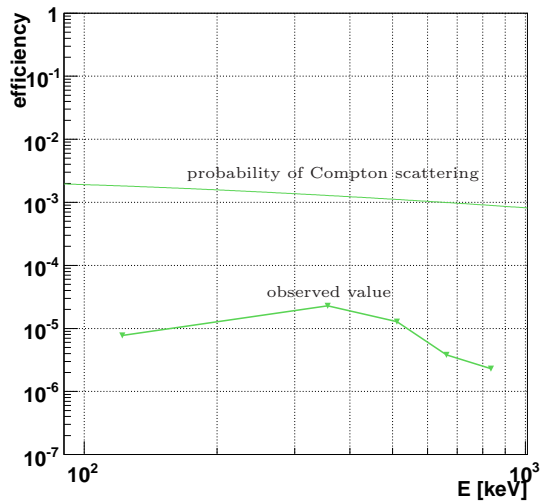


Figure 6.22: The dependence of the detection efficiency on the energy of the incident gamma-rays. The solid line is the Compton scattering probability in an Ar gas of 8 cm depth.

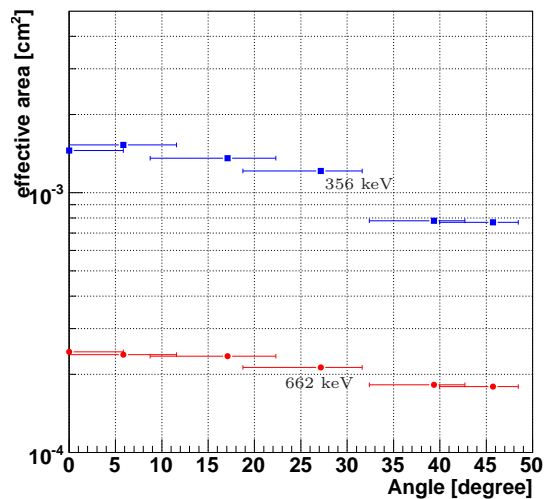


Figure 6.23: The dependence of the effective area on the zenith angle

Chapter 7

Flight Model Detector

7.1 Design of Flight Model

For the MeV gamma-ray observation in astronomy, we must launch this detector in space. Then, for the future observation in spacecraft loading, we have a plan of the balloon experiments, Sub-MeV gamma-ray Imaging Loaded-on-balloon Experiment (SMILE). The SMILE plan consists of 3 steps. At the first step, we confirm the gamma-ray detection using this camera for observing diffuse cosmic gamma-rays and secondary ones generated by the collision between high energy cosmic-rays and nuclei in the air. The second step will be the observation of bright sources, like Crab or Cyg X-1, in the short time of about 6 hours using a larger detector ($\sim 30 \times 30 \times 30$ cm³). The final step will be the observation of several sources in the long time more than a few days.

This work is the first step of the SMILE project, and concretely we aimed the following items;

1. Operation of μ -TPC & Gamma-Ray Detection at High Altitude: The μ -TPC is our original detector and has no flight experience. At the very high altitude, the cosmic-rays including the heavy ion come and deposit large amount of their energy in the detector. Therefore we must study the performance of μ -PIC and GEM for such charged particles. Although we have already measured the gamma-ray detection on the ground using the prototype camera. We have to check the performance of our camera for detecting celestial gamma-rays in such condition.
2. Observation of Diffuse Cosmic Gamma-Rays and Atmospheric Gamma-Rays: For the future observation, it is necessary to know how much background gamma-rays from the air affects. As the background gamma-rays, there are atmospheric gamma-rays and the gamma-rays produced by the interaction of cosmic-ray with the gondola. Then, by measuring the variation of gamma-ray flux depending on the altitude, we aim to measure both diffuse cosmic gamma-rays and atmospheric gamma-rays separately.

We construct a flight model detector to match with these purposes.

7.1.1 Cosmic-Ray Fluxes at Balloon Altitude

Figure 7.1 shows the spectra of diffuse cosmic X/gamma-rays reported by various balloon experiments [46], where the fitting for those data is described as

$$\left(\frac{dN_\gamma}{dE}\right)_{\text{cosmic}} = 30 \times E^{-2.0 \pm 0.2} \text{ photons cm}^{-2}\text{sec}^{-1}\text{str}^{-1}\text{keV}^{-1}. \quad (7.1)$$

When cosmic gamma-rays pass through the air, a part of them are attenuated by the atmospheric depth or scattered in the air. Therefore, the flux of diffuse cosmic gamma-ray is changed as:

$$\left(\frac{dN_\gamma}{dE}\right)'_{\text{cosmic}} = (1 + p(z, E)) \exp(-z/\tau) \left(\frac{dN_\gamma}{dE}\right)_{\text{cosmic}}, \quad (7.2)$$

where z and τ is the atmospheric depth and the mean free pass of the total attenuation in the air, respectively. $p(z, E)$ is the ratio of the scattered component to the gamma-rays reaching the detector without any interactions. For example, $p(100\text{keV}) \sim 1$ and $p(1\text{MeV}) \sim 0.25$ at $z \sim 10\text{g/cm}^2$ [46, 47]. Also this ratio has the dependence of $p(z, E) \propto \log(1 + z/\tau_{\text{abs}})$ on the atmospheric depth [48], where τ_{abs} is the mean free pass of the absorption in the air.

On the other hand, the spectra of atmospheric gamma-rays, secondary proton, secondary electron and secondary positron in the air shower depend on the geomagnetic latitude [49]. At the Sanriku Balloon Center (geomagnetic latitude: 30.4°) and $z = 3.8\text{g/cm}^2$, those spectra is described as

$$\left(\frac{dN_\gamma}{dE}\right)_{\text{atmos}} = 250 \left(\frac{E}{\text{MeV}}\right)^{-1.7} + 1.14 \times 10^5 \left(\frac{E}{\text{MeV}}\right)^{-2.5} e^{-\left(\frac{E}{120\text{MeV}}\right)^{-1.5}}, \quad (7.3)$$

$$\left(\frac{dN_p}{dE}\right)_{\text{atmos}} = 0.1 \left(\frac{E}{100\text{MeV}}\right)^{-1.18} \quad 100\text{MeV} \leq E \leq 400\text{GeV}, \quad (7.4)$$

$$\left(\frac{dN_{e^-}}{dE}\right)_{\text{atmos}} = 0.3 \left(\frac{E}{100\text{MeV}}\right)^{-2.7} \quad 100\text{MeV} \leq E, \quad (7.5)$$

$$\left(\frac{dN_{e^+}}{dE}\right)_{\text{atmos}} = 1.66 \left(\frac{dN_{e^-}}{dE}\right)_{\text{atmos}}, \quad (7.6)$$

in unit of photons $\text{sec}^{-1} \text{m}^{-2} \text{str}^{-1} \text{MeV}^{-1}$, respectively. Below 100 MeV, the spectra of proton and electron/positron were assumed by the extrapolation from the flux in the higher energy region as

$$\left(\frac{dN_p}{dE}\right)_{\text{atmos}} = 0.1 \left(\frac{E}{100\text{MeV}}\right)^{-1}, \quad (7.7)$$

$$\left(\frac{dN_{e^-}}{dE}\right)_{\text{atmos}} = 0.3 \left(\frac{E}{100\text{MeV}}\right)^{-1}. \quad (7.8)$$

These spectra are shown in Figure 7.2. In the following simulation, we use these spectra.

7.1.2 Design of Flight Model for First Flight

Our advanced Compton camera, however, has a low detection efficiency because of the gaseous Compton target. In order to increase the efficiency, we used a Xe TPC gas in the flight model tracker instead of Ar, which has a higher cross section of Compton scattering. Another improvement is the increase of the drift volume from $10 \times 10 \times 8 \text{ cm}^3$ to $10 \times 10 \times 14 \text{ cm}^3$, which increases twice the detection efficiency. However, the increase of the drift length needs the increase of the area of GSO units. Finally, we determined the design of MeV gamma-ray camera in Figure 7.3.

7.1.3 Particle Incoming to Detector

Since it is very difficult to operate the detector and the electronics in a vacuum, a pressure vessel to seal them in is necessary. Then we construct an Al vessel with the diameter of 1 m, the height of 1.4 m and the thickness of 3 mm, which has an attenuation factor of 13 % for 100 keV and 5 % for 1 MeV. In order to estimate how much particle will come into the detector by

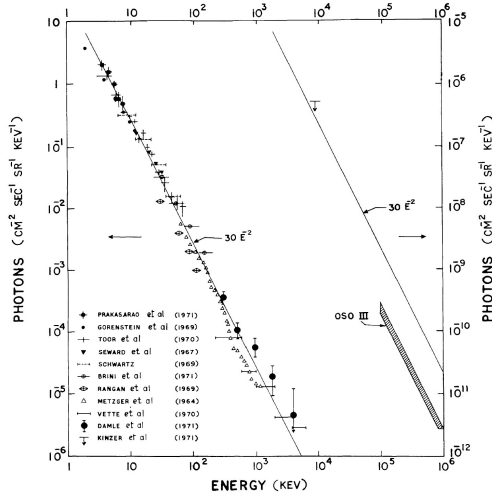


Figure 7.1: The diffuse cosmic X/gamma-ray spectra reported by various experiment [46]

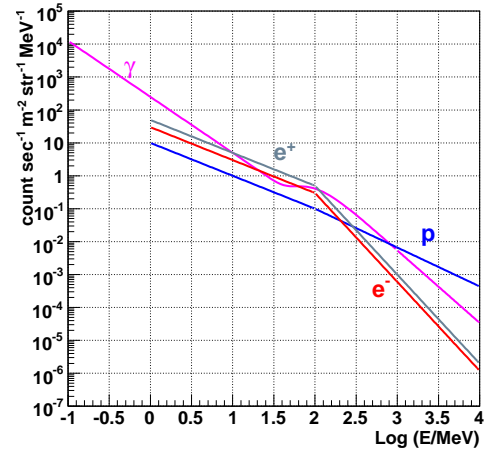


Figure 7.2: The spectrum of atmospheric charged particles and atmospheric gamma-rays

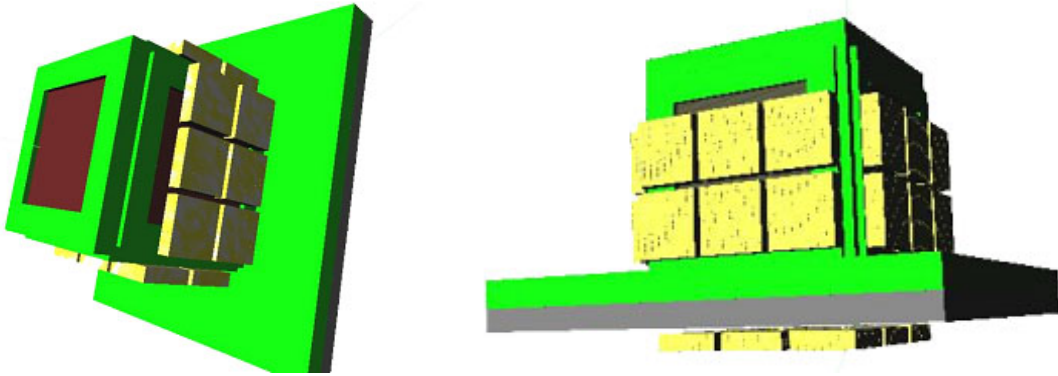


Figure 7.3: The schematic view of flight model detector

simulation, the source particle were generated from the zenith direction with the spectra shown in Figure 7.2. As the sensitive area, we assumed a 30 cm cube at upper half of the inside of the vessel, and count the particles coming into this sensitive cube as shown in Figure 7.4.

Then the obtained spectra for the various particles are shown in Figure 7.5. From Figure 7.5, the dominant component is found gamma-rays. But, because our detector has a low efficiency for gamma-rays, the detected rate for gamma-rays must be ~ 1 Hz. On the other hand, since the efficiency for the charged particles is nearly 1, the trigger rate of the charged particles is expected to be a few kHz. Therefore, if we use a simple trigger system, almost all triggered events would be occupied by charged particles, and the live time would be dramatically decreased. For this reason, we must adopt a sophisticated trigger system to reject charged particles.

Since a minimum ionizing particle typically deposits an energy of 890 keV/mm in the GSO scintillator, the energy deposit in our GSO unit by charged particles reaches 12 MeV. On the other hand, the flight model detector is designed to detect the gamma-rays below 1 MeV. Therefore, with the upper threshold of about 1 MeV, the charged particles would be easily separated by the gamma-rays detected in GSO, because the quenching factor of the general scintillator, which is the light yield of photon to proton, is about 0.1. Then, we adopt two thresholds for GSO units: the lower one is for the trigger generation, and another one is for the veto of charged particles. Also we placed a thin plastic scintillator over the tracker as a veto for

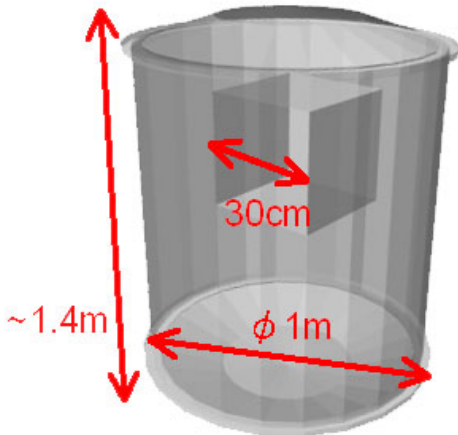


Figure 7.4: The schematic view of the pressure vessel. we deal the 30 cm cube in this vessel as a sensitive area.

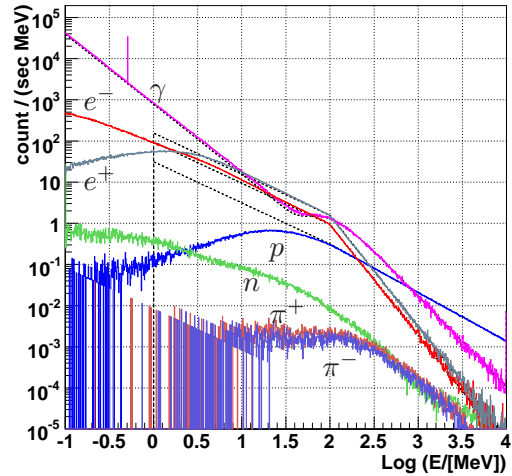


Figure 7.5: The spectra of incoming particles. The dashed lines are count rates of source flux into $30 \times 30 \text{ cm}^2$.

downward charged particles.

7.1.4 Expectation of Gamma-Ray Detection

To simulate the performance of our camera, we constructed an MeV gamma-ray camera with a TPC with a Xe gas and GSO units in the simulation, of which properties are summarized in Table 7.4 and Table 4.1. In the GEANT4 simulation, we considered Doppler broadening, multiple scattering in the TPC gas, the alignment, the position encoding of μ -TPC and the energy resolution of both μ -TPC and GSO. However, we did not consider the diffusion of the electron cloud and the response of preamplifier because of the reasonable calculation time.

Figures 7.6 and 7.7 show the dependences of the detection efficiency on the incident gamma-ray energy and the dependence of the effective area on the incident angle, respectively. As shown in Figure 7.6, a detection efficiency of the flight model is estimated $\sim 10^{-4}$, and the energy range from 100 keV to 1 MeV is expected to be measured. Moreover, from Figure 7.7, the effective area is decreased a half at the zenith angle of $\sim 60^\circ$, and the FOV of this detector is estimated about 3 str.

Using above results, the expected photon flux of the cosmic gamma-ray is presented in Table 7.1, and about 100 photons would be detected during 3 hours observation at the altitude of 35 km. On the other hand, as the altitude decreases, the less number of cosmic diffuse gamma-rays would come and the more number of atmospheric gamma-ray would come into the detector. Table 7.2 summarized the expectation of the photon flux at various altitude during 3 hours observation. Consequently, we note that the total detected photon flux would not be changed so much, but only the ratio of cosmic and atmospheric gamma-ray would be changed.

7.2 Data Acquisition of Flight Model Detector

Figure 7.8 is the block diagram of the data acquisition system of the SMILE. This system is based on the system of the prototype camera, and the veto system for the charged particles was added. In addition, this system has a GPS module, a scaler for the status monitoring, and also a discriminator for the remote control of the threshold. The CPU of the system is a VME bus

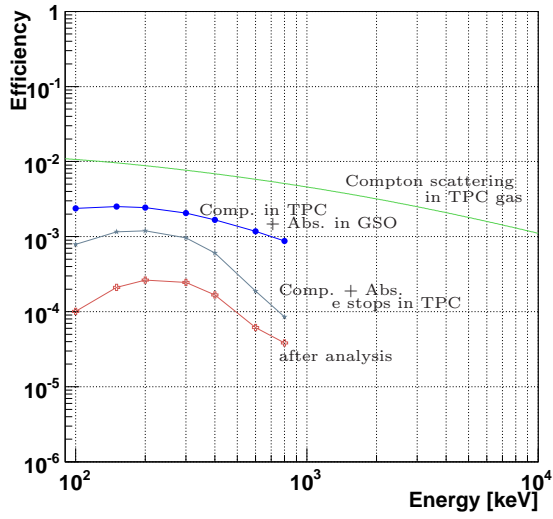


Figure 7.6: The simulated detection efficiency as a function of the incident gamma-ray energy. The incident angle is 0°

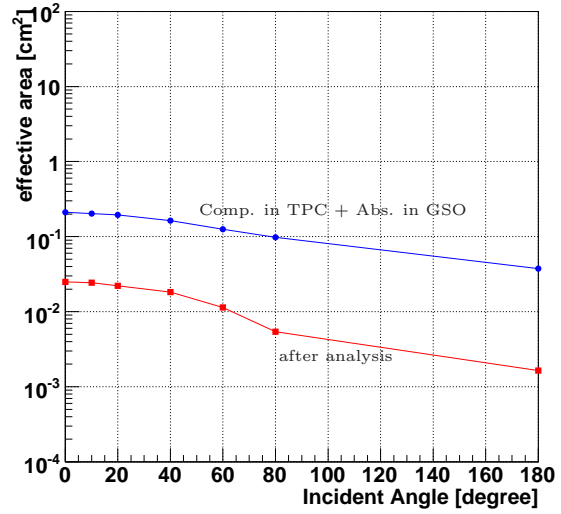


Figure 7.7: The simulated effective area as a function of the incident angle. The incident gamma-ray energy is 300 keV.

Table 7.1: The expectation of the detected photon number of cosmic gamma-ray for 3 hours level flight at the altitude of 35 km

Energy [keV]	Flux [$\gamma / (\text{cm}^2 \text{ sec str})$]	p^\dagger	Efficiency	Vessel attenuate	Number
100 - 200	1.50×10^{-1}	0.686	2.11×10^{-4}	0.894	57.1
200 - 400	7.50×10^{-2}	0.560	2.50×10^{-4}	0.919	37.9
400 - 600	2.50×10^{-2}	0.424	1.70×10^{-4}	0.930	8.46
600 - 750	1.00×10^{-2}	0.338	6.13×10^{-5}	0.939	1.26
750 - 900	6.67×10^{-3}	0.264	3.85×10^{-5}	0.946	.532

\dagger : p is the ratio of the scattered component to the gamma-rays reaching the detector without any interactions.

Table 7.2: The expectation of detected photon number at various altitude during 3 hours

Altitude [km]	Pressure [g/cm ²]	Cosmic	Atmospheric	by charged particle	All
30	12.2	69.5	185	21.0	275
32	9.07	86.5	137	15.6	239
33	7.83	93.7	119	13.5	226
34	6.77	99.9	103	11.6	214
35	5.86	105	88.7	10.1	204
37	4.42	113	66.9	7.60	188

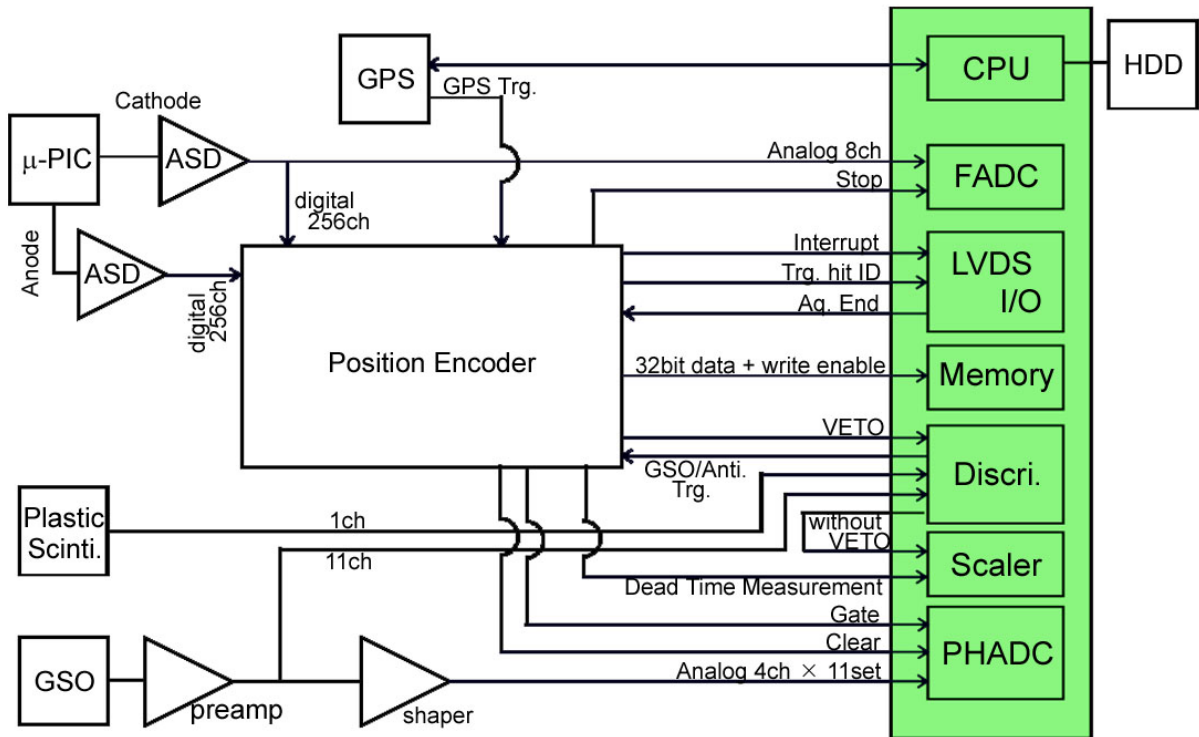


Figure 7.8: The diagram of SMILE data acquisition system

board computer on Linux, and controls all system. Both monitoring data and the event data of $N_{\text{hit}} > 3$ are acquired via VME bus, and are saved in the IDE HDDs. The system has two HDDs, and saves the same data, respectively for the redundancy.

We designed two operation modes in the DAQ system. One is the Compton Camera Mode for the gamma-ray detection. The other is the Charged Particle Tracking Mode for checking the detector performance. We change two modes by the remote operation via the CPU. The working status of the data acquisition program is monitored by another program. As the fail safe, if the acquisition program would break down at fault, the script starts up the acquisition program again automatically.

7.2.1 Compton Camera Mode

The Compton camera mode is the main data acquisition mode for the SMILE system. The detection logic is the same as that of the prototype system basically. This mode consists of three different type triggers. One is a GSO unit trigger for the gamma-ray detection. Second is a veto trigger for the rejection of charged particles. The last is a GPS trigger. For the generation of triggers, the position encoder waits during the 100 nsec after the first trigger incoming due to the time lag between the lower threshold hit and the upper threshold hit of the GSO unit.

GSO Unit Trigger

When the pulse height of the GSO signal is between the lower and upper thresholds, the discriminator generates a GSO unit trigger. The position encoder receives the GSO unit trigger, and then the encoder starts the Compton camera logic, which is similar to the prototype procedure. Figures 7.9 and 7.10 are the time charts of this mode in case of TPC signal incoming and

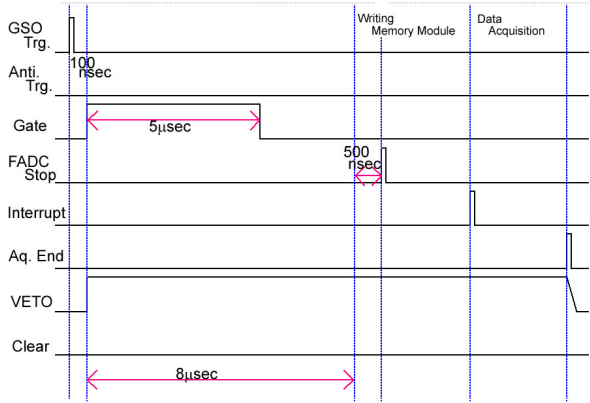


Figure 7.9: The timing chart with a GSO unit trigger and TPC signals

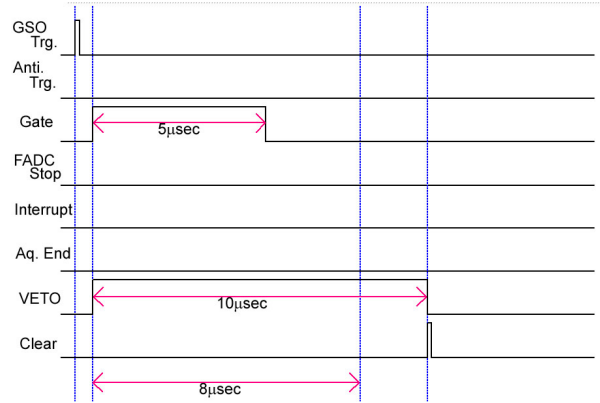


Figure 7.10: The timing chart with a GSO unit trigger and no TPC signal

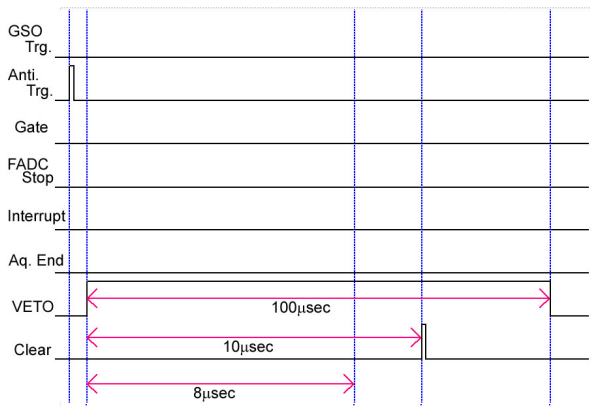


Figure 7.11: The timing chart with a veto trigger

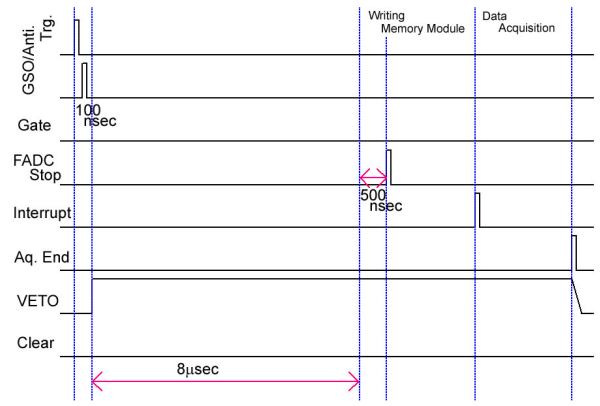


Figure 7.12: The timing chart in the charged particles tracking mode

no coming, respectively. Because the maximum of the drift length of the flight model TPC is longer than that of the prototype TPC, and the drift velocity in Xe gas is slower than Ar gas, the waiting time for TPC signals is 8 µsec.

Veto Trigger

When the pulse height of the GSO signal is larger than the upper threshold or when the signal comes from the anti-coincidence counter, the DAQ system generates the veto for the trigger, as shown in Figure 7.11.

If a veto trigger was generated, charged particles would pass through the µ-TPC, and would deposit a large energy in the GSO scintillator unit. Therefore, the system must wait for the maximum drift time (~ 8 µsec) or the recovering time of the GSO signal undershoot (~ 30 µsec). Thus, the position encoder must wait during 100 µsec after a veto trigger. Since the DAQ system requires several msec for the acquisition data, the veto system is very useful to decrease the dead time.

GPS Trigger

Our system has a GPS module to measure the balloon position and the current time. The GPS module also generates a pulse per 1 sec. We use this pulse as a trigger, in order to test the system condition. By this GPS trigger, the position encoder works as like the GSO unit trigger

and TPC signal incoming (Figure 7.12). In addition, we measure both the pedestal of the peak hold ADC and the noise level of μ -TPC in the flight.

7.2.2 Charged Particle Tracking Mode

The Charged Particle Tracking Mode is used for the check of the μ -TPC's performance at the high altitude. Figure 7.12 shows the timing chart in this mode. When the position encoder receives any two triggers of GSO unit or plastic scintillator during the 100 nsec, the procedure starts. This mode does not acquire the GSO unit data, since the purpose of this mode is the test of the μ -TPC and the GSO data are not required. We can know the triggered scintillator by the 'Trigger hit ID'.

7.2.3 Dead Time Measurement & Condition Monitoring System

To monitor the dead time, the position encoder generates '10 MHz clock' and takes 'the coincidence of VETO and 10 MHz clock'. We count the number of the coincidence by the scaler in this system, and obtain the dead time from the ratio of these counts. Also the scaler counts the hit number of each scintillator without VETO, for the check of the scintillator performance.

The system also has a DC-type ADC system for the measurements of the balloon system status. This ADC measures the voltage of the power supplies, the current of μ -TPC HV, the geomagnetic field, the tilt angles of the vessel, the pressure, and the temperatures of several points inside or outside the vessel. For the measurement of the position of the balloon and the current time, the CPU often contact to the GPS module via a serial port.

Then the CPU saves the data of the scaler, the DC-type ADC and the GPS module into two HDDs.

7.3 Flight Model μ -TPC

As a flight model TPC, we developed a TPC with the drift length of 15 cm, as shown in Figure 7.13. Since the gas volume of the flight model TPC is twice bigger than that of the prototype due to the longer drift region, the Compton probability becomes twice higher than that of the prototype even with the same gas. The gas vessel is made of a G10 frame and an Al window with the thickness of 2 mm, and μ -PIC is put on an Al flange with the thickness of 16.7 mm. A GEM is placed at the distance of 4 mm above the μ -PIC. This vessel is filled with a gas and is sealed by O-ring.

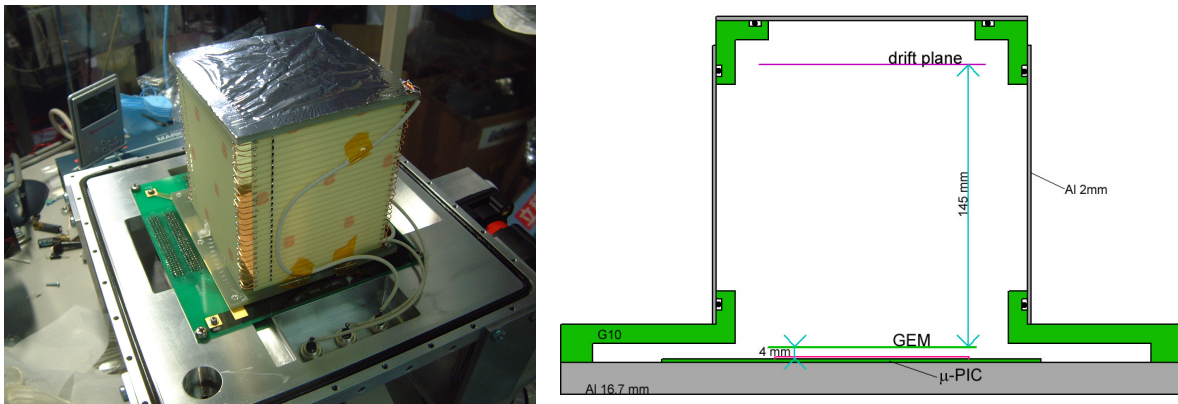


Figure 7.13: The photograph of 15 cm drift cage (left) and the schematic view of the gas vessel (right)

Table 7.3: The gas properties of the flight model μ -TPC

Parameter	value
component	Xe + Ar + C ₂ H ₆
mass ratio	80 : 18 : 2
pressure ratio	54 : 40 : 6
density	3.97 g/cm ³
Radiation length	5.4×10^3 cm
dE/dX of MIPs	5.27 keV/cm
average of Z	37.5
w value	24 eV

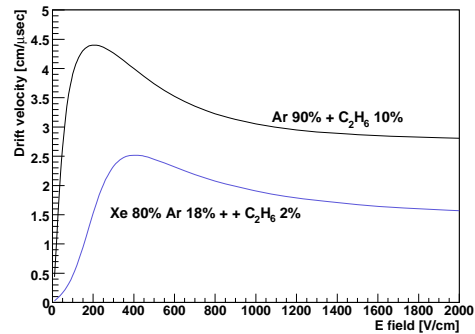


Figure 7.14: The electron drift velocity of 2 different gas

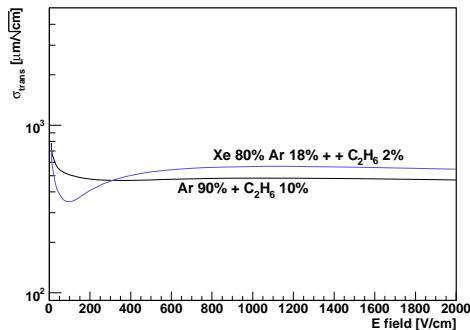


Figure 7.15: The transverse diffusion of 2 different gas

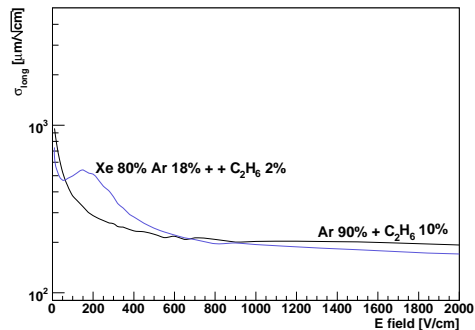


Figure 7.16: The longitudinal diffusion of 2 different gas

7.3.1 Properties of TPC Gas

In order to measure the diffuse cosmic gamma-rays, we must increase the detection efficiency of the flight model Compton camera to ten times of that of the prototype camera. Therefore, as a TPC gas, we used a Xe gas. Since Xe gas gives us a lower gas gain than Ar gas with the same voltage, a higher voltage is required for enough gain to detect MIPs tracking, and the stable operation becomes difficult. Then we mixed Xe with Ar in order to decrease the operation voltage. Also ethane gas is added as the quenching gas.

The theoretical properties of the TPC gas are listed up in Table 7.3. Expected dE/dX for MIPs in this gas is about 5.3 keV/cm, which is twice of that of Ar gas. Also the average of Z is twice of Ar. Therefore, the Compton scattering probability is about twice higher than that of Ar gas, and the flight model TPC is expected to detect the higher energy electrons than the prototype TPC. Figure 7.14 shows the electron drift velocity, and Figures 7.15 and 7.16 show the transverse and longitudinal diffusion in the TPC gas and Ar gas, respectively. With the TPC gas, the electron drift velocity is a half of the drift velocity in Ar gas, and the diffusion is nearly equal to that in Ar. Therefore the longitudinal position resolution of this gas is better than Ar gas.

7.3.2 Gain Uniformity

We operated the flight model μ -TPC with the anode voltage of 550 V for μ -PIC and the differential voltage of 400 V for the GEM. The obtained gain uniformity is shown in Figure 7.17.

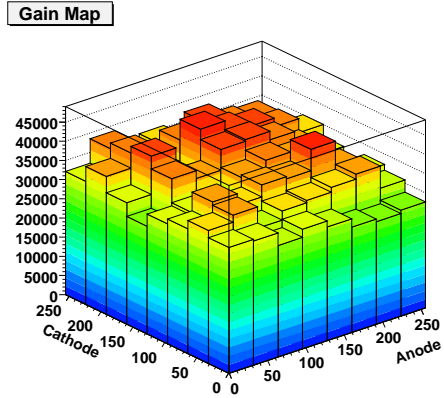


Figure 7.17: The gain uniformity of the flight model μ -TPC

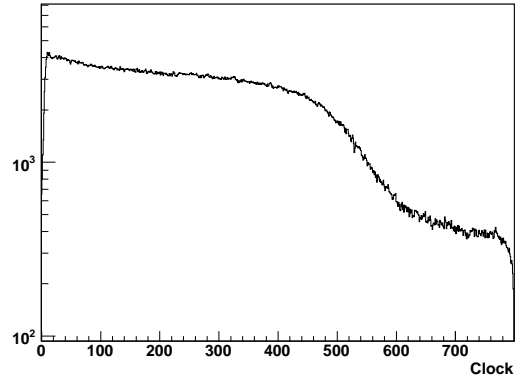


Figure 7.18: The histogram of the clock counter

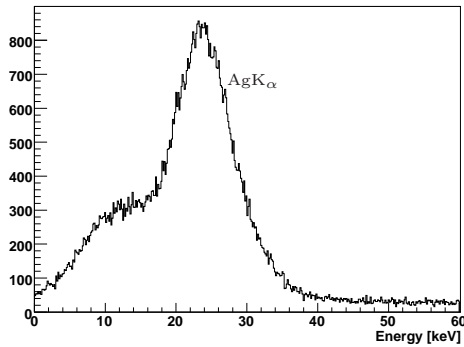


Figure 7.19: The spectrum of ^{109}Cd by the flight model TPC

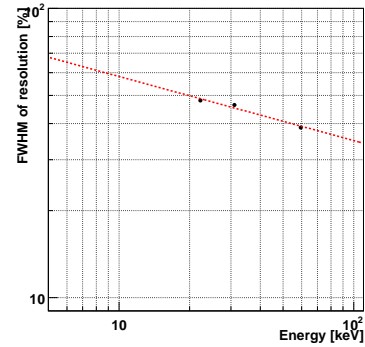


Figure 7.20: The energy resolution of the flight model TPC

The average of gas gain is about 3.5×10^4 , and the RMS of the gain uniformity is about 12 %. In comparison with the prototype TPC, the flight model TPC has a higher gas gain, but the uniformity is worse. This makes the energy resolution worse. However, the tracking efficiency is expected to be not affected because of the enough high gain.

7.3.3 Clock Counter Histogram

Figure 7.18 shows the distribution of the drift time obtained by the flight model TPC, where the drift region corresponds to the clock of 10 - 600. The length of the drift region is about 14 cm, therefore the electron drift velocity is about $2.37 \text{ cm}/\mu\text{sec}$. Because the electric field in the drift region is $380 \text{ V}/\text{cm}$, the theoretical drift velocity is $2.5 \text{ cm}/\mu\text{sec}$ from Figure 7.14. Therefore, the measured velocity is well consistent to the Figure 7.14.

7.3.4 Energy Resolution

Figure 7.19 is an obtained energy spectrum of ^{109}Cd , and Figure 7.20 shows the energy resolution. In Figure 7.20, the dashed line is obtained by fitting, and is described as follows,

$$\left. \frac{\delta E}{E} \right|_{\text{FWHM}} [\%] = 9.7 \times 10 \left(\frac{E}{\text{keV}} \right)^{-0.22}. \quad (7.9)$$

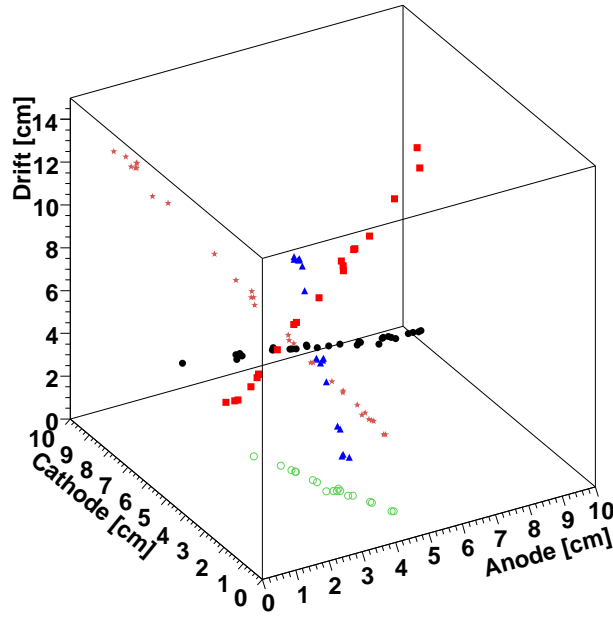


Figure 7.21: The 5 tracks by the flight model TPC

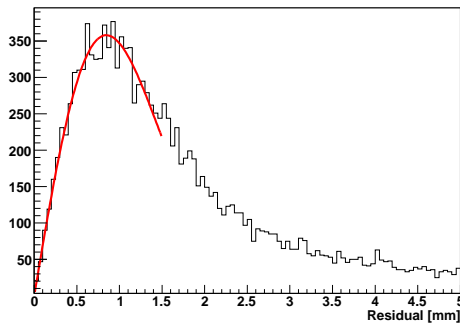


Figure 7.22: The histogram of residuals at the drift length of 6 - 7 cm

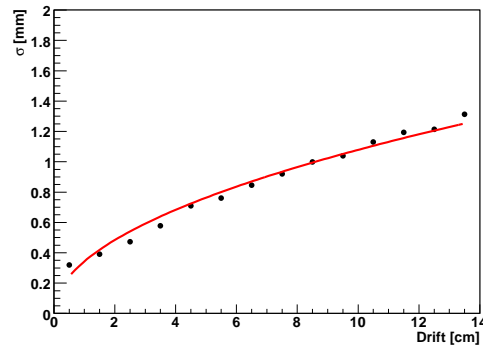


Figure 7.23: The position resolution depending on the drift length

In comparison with the prototype TPC, the energy resolution of the flight model is worse, which may be due to the non-uniformity of the gain. Another reason is that the TPC gas of the flight model is sealed, while the gas of the prototype TPC flows. Therefore, the gaseous purity of the flight model is worse than the purity of the prototype TPC, by the outer gas. Because the outer gas captures the seed electrons and the gain uniformity is not good, the flight model has the worse energy resolution than the prototype.

7.3.5 Position Resolution

With the charged particle tracking mode, we observed the cosmic muons. In Figure 7.21, several tracks of cosmic muons obtained by the ground experiment using the flight model TPC are depicted.

For the measurement of the position resolution of tracking, we obtained the residual between the hit points and track obtained by fitting. Figure 7.22 is a histogram of the residual at the drift length of 6 - 7 cm. In this figure, the solid line is obtained by fitting with a 2 dimensional

Table 7.4: The specification of flight model tracker

Gas	Xe + Ar + C ₂ H ₆ , sealed 1 atm
Volume	10 × 10 × 14.5 cm ³
Fiducial Volume	9 × 9 × 14 cm ³
Gas Gain	~ 35000
Drift Velocity	2.4 cm/μsec
Encoding Clock	100 MHz
Position Resolution	$\sigma_{\text{FM}}[\text{mm}] = \sqrt{(4.2 \times 10^{-2})^2 + (3.4 \times 10^{-1} \sqrt{z})^2}$
Energy Range	≤ 150 keV
Energy Resolution	$\text{FWHM}[\%] = 5.4 \times 10 \left(\frac{K_e}{\text{keV}}\right)^{-0.30}$

Gaussian in circular polar coordinates (5.1). Also Figure 7.23 shows the position resolution depending on the drift length. The solid line in this figure is

$$\sigma_{\text{FM}}[\text{mm}] = \sqrt{(4.2 \times 10^{-2})^2 + (3.4 \times 10^{-1} \sqrt{z})^2}. \quad (7.10)$$

7.3.6 Summary of Flight Model μ-TPC

I summarize the performance of the flight model μ-TPC in Table 7.4 based on the ground test results. In comparison with the prototype TPC, the flight model μ-TPC has a larger volume and a larger Compton scattering probability, but the energy resolution is worse than that of the prototype. However, since the first priority of the flight model developing is the improvement of the detection efficiency, this TPC has the enough performance.

7.4 Performance of Flight Model Detector

For the flight model of the MeV gamma-ray Compton camera, we constructed a bottom absorber (Figure 7.24) and 4 side absorbers (Figure 7.25). The performance of each GSO unit is similar to that of the prototype. With these GSO arrays and the flight model μ-TPC (Table 7.4), we constructed the flight model MeV gamma-ray Compton camera (Figure 7.26). In this section, the performance of the flight model detector is investigated.

Figure 7.27 shows a 3D image of a typical Compton scattering event obtained by the flight model detector. In order to check the performance of the flight model Compton camera, we measure gamma-rays using the radioactive isotopes, and also measure the background gamma-rays using no source with Compton camera mode. The spectra of ¹³⁷Cs and the background gamma-rays are shown in Figures 7.28 and 7.29, respectively. In these spectra, the peak of 662 keV from ¹³⁷Cs is clearly seen, and the spectrum of the background gamma-rays has no characteristic peak. On the other hand, When the position of the gamma-ray point source (¹³⁷Cs) changed, we obtained the images as shown in Figure 7.30. The source position are reconstructed correctly in these images.

The energy dependence of the energy resolution is shown in Figure 7.31, where the solid line, the dotted-line and the dashed-line are the energy resolution of the flight model camera, the GSO units and the μ-TPC, respectively. In the comparison with the prototype, the energy resolution of the flight model Compton camera is worse than that of the prototype camera, as mentioned previously. However, it seems that the flight model has an enough energy resolution, since diffuse cosmic and atmospheric gamma-rays have continuum spectrum.

Figure 7.32 shows the dependence of the angular resolution of ARM and SPD on the energy of the incident gamma-rays. Those looks similar to the energy dependence of the prototype's ARM and SPD. However, in comparison with the prototype, the flight model has the worse

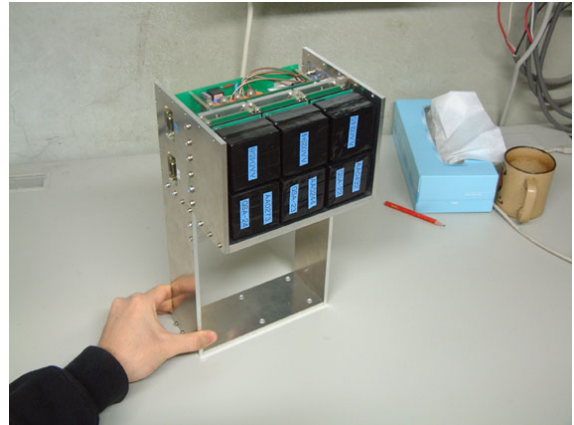


Figure 7.24: The flight model of bottom absorber

Figure 7.25: The flight model of side absorber

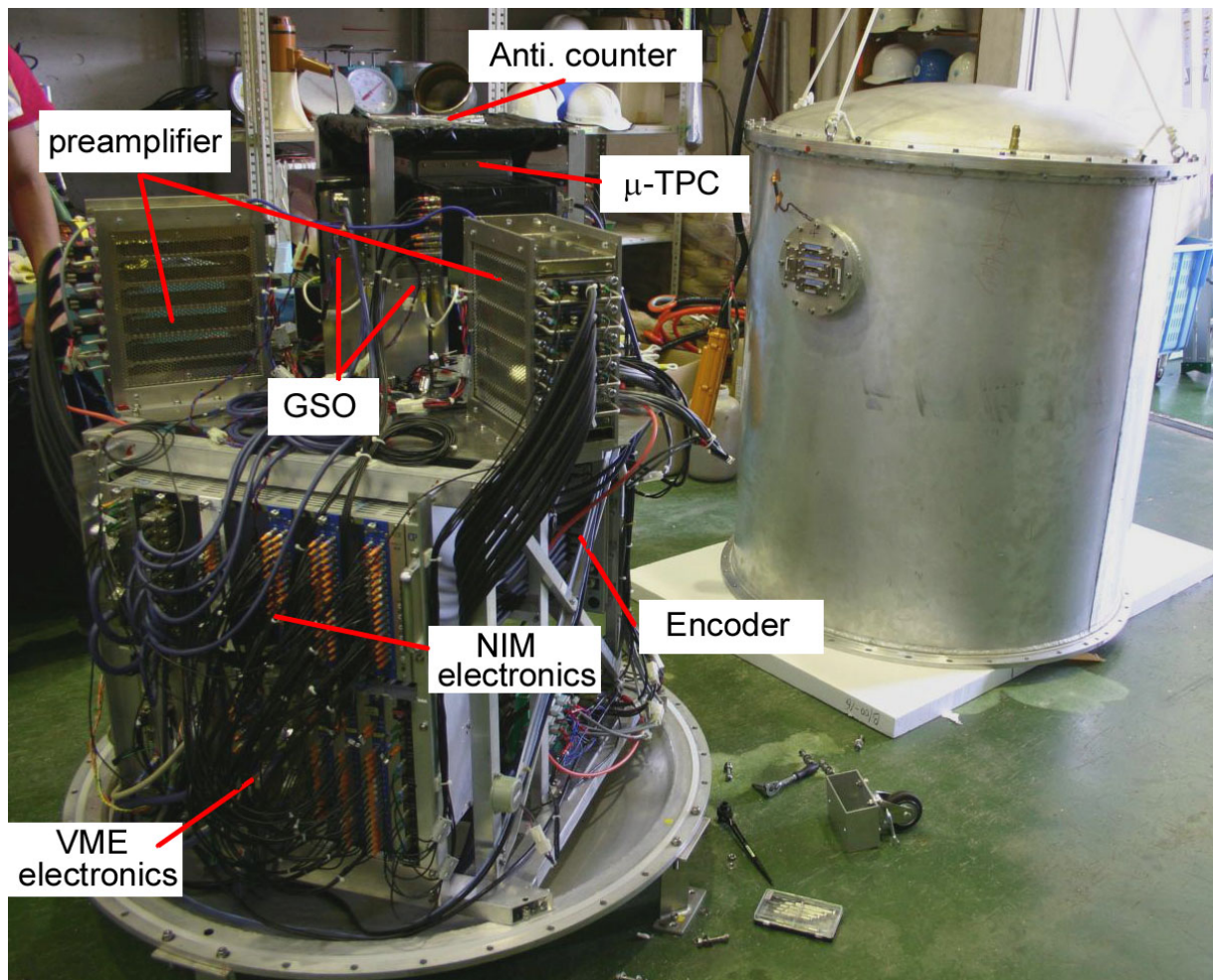


Figure 7.26: The photograph of the flight model detector and the Al vessel

20050818/per7 track_04-4908

source: ^{137}Cs 662 keV

E_0 : 639.7 keV

α_{kin} : 89.9°

E_γ : 514.7 keV

α_{geo} : 84.3°

K_e : 125.0 keV

ϕ : 36.3°

ψ : 53.6°

● : source position

★ : reconst. point

■ : absorbed point

▲ : Compton point

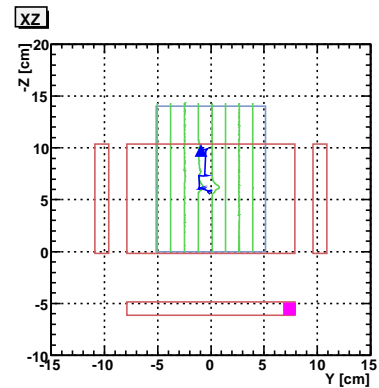
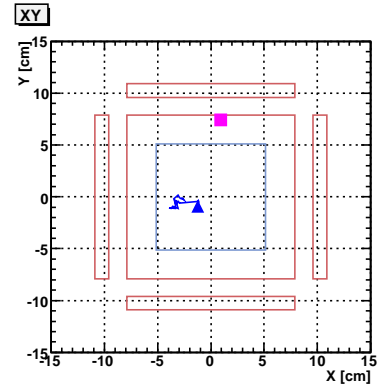
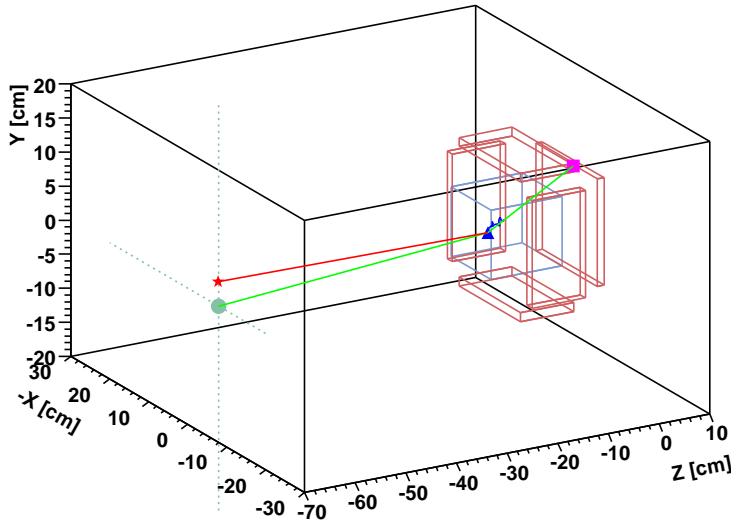


Figure 7.27: The typical gamma-ray event obtained by the flight model camera

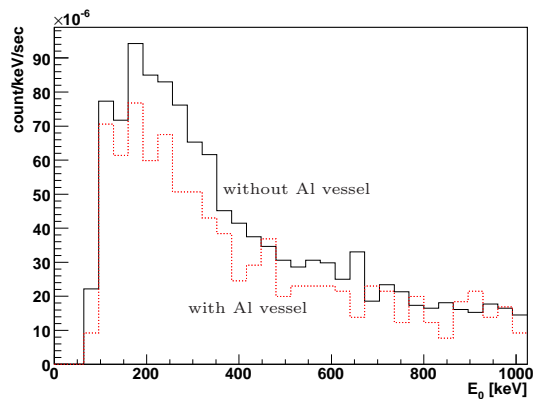
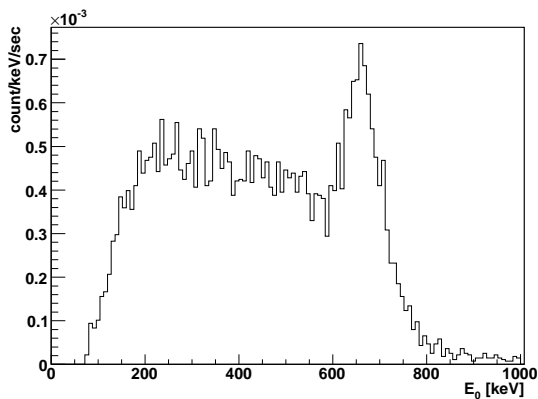


Figure 7.28: The obtained spectrum of ^{137}Cs

Figure 7.29: The obtained background spectrum

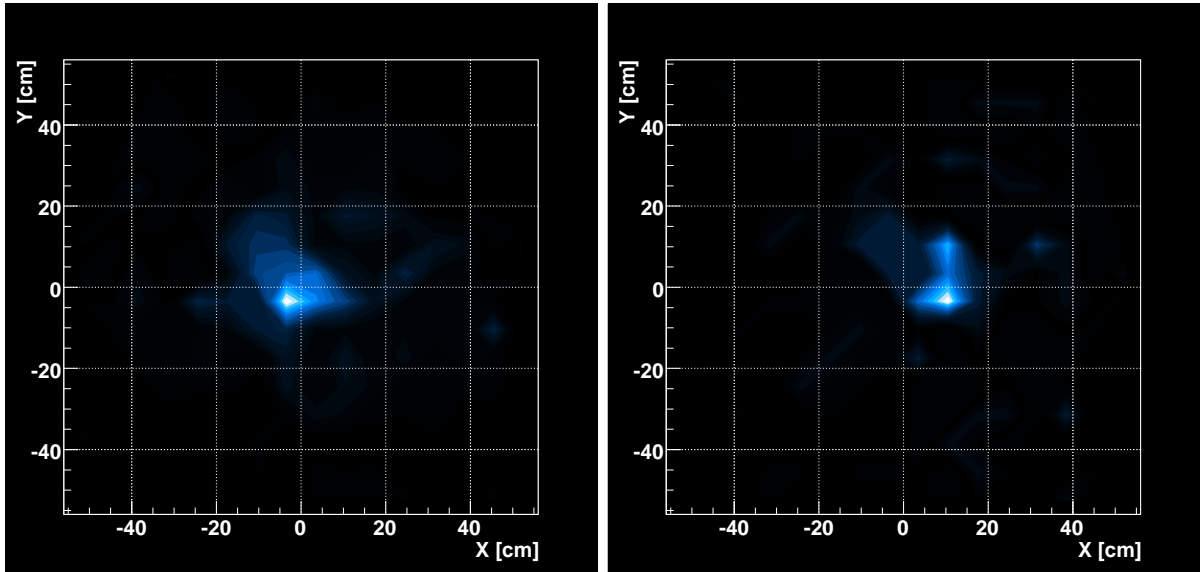


Figure 7.30: The obtained images by irradiation of gamma-rays from ^{137}Cs , which was put at the distance of ~ 50 cm from the camera window. The source position are (0cm,0cm) and (10cm,0cm), respectively. The energy range is 600 - 724 keV.

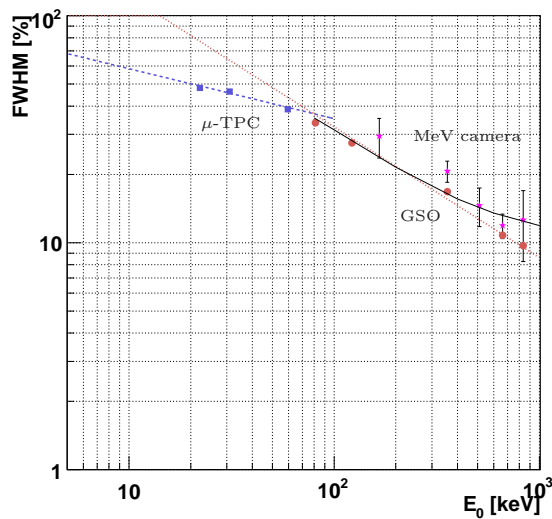


Figure 7.31: The energy resolution of the flight model camera. The dotted-line and the dashed-line are the energy resolution of the GSO units and the flight model μ -TPC, respectively. Also the solid line is that of the flight model camera expected by a calculation.

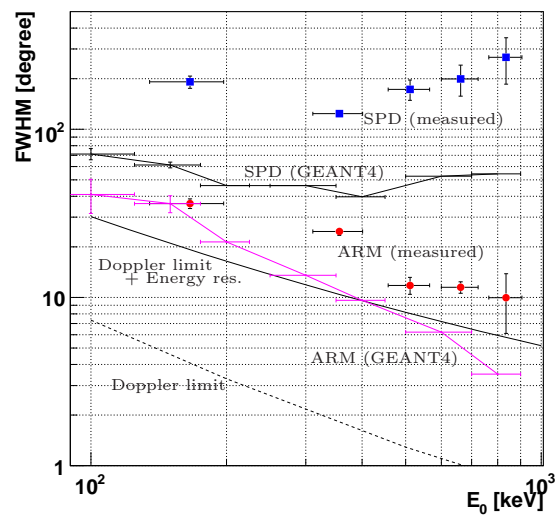


Figure 7.32: The dependence of the ARM and the SPD on the energy of the incident gamma-rays. The circles and the boxes are the FWHM of the ARM and the SPD, respectively. The data of a GEANT4 simulation does not include the electron diffusion in the TPC and the response of the preamplifier.

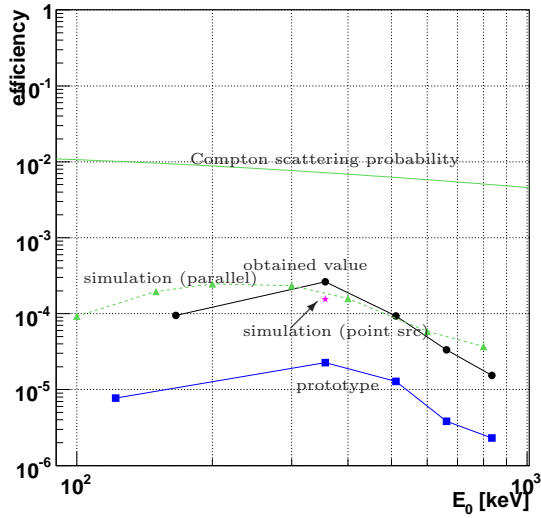


Figure 7.33: The dependence of the detection efficiency on the energy of the incident gamma-rays. The solid line and dashed line are the obtained efficiency and the simulated efficiency of the flight model, respectively. Also the box is the obtained efficiency of the prototype.

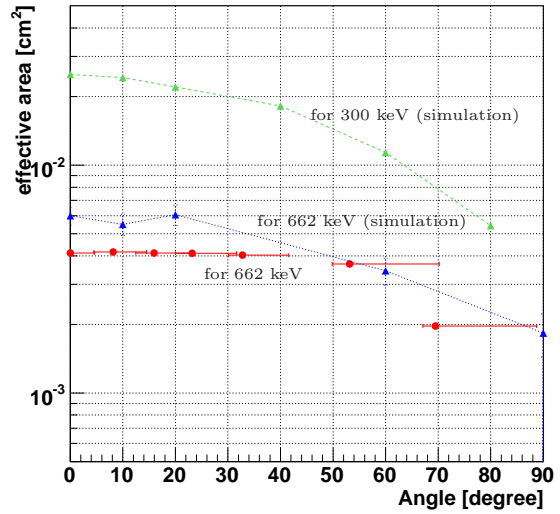


Figure 7.34: The dependence of the effective area on the zenith angle. The energy range is 600 - 724 keV. The dashed line is the simulated effective area for the gamma-rays of 300 keV and 662 keV.

angular resolution of both the ARM and the SPD. Since the purpose of this SMILE is not the measurement of the celestial point sources, we consider that the flight model has an enough angular resolution.

The detection efficiency of the on-axis source is shown in Figure 7.33, where the circles and the triangles are the experimental value and the simulation one, respectively. The detection efficiency is $\sim 10^{-4}$, which is roughly consistent with the simulated one. Also it was increased by 10 times than that of the prototype due to the improvements of μ -TPC. On the other hand, Figure 7.34 shows the variation of the effective area depending on the zenith angle. This figure says the effective area is decreased to a half at the zenith angle of $\sim 60^\circ$, thus the FOV of the flight model is about 3 str. This value is roughly consistent with that of the detector design.

Summarizing the performance of the flight model, it has a larger effective area and a larger FOV, but the angular resolution and the energy resolution are worse than those of the prototype. Because the increase of both the sensitivity and the FOV are most significant improvement in this SMILE, we consider this flight model has an enough performance.

Chapter 8

Balloon Flight

8.1 First Flight of SMILE

8.1.1 Specification of Physical Instrument

We put our detector in a $1\text{ m}\phi \times 1.4\text{ m}$ Al vessel, and the vessel was fixed at the Al gondola with the size of $1.20 \times 1.45 \times 1.55\text{ m}^3$, as shown in Figure 8.1. At both sides of the gondola, the batteries and the ballast boxes were attached, and the gondola was packed with the expanded polystyrene. The specifications of the first SMILE balloon are listed in Table 8.1. The total weight is 816 kg: the balloon 263 kg, the gondola 397 kg, the ballast 130 kg, and the other applications (parachute, cutter and radio-buoy) 26 kg. The total power consumption is about 350 W, where the power in the vessel is $\sim 250\text{ W}$ and the conversion loss is $\sim 100\text{ W}$. The SMILE gondola has two clinometers and two geomagnetic aspectmeters for the posture measurement of the gondola. Also there is a fine pressure gauge outside the gondola, a general pressure gauge inside the vessel and a differential pressure gauge inside the TPC vessel. Also 23 temperature sensors are set inside and outside the vessel, where 12 sensors inside of the Al vessel and 11 sensors outside. To reach a ceiling altitude of 35 km, we used a balloon with the volume of 10^5 m^3 (B100, Fujikura Kousou). By a B100, the pressure at the expected altitude is

$$850 \times \frac{819[\text{kg}]}{10^5[\text{m}^3]} = 7.0[\text{hPa}]. \quad (8.1)$$

Therefore, the expected altitude is about 34.1 km.

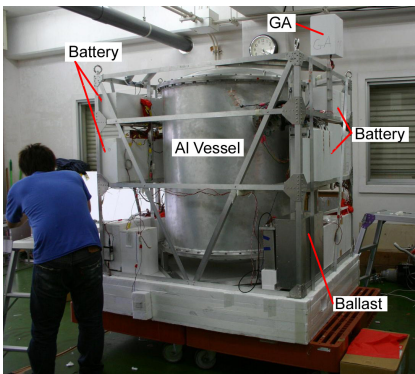


Figure 8.1: The photograph of gondola before the packing

Table 8.1: The specifications of the 1st SMILE balloon

Balloon	Fujikura Kousou B100 (10^5 m^3)
Gondola Size	$120 \times 145 \times 155\text{ cm}^3$
Weight	816 kg
Balloon	263 kg
P. I.	397 kg
Ballast	130 kg
Power	$\sim 350\text{ W}$
Command	double tone 15 ch
Telemetry	Bi-phase 64 kbps

Table 8.2: The table of the commands for the SMILE data acquisition system. The blank column means ‘Clear SELECT’.

#MENU	Telemetry Test	#SELECT								
		0	1	2	3	4	5	6	7	
0	Monitor data	Event data	Scaler data	GPS data						
1	Setting	Clear MENU	HV default	HV off	Discr. default	Discr. max	Discr. min			
2	Mode	Clear MENU	Compton	tracking		Shutdown				
3	Reset	Clear MENU	Encoder	GPS	fan on	fan off				
4	GSO discr.	Clear MENU	50 mV	0 mV	15 mV	30 mV	70 mV	100 mV	100 mV	1 V
5	Anti. discr.	Clear MENU	50 mV	0 mV	25 mV	100 mV	400 mV	400 mV	1 V	
6	Upper discr.	Clear MENU	1 V	0 mV	200 mV	400 mV	600 mV	600 mV	2.5 V	
7	Anode th.	Clear MENU	-35.0 mV	0 mV	-32.5 mV	-37.5 mV	-40.0 mV	-40.0 mV	-50.0 mV	
8	Cathode th.	Clear MENU	35.0 mV	0 mV	32.5 mV	37.5 mV	40.0 mV	40.0 mV	50.0 mV	
9	Anode V	Clear MENU	550 V	0 V	540 V	545 V	555 V	555 V	560 V	
10	Drift V	Clear MENU	-6.2 kV	0 V	-5.6 kV	-5.8 kV	-6.0 kV	-6.0 kV	-6.4 kV	
11	Bottom HV	Clear MENU	Default	0 V	def. -10 V	def. -30 V	def. -50 V	def. -50 V	def. -100 V	
12	Side 1 HV	Clear MENU	Default	0 V	def. -10 V	def. -30 V	def. -50 V	def. -50 V	def. -100 V	
13	Side 2 HV	Clear MENU	Default	0 V	def. -10 V	def. -30 V	def. -50 V	def. -50 V	def. -100 V	
14	Anti. HV	Clear MENU	-1.05 kV	0 V	-0.90 kV	-0.95 kV	-1.00 kV	-1.00 kV	-1.10 kV	

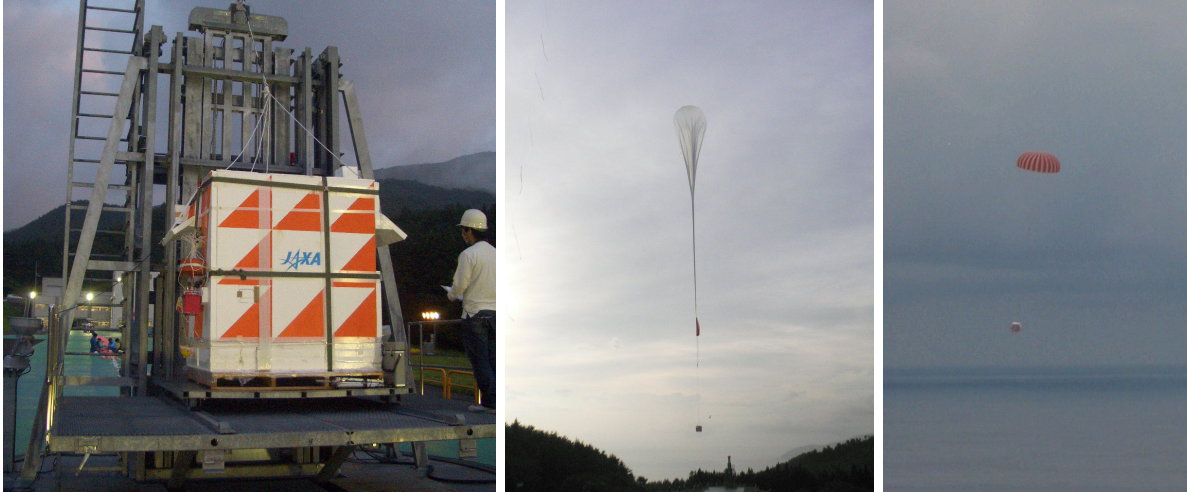


Figure 8.2: The left is photograph of final style of gondola on a launcher. The SMILE balloon was launched from Sanriku Balloon Center at 06:11 on 1 September, 2006 (center). And we recovered the detector at 14:32 (right).

For the remote control, we use 15 telecommands using a relay switch. Six commands are for the balloon control: 2 for the cutter, 1 for the ballast control, 1 for the exhaust control and 2 for the balloon control system. The other 9 commands are for the SMILE system: 2 for the standby-on/off, 4 for the power-on/off and 3 for the control of the SMILE data acquisition system. The 3 commands for the control of the SMILE data acquisition system were named MENU, SELECT and SET. The CPU counts the received MENU/SELECT signal. When the CPU receives SET, the SMILE system carries out the command of the MENU/SELECT number in Table 8.2.

All of the acquired data are saved into two local hard disk drives. However, since the local disks may not be recovered after the experiment, we must transfer a part of the data to the ground station. For the data transfer, we used the pulse-code modulation telemetry in 64 kbps. The SMILE system sends the 384 byte HK/GPS data at every 1 sec, and sends the 320 byte scaler data at every 10 sec. Also the system sends the 384 byte event data during the remainder. Therefore, the maximum rate of the event data transfer is ~ 20 Hz.

8.1.2 Flight Path and Operation Mode

The first SMILE balloon was launched from Sanriku Balloon Center (39.16N, 141.82E) on 1st September, 2006 (JST). The event sequence in the flight is listed up in Table 8.3. We turned on the power of the system at 05:26, and began to operate the SMILE system in the Compton camera mode (the left of Figure 8.2). The balloon was launched at 06:11 (the center of Figure 8.2). At 08:56, the balloon reached to the altitude of 35 km, and started the level flight. We changed the operation mode to the charged particle tracking mode at 12:06, and the mode returned to the Compton camera mode at 12:34. Then we turned off the power of system at 12:59. Finally we cut the gondola from the balloon at 13:20. The gondola landed on the sea at 13:45, and we recovered the gondola at 14:32 on the sea (the right of Figure 8.2).

Figure 8.3 shows the path of the first SMILE flight. Also, the time variation of the flight altitude of the balloon is shown in Figure 8.4, and that of the pressure of the atmosphere in the level flight is shown in Figure 8.5. In the level flight from 08:56 to 10:15, the altitude was constant 35.0 km and the atmosphere pressure is 5.4 hPa (5.5 g/cm²). From 11:20 to 13:00, the altitude is 32 km and the pressure is 8.5 hPa (8.7 g/cm²).

Table 8.3: The sequence of events in the flight

Time in JST	Event
05:26	turn on (Compton camera)
06:11	launch
08:56	reach to the level flight
12:06	tracking mode
12:34	Compton camera mode
12:59	turn off
13:20	cut from the balloon
13:45	landing
14:32	recovering



Figure 8.3: The path of the SMILE flight

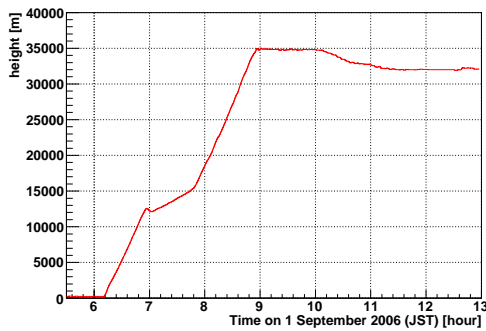


Figure 8.4: The altitude of the gondola

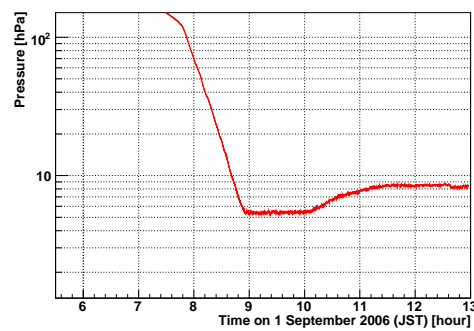


Figure 8.5: The atmosphere pressure

8.2 Status of Detector in Balloon Flight

8.2.1 House Keeping Data

Figure 8.6 shows the time variations of the pressure of the TPC gas and the pressure inside the Al vessel. This figure says that the air tightness of the Al vessel was kept during the flight. Also the TPC gas pressure was increased gradually, and the pressure increased at the end of the experiment was 4.5 %. The increase of the TPC gas pressure was too slight to make little change of the gas gain of the μ -TPC.

On the other hand, Figure 8.7 shows the temperatures of the various points. From this figure, we inferred that the increase of the TPC gas pressure might be caused by the gas temperature increase. The hottest point in the Al vessel is the CPU, but the temperature of the CPU was kept under 60 °C. At the outside of the Al vessel, the hottest point was the battery supplying the most intense current, which is Battery 1 in Figure 8.7. However, because the battery works at the temperature of -20 - 90 °C, its temperature was no problem in the flight.

8.2.2 Count Rate of Scintillators

The count rates of all scintillators without the veto are shown in Figure 8.8. A, B and C of GSO units are the bottom camera. C, D, E and F are the lower line of the side camera, and H, J, K and L are the upper line of the side camera. These count rates decreased just after the launch of the balloon, because the radiation from the earth decreases as the altitude increases. The count rate has a maximum rate (the Pfozter Maximum) at about 08:00, where the altitude was the point of the air shower maximum, about 18 km. In the level flight, the count rate was about the half of the maximum rate, and looked constant.

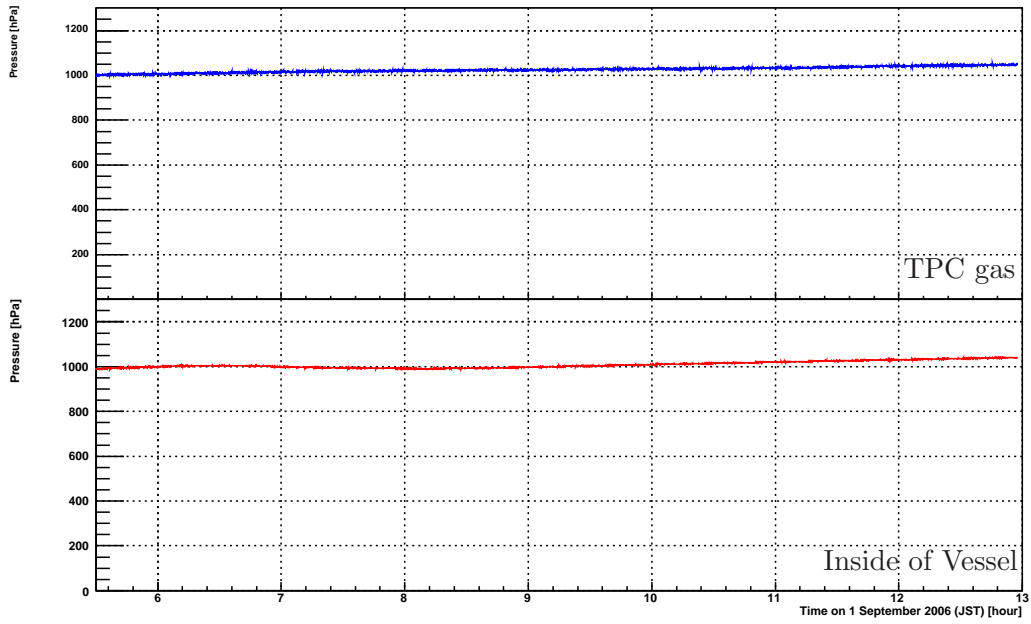


Figure 8.6: The pressure of TPC gas (upper) and the pressure of the inside of Al vessel (lower) in the flight

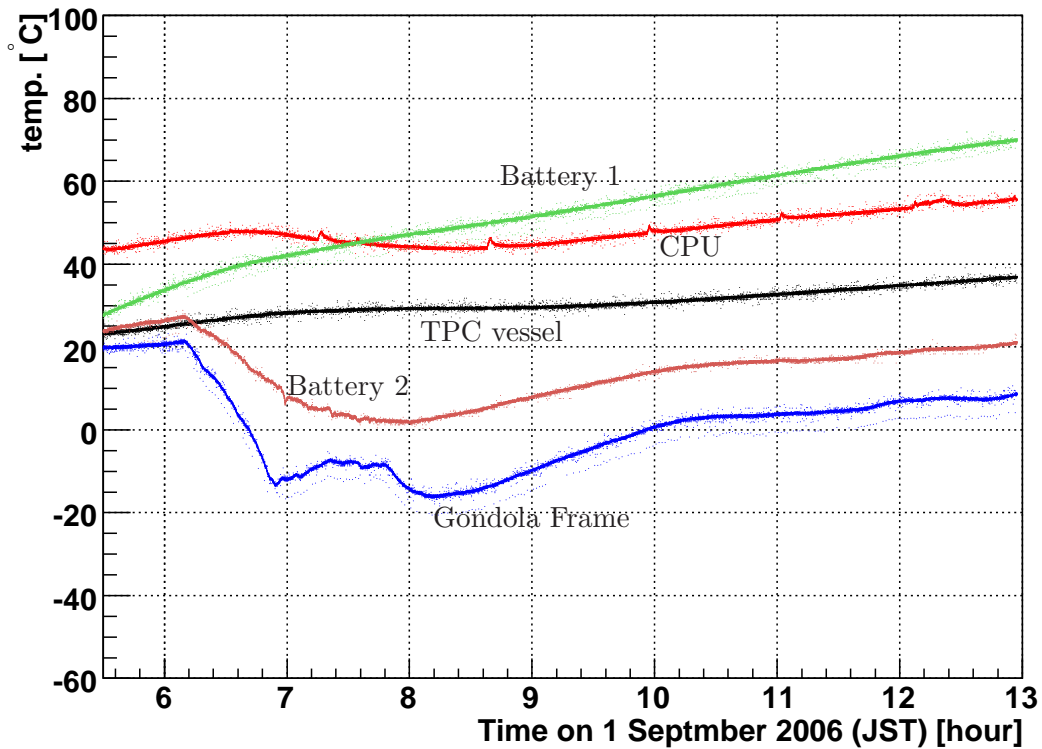


Figure 8.7: The temperatures at the various points

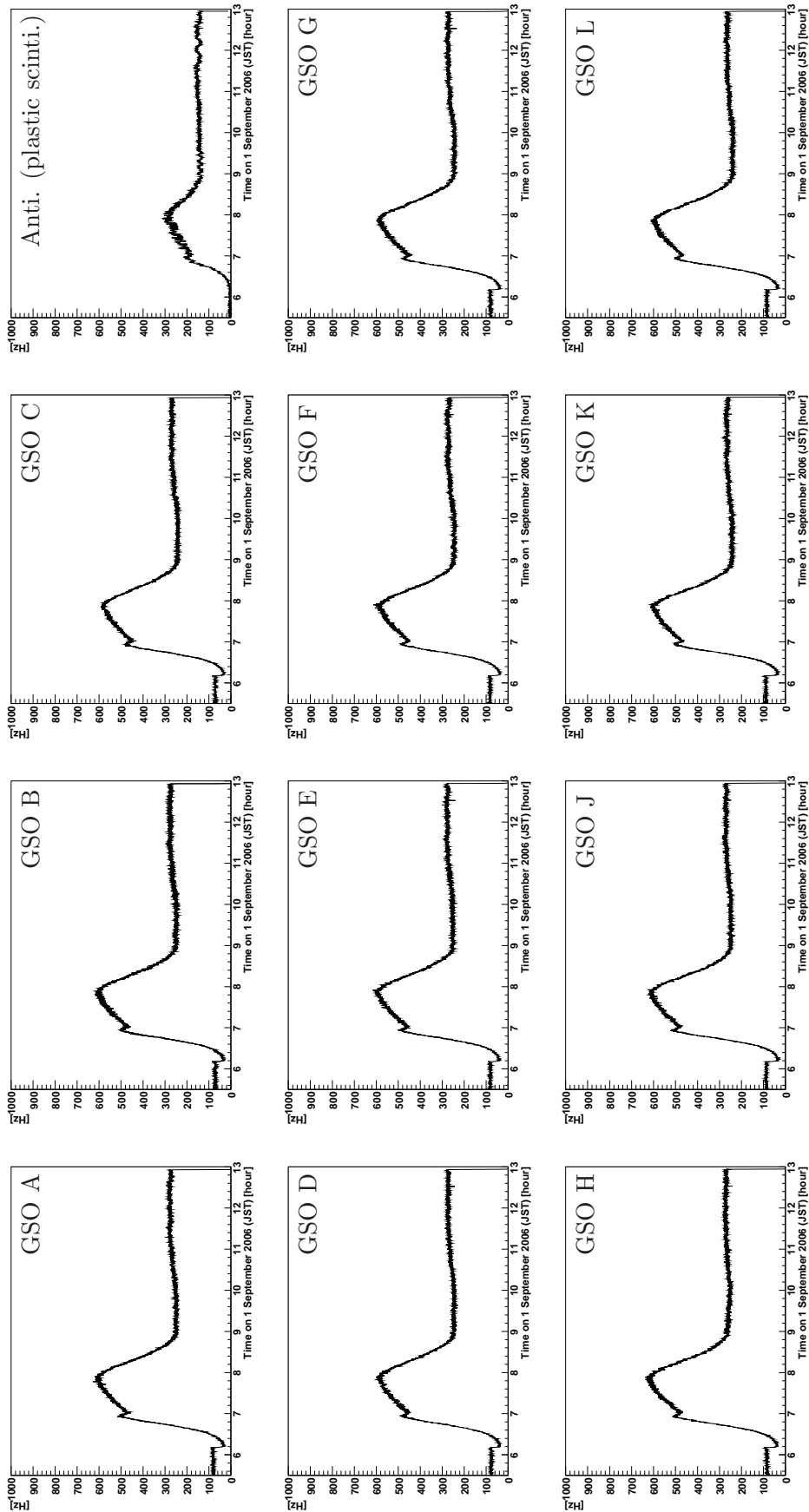


Figure 8.8: The count rate of all GSO units and the plastic scintillator. A, B and C of GSO unit are the bottom camera. D, E, F and G are the lower line of the side camera. H, J, K and L are the upper line.

8.2.3 Current of μ -TPC

The time variation of the current of the μ -PIC anode is shown in Figure 8.9. From this figure, it is noted that there occurred several small discharges in the flight. It means that the pixels of the μ -PIC were not broken for those several discharges. Figure 8.10 shows the discharge rate per 30 minutes during the flight. The discharge rate increased after the launch of the balloon. After the Pfofzer Maximum, the discharge rate looked constant, although the count rate of the GSO units at the level flight decreased in a half of that at the Pfofzer Maximum. Thus we consider these discharges were caused by the primary heavy cosmic-rays, such as a He or C ions.

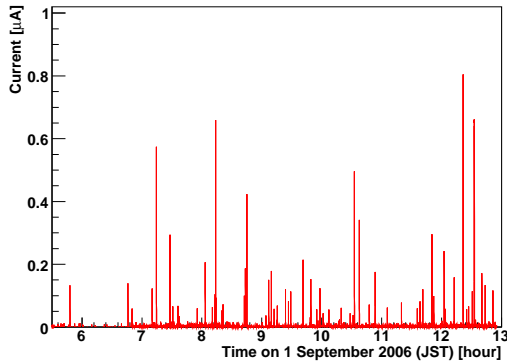


Figure 8.9: The current of μ -PIC anode in the flight

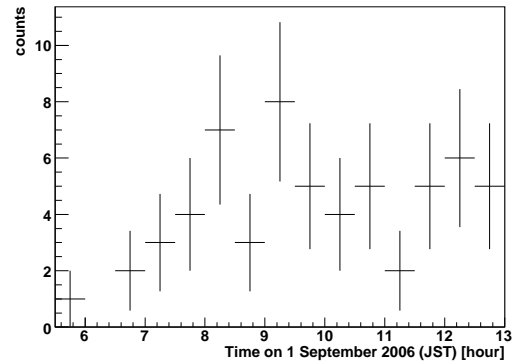


Figure 8.10: The discharge number of μ -PIC per 30 minutes

8.2.4 Dead Time & Event Rate

Figure 8.11 shows the ratio of the dead time to the real time. The ratio was 5 % on the ground. The dead time was increased to 30 % at the Pfofzer Maximum, and 20 % in the level flight with the Compton camera mode. During the charged particle tracking mode (12:06 - 12:34), the dead time was about 30 %. Sometimes, the ratio was increased to ~ 100 %. That was due to a system bug, which the position encoder loses the acquisition end signal, and then the automatically fail safe reseted the acquisition cycle. In the calibration run on the ground, such an error did not happen so often. We must fix the bug for the future balloon experiments. The

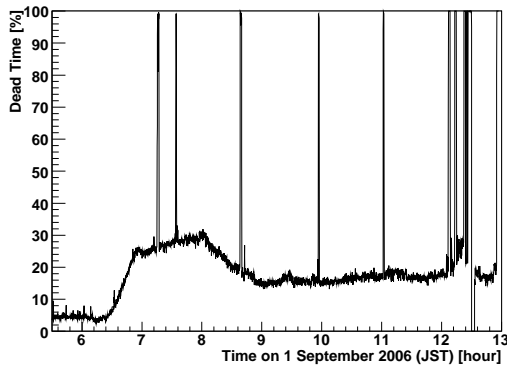


Figure 8.11: The dead time ratio to the real time

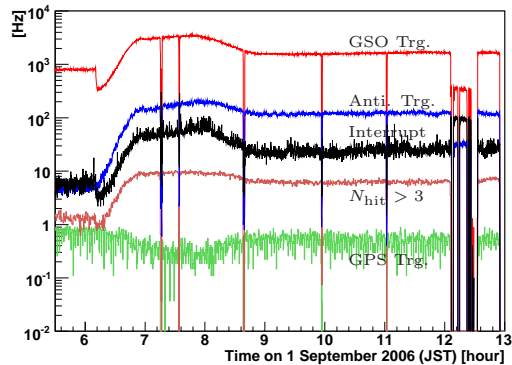


Figure 8.12: The time variation of the various flags

per1 track_00-1523
Fri Sep 1 12:08:40 2006

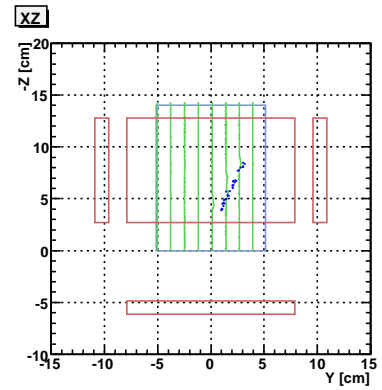
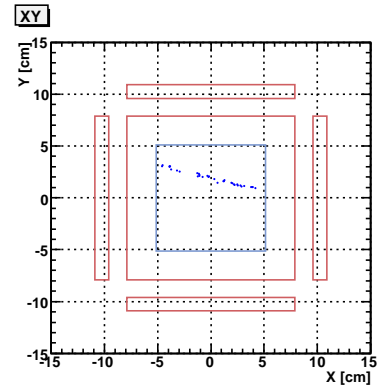
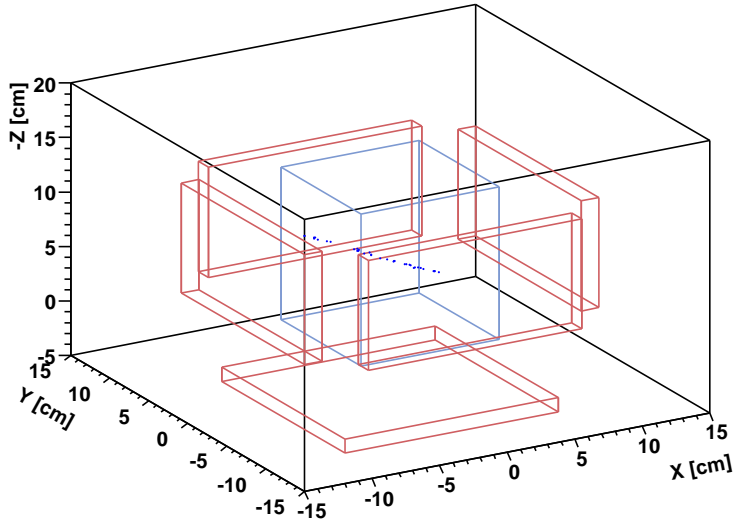


Figure 8.13: The single track obtained in the Charged particle tracking mode

per1 track_00-1203
Fri Sep 1 12:06:29 2006

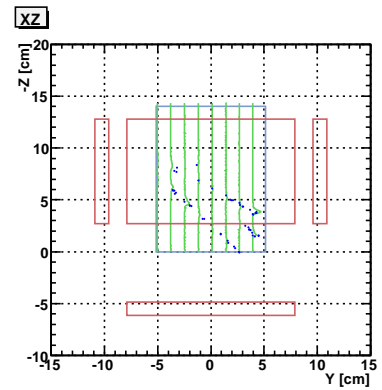
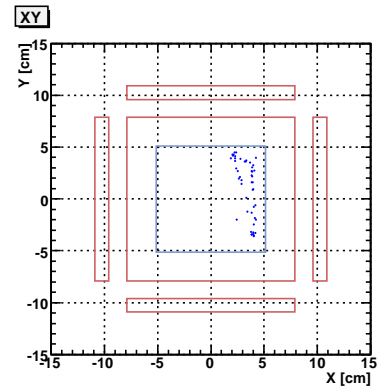
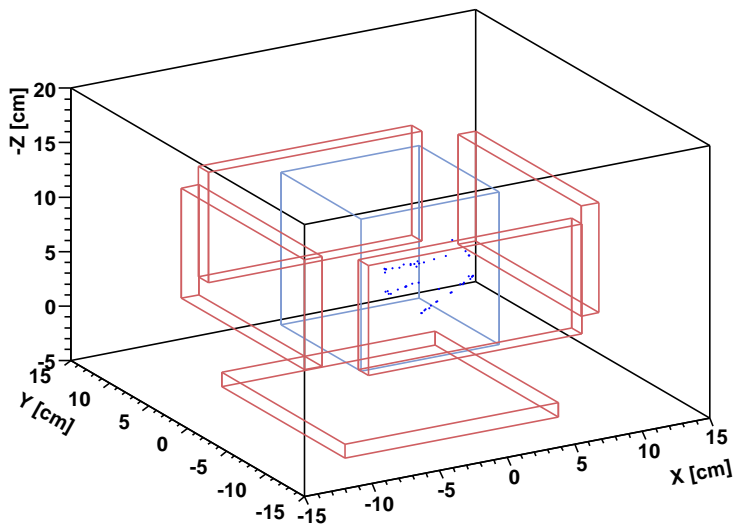


Figure 8.14: The multi track obtained in the Charged particle tracking mode

rates of the several DAQ flag are shown in Figure 8.12, where ‘GSO Trg.’ the rate of all GSO trigger received by the position encoder, ‘Anti. Trg.’ the plastic scintillator trigger rate received by the encoder, ‘Interrupt’ is the rate of the coincidence of the μ -TPC and GSO, ‘ $N_{\text{hit}} > 3$ ’ is the data acquisition rate by GSO trigger, and ‘GPS Trg.’ is the data acquisition rate by the GPS trigger. At the Pfozter Maximum, the coincidence rate was ~ 60 Hz, and the data acquisition rate ($N_{\text{hit}} > 3$) was ~ 10 Hz. During the level flight, the coincidence rate was ~ 25 Hz, and the data acquisition rate was ~ 6 Hz. The GPS trigger rate had a negative correlation with the dead time, and it was ~ 0.7 Hz on the ground, ~ 0.3 Hz at the Pfozter Maximum and ~ 0.5 Hz during the level flight.

8.3 Results of Experiment & Discussion

We analyzed the data obtained in the flight, and summarize the results in this section.

8.3.1 Charged Particle Tracking Mode

The examples of the obtained tracks in the charged particle tracking mode are shown in Figures 8.13 and 8.14. Especially, Figure 8.14 shows the multi-tracks of the ‘shower event’ from GSO. Figure 8.15 shows the relation of the energy and the track length of all events obtained in the charged particle tracking mode. The solid line and the dashed line in this figure are calculated dE/dX of MIPs and the stopping electrons, respectively. For the gamma-ray reconstruction, we select the fully contained electron events under the criteria such as

$$\left| \frac{L_e}{\text{cm}} - 1.8 \times 10^{-3} \left(\frac{K_e}{\text{keV}} \right)^{1.8} \right| \leq 2, \quad K_e > 15[\text{keV}]. \quad (8.2)$$

Figure 8.15 says that fully contained electron cut rejected 95 % of the events acquired in the charged particle tracing mode. Therefore, only using this selection, ~ 5 % of charged particle events might include to the gamma-ray events.

In order to obtain the dE/dX spectrum of the single track in the flight, we fitted the tracks with a straight line under the position resolution (7.10), and then the resultant χ^2 histogram is Figure 8.16. We selected the events of $\chi^2 < 1$ as a single track event for which we obtained the dE/dX spectrum as shown in Figure 8.17. In this figure, the solid line is obtained by fitting with a Lorentzian having a peak at 5.4 keV/cm. Since the calculated dE/dX is about 5.3 keV/cm, the obtained value is consistent to the calculated one.

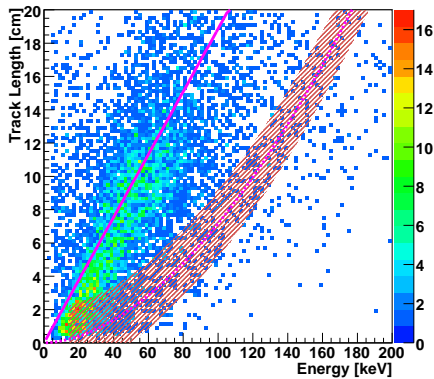


Figure 8.15: The relation of the track energy and the track length in the charged particle tracking mode.

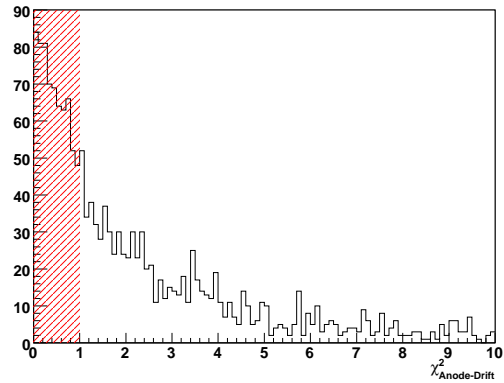
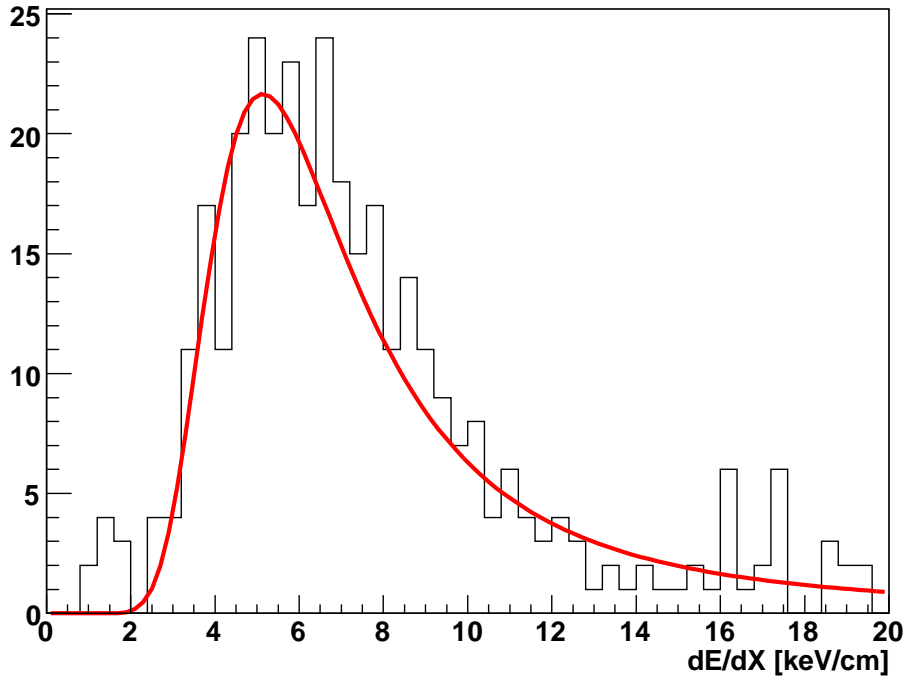


Figure 8.16: The χ^2 histogram of fitting the tracks with a straight line.

Figure 8.17: The dE/dX spectrum in the level flight

8.3.2 Compton Camera Mode

Figure 8.18 shows the typical Compton scattering event obtained during the balloon flight. In order to collect such Compton events, we analyzed this flight data using the same criteria used in the ground calibration, as described in section 7.4. The sum spectra of μ -TPC and GSO at each event selection are shown in Figure 8.19. In the Compton camera mode, 2.23×10^5 events were acquired during 7.0 hours, in which the single GSO trigger events were 1.09×10^5 events. Figure 8.20 shows the relation of the energy and the length of the obtained tracks in the Compton camera mode. The solid line and the dashed line are the dE/dX of the MIPs and the stopping electron in this TPC, respectively. The difference from Figure 8.15 is the existence of many events along the dashed line. The fully contained electron events (8.2) were 6.46×10^3 events. After the Compton scattering kinematic fit (6.3), 1.02×10^3 events remained. Then 427 events were inside the FOV. Finally, 199 events were inside the FOV during the level flight of 3.0 hours live time. On the other hand, the ratio of the single GSO trigger events to the all acquired events is about 50 % in this experiment, and the reduction efficiency of charged particle by the selection of the fully contained electron is 95 % as seen in section 8.3.1. Also the reduction efficiency by the selection using the Compton scattering kinematics is > 99 %, which was obtained by simulation. Thus, the wrong-rejection probability of charged particle is about 3×10^{-4} for the gamma-ray reconstruction. Even if all of the acquired data in the level flight were the charged particle events, the remained number of the particle events was < 20 after the kinematical cut. Thus, the systematic error by charged particle was < 4 %. Also there are the ‘not-Compton’ events, which include the events of scattering in the GSO at first or the events of absorption in the GSO and absorption of irradiation GdK_α in μ -TPC. A GEANT4 simulation says that the systematic error due to such pseudo events is ~ 20 % for 150 keV and ~ 40 % for 600 keV.

In the level flight, the energy spectrum of 199 downward gamma-rays, of which the direction

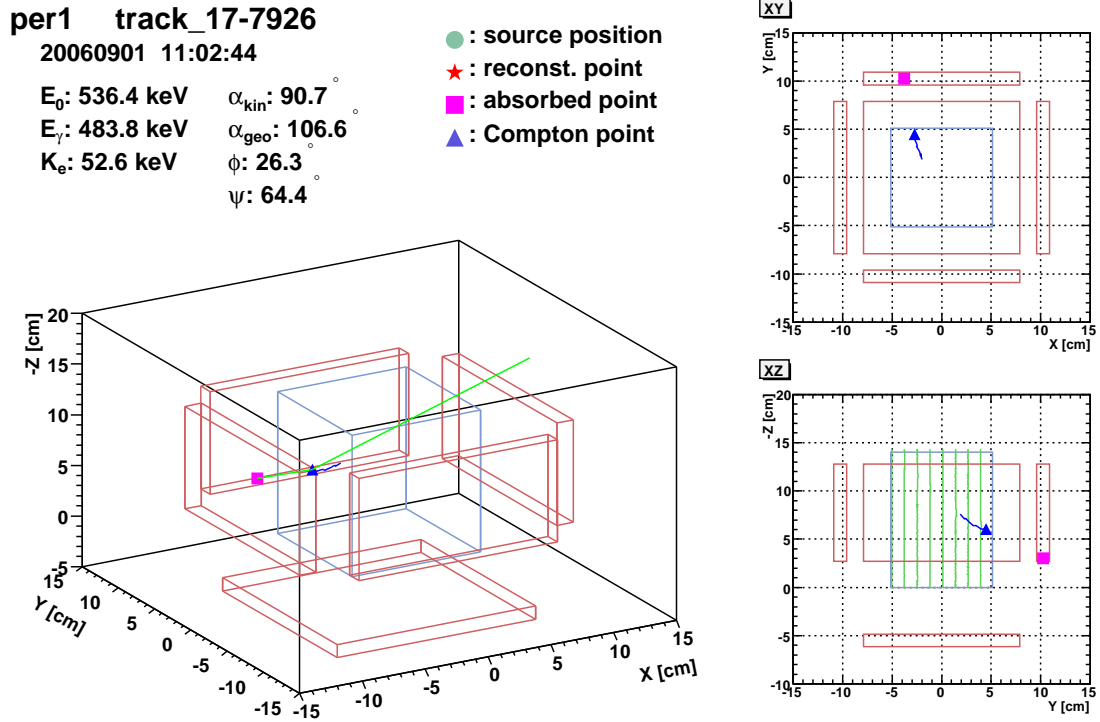
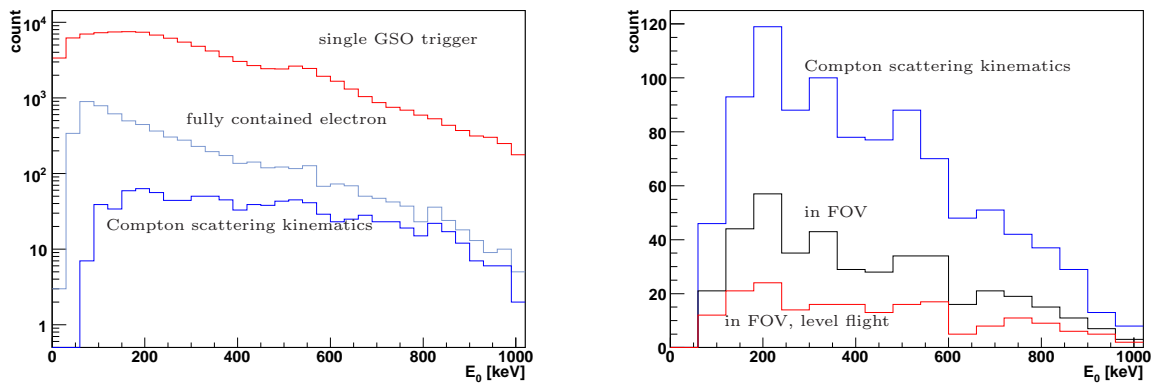


Figure 8.18: The event view of the Compton event in the flight

are inside the FOV (zenith angle $< 60^\circ$), is shown in Figure 8.21. Since we expected to detect ~ 200 photons inside the FOV during 3 hours at the altitude of 35 km by GEANT4 simulation (Table 7.2), the experimental result, of which 199 photons were obtained during the live time of 3.0 hours at the altitude of 32 - 35 km, was well consistent. Also this spectrum has a slightly excess at near 511 keV, which is seen in the simulation as shown in Figure 7.5. The photon number of this excess is ~ 10 . Therefore, it is roughly explained with 511 keV gamma-rays produced by the charged particles, because our simulation says about 10 photons are produced by such cosmic-rays at the altitude of 35 km (Table 7.2).

The time variation of the gamma-ray events is shown in Figure 8.22, which has a maximum countrate near the Pfozter Maximum, and thereafter it is roughly constant during the level flight, which is similar to the time variation of the hit of the GSO units.


 Figure 8.19: The spectra summed of μ -TPC and GSO at each event selection

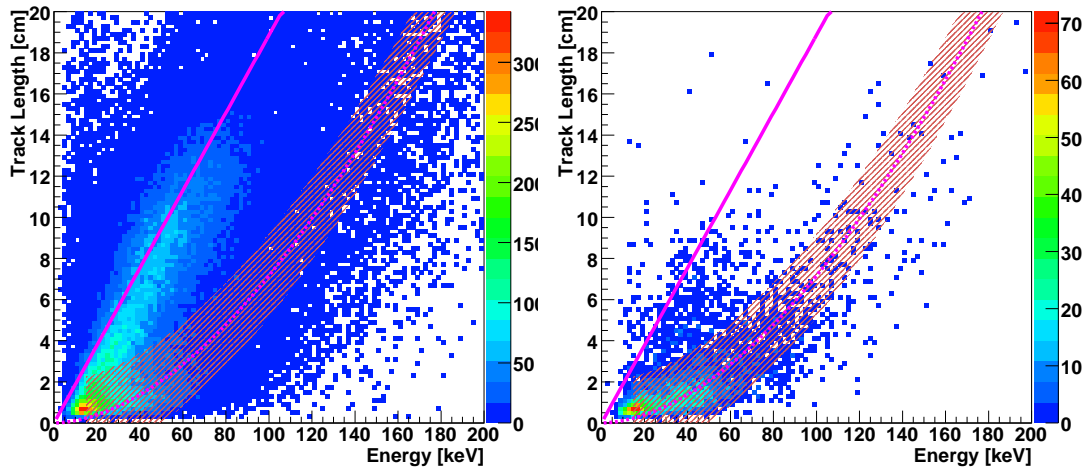


Figure 8.20: The relation of the energy and the length of the obtained tracks in Compton camera mode. The left figure is the relation of all events and the right one is that of the fully contained events in $7 \times 7 \times 7 \text{ cm}^3$. The solid line and the dashed line are the dE/dX of the MIPs and the stopping electrons, respectively.

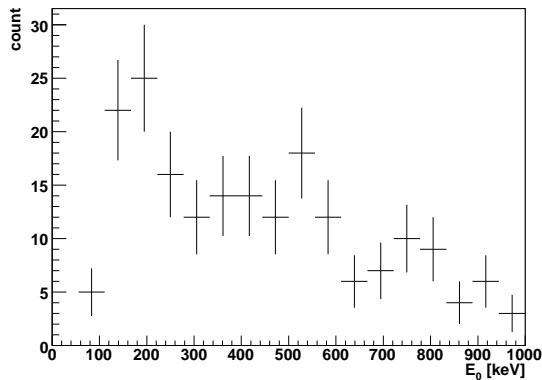


Figure 8.21: The spectrum of the downward gamma-rays during the level flight (after 09 : 00). The error bar is the statistical sigma.

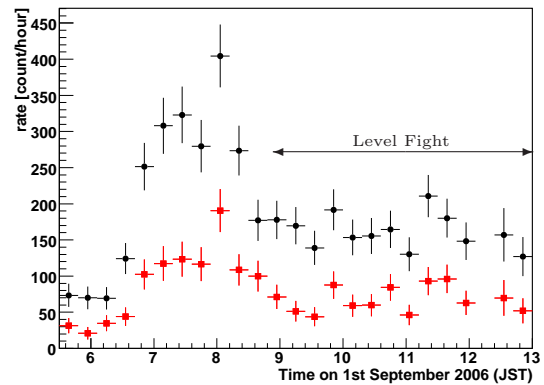


Figure 8.22: The time variation of the detected gamma-rays. The circles and the boxes are all direction and the downward gamma-rays count rate, respectively. The error bar is the statistical sigma.

Table 8.4: The number of the detected downward gamma-rays from 100 keV to 900 keV

Time (JST)	Pressure [hPa]	120 - 300 keV	300 - 900 keV	Real Time [hour]
8 : 00 - 8 : 12	54.6	15	16	0.144
8 : 12 - 8 : 24	31.8	7	9	0.152
8 : 24 - 8 : 48	13.8	10	20	0.324
8 : 54 - 10 : 06	5.42	17	41	1.11
10 : 06 - 11 : 00	6.69	16	32	0.752
11 : 00 - 11 : 30	8.13	9	17	0.411
11 : 30 - 12 : 55	8.46	17	27	0.767

Using the obtained effective area by a ground calibration (Figure 7.34), we calculated the flux of the incident gamma-rays. Figure 8.23 shows the dependence of the gamma-rays flux on the zenith angle at the level flight. With the events in all azimuth angle, we obtained the gamma-ray flux printed by circles in Figure 8.23. In this figure, the solid line is the calculated gamma-ray flux at 300 keV in the atmospheric depth of 7.0 g/cm² [50]. The obtained flux inside the FOV looks consistent with the calculation. However, the obtained transverse flux ($60^\circ < \text{zenith angle} \leq 90^\circ$) is roughly two times larger. On the other hand, the dependence of the photon number on the azimuth angle is shown in Figure 8.24. This figure says that the gamma-ray flux in FOV was statistically consistent to be uniform distribution (the resultant χ^2 fitting with a constant is 0.68), but the transverse gamma-ray flux had the azimuth angle variation. Comparing with the alignment of the accessories (the left of Figure 8.24), the directions of the high flux were quite consistent with the position of batteries. This fact means that the batteries might become the gamma-ray sources by the interaction with cosmic-rays. Then, we calculated the gamma-ray flux with the events of the azimuth angle between -45° and 75° , and we obtained the zenith angle dependence of the flux printed by boxes in Figure 8.23. The zenith angle dependence of the gamma-ray flux with the azimuth angle between -45° and 75° is roughly consistent with the calculation by Ling [50]. Therefore, we consider that the excess of the transverse flux was secondary gamma-rays by the interaction of batteries and cosmic-rays.

The detected photon number is listed in Table 8.4, and the relation of the atmospheric depth and the photon number, which is called a growth curve, is shown by the circles in Figure 8.25. The error bar in this figure is only statistical. In order to obtain both the fluxes of diffuse cosmic gamma-ray and atmospheric gamma-ray, we assumed two functions of the atmospheric depth. Because the flux of atmospheric gamma-ray is nearly proportional to the atmospheric depth [47], the flux is

$$f_{\text{atmos}}(z) = a \times (1 + k) \times z, \quad (8.3)$$

where z is the atmospheric depth, k is the ratio of the gamma-rays produced by the interaction of charged particles and the vessel to atmospheric gamma-rays, and a is a free parameter. From Figure 7.5, k is estimated to be 0.08 for 120 - 300 keV and 0.19 for 300 - 600 keV. On the other hand, diffuse cosmic gamma-rays are scattered or attenuated in atmosphere. Thus, the flux of diffuse cosmic gamma-ray is described as

$$f_{\text{cosmic}}(z) = b \times (1 + p) \times \exp(-z/\tau), \quad (8.4)$$

where τ is the mean free path of the total attenuation in the air, p is the scattered component term (see section 7.1.1), and b is a free parameter. Then we fitted the growth curve with the combination of two function

$$R(z) = A_{\text{eff}} \times (1 - \nu_{\text{vessel}}) \times (f_{\text{cosmic}} + f_{\text{atmos}}), \quad (8.5)$$

where A_{eff} and ν_{vessel} are the effective area of the flight model detector and the attenuation factor of the aluminium vessel, respectively. In Figure 8.25, the solid line, the dashed line and the dotted line are obtained $R(z)$, the cosmic component and the atmospheric component, respectively. Obtained a is $1.27 \times 10^{-1} \pm 3.3 \times 10^{-2}$ photons/(cm² sec str MeV (g/cm²)) for 120 - 300 keV and $1.43 \times 10^{-2} \pm 3.4 \times 10^{-3}$ photons/(cm² sec str MeV (g/cm²)) for 300 - 900 keV. Also obtained b is $7.49 \times 10^{-4} \pm 4.59 \times 10^{-4}$ photons/(cm² sec str keV) for 120 - 300 keV and $2.58 \times 10^{-4} \pm 5.6 \times 10^{-5}$ photons/(cm² sec str keV) for 300 - 900 keV. Moreover we assumed that both diffuse cosmic gamma-rays and atmospheric gamma-rays have a power law spectrum of $E^{-2.0}$ and $E^{-1.7}$ [46, 49], respectively, and then each gamma-ray flux obtained by fitting is

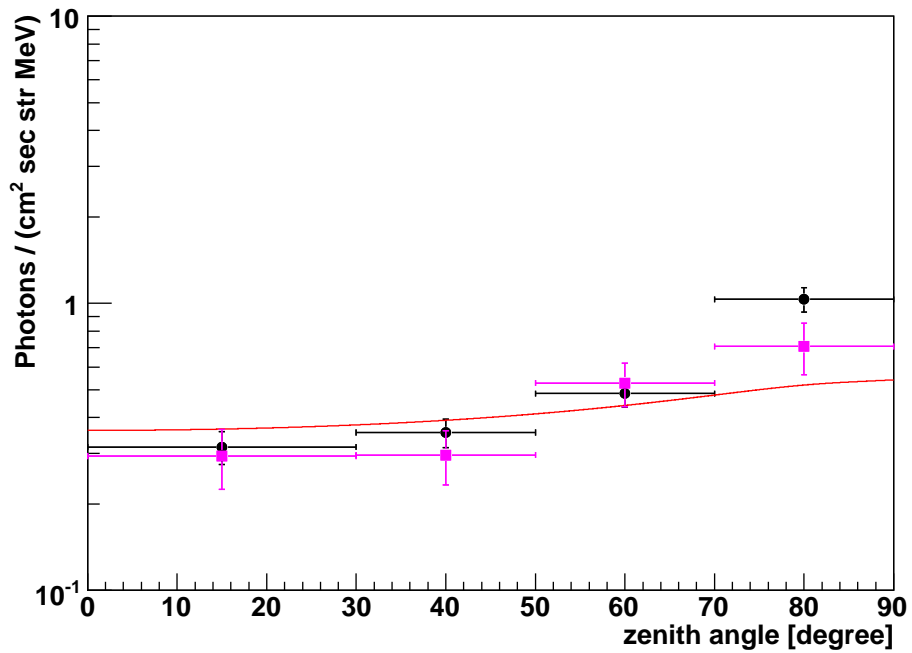


Figure 8.23: The dependence of the gamma-ray flux on the zenith angle during the level flight. The circles and the boxes were calculated with the events in all azimuth direction and in the limited azimuth direction, respectively. The error bar is the statistical sigma. The solid line is the calculated flux for 300 keV gamma-rays at the atmospheric depth of 7.0 g/cm^2 [50].

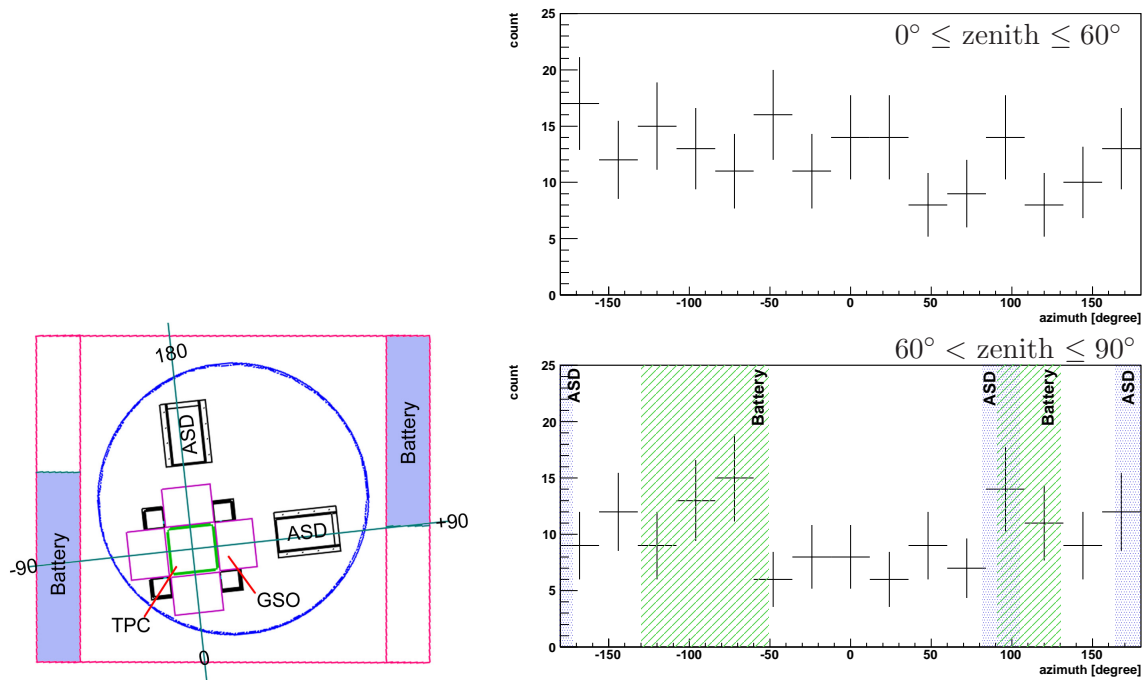


Figure 8.24: The definition of the azimuth angle (left) and the azimuth angle depending of the photon number (right).

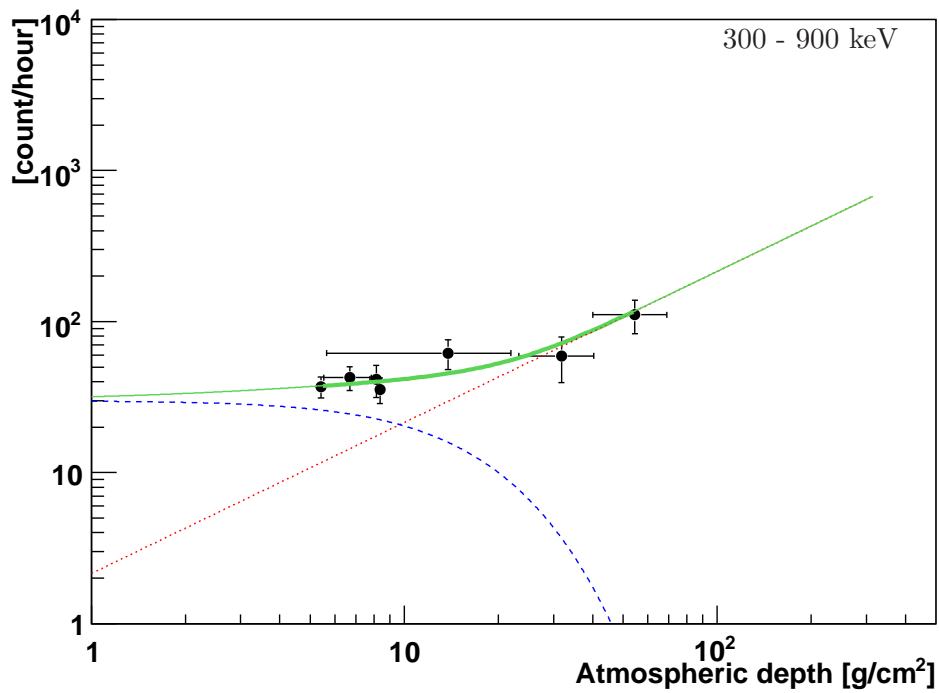
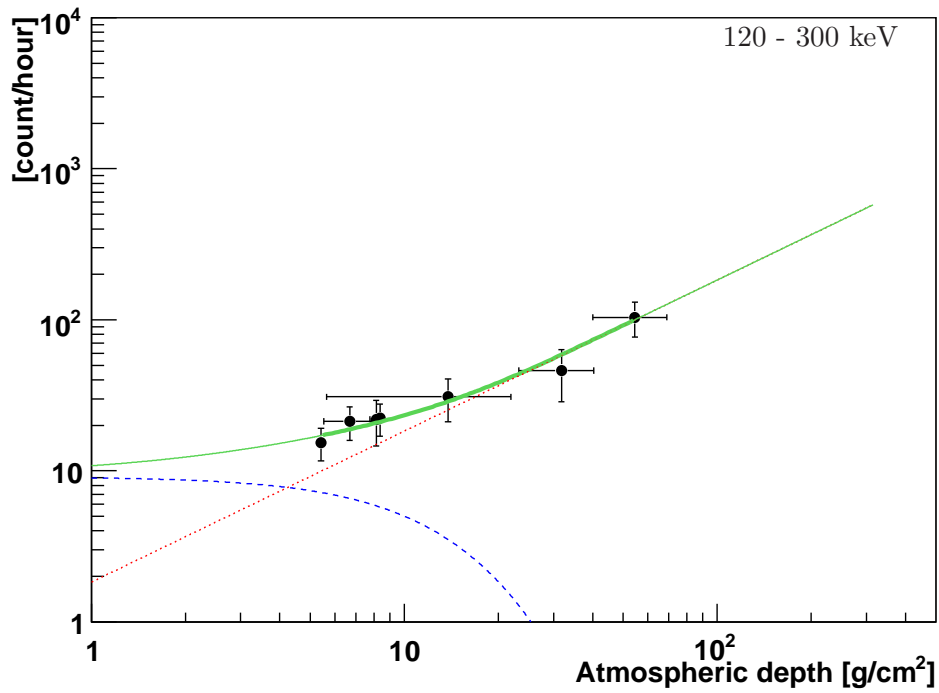


Figure 8.25: The relation of the atmospheric depth and the count rate (the growth curve). The circles are obtained data during this flight, and the error bar is the statistical sigma. The solid line is obtained by fitting of the data. The dotted-line and the dashed-line are diffuse cosmic gamma-rays and atmospheric gamma-rays, respectively.

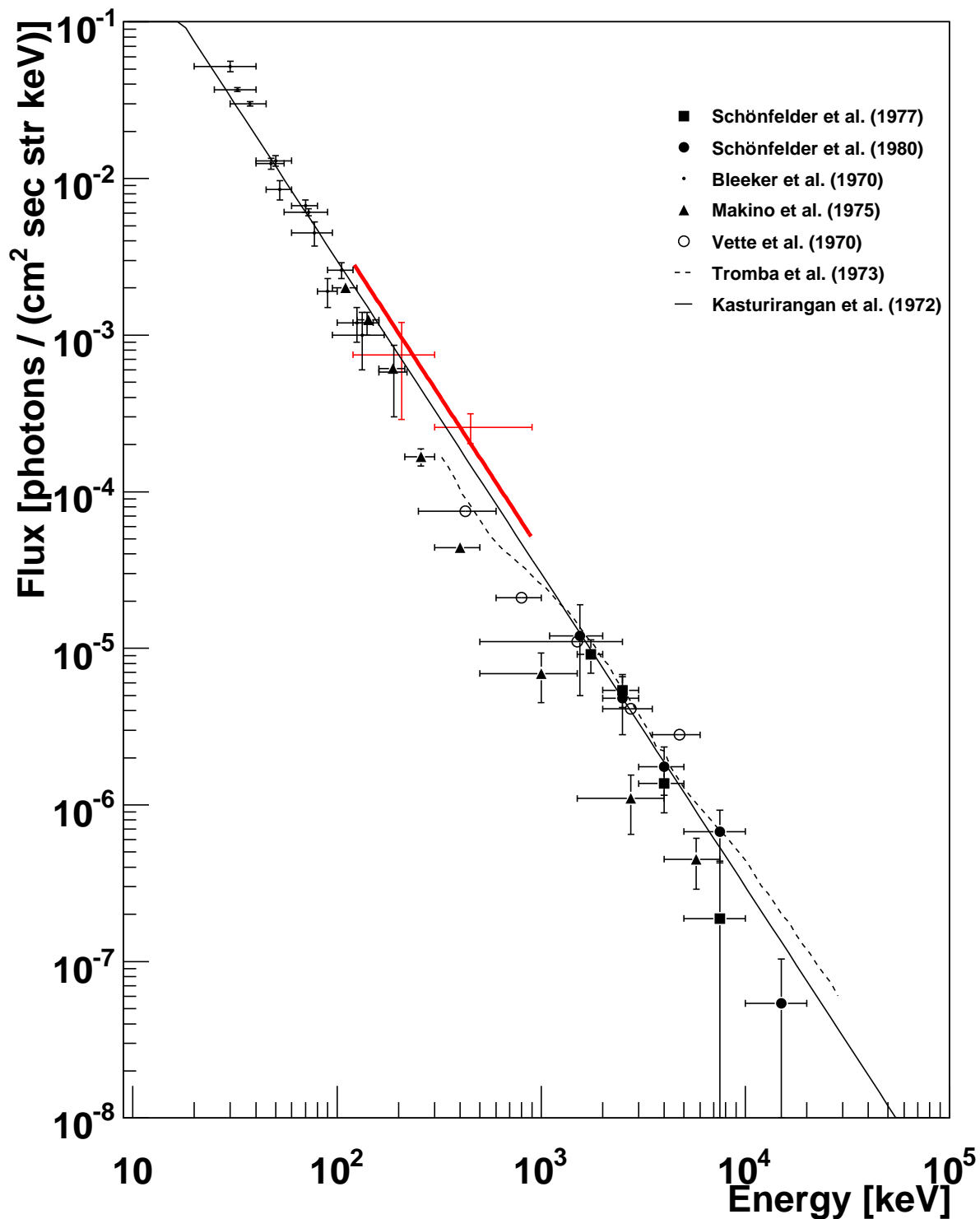


Figure 8.26: The obtained flux of diffuse cosmic gamma-rays. The red solid line is our result. The error bar includes only the stastic error, and the systematic error is a factor of about 2. For the comparison, we also plotted the results of past other groups [47, 51, 52, 53, 54, 55].

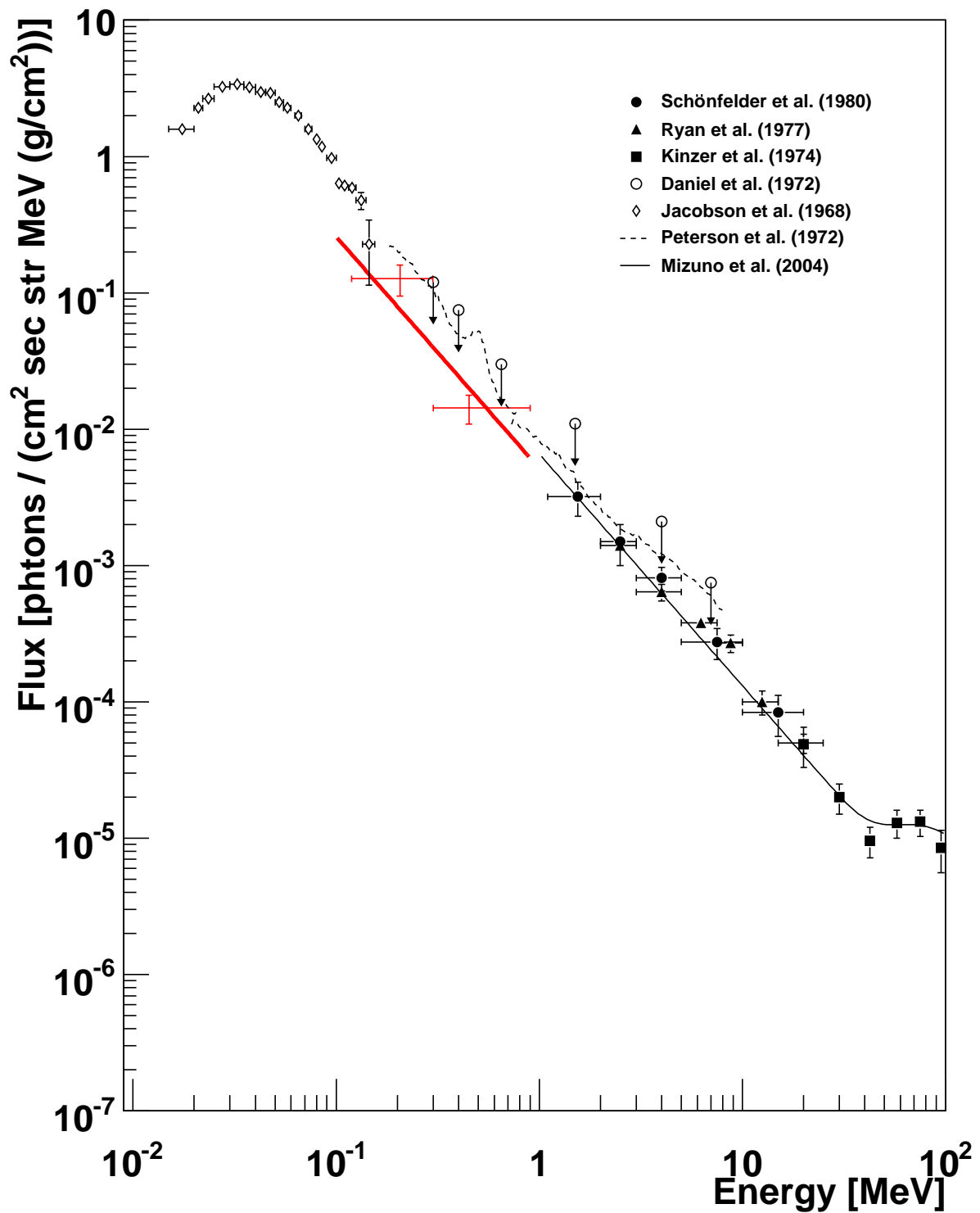


Figure 8.27: The obtained flux of atmospheric gamma-rays. The red solid line is our result. The error bar includes only the stastic error, and the systematic error is a factor of about 2. For the comparison, we also plotted the results of past other groups [51, 56, 57, 58, 59].

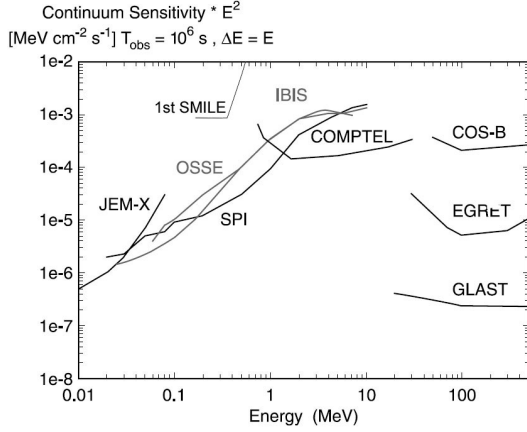


Figure 8.28: The comparison of the sensitivity for continuum component [38]

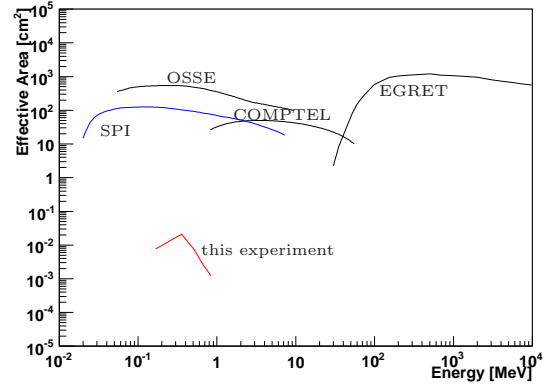


Figure 8.29: The comparison of the effective area [30, 60, 61]

described as follows,

$$F_{\text{cosmic}}(E) = (41 \pm 2) \times \left(\frac{E}{\text{keV}} \right)^{-2.0} \quad [\text{photons/cm}^2 \text{ sec str keV}], \quad (8.6)$$

$$F_{\text{atmos}}(E) = (0.65 \pm 0.16) \times \left(\frac{E}{\text{keV}} \right)^{-1.7} \quad [\text{photons/cm}^2 \text{ sec str keV (g/cm}^2)]. \quad (8.7)$$

The obtained fluxes of diffuse cosmic gamma-rays and atmospheric gamma-rays are compared with the results of previous balloon/rocket experiments, as shown in Figure 8.26 and 8.27, respectively. The systematic error is a factor of about 2 due to the uncertainty of the detection efficiency as described in section 7.4. These figure says that the obtained fluxes from SMILE are nearly consistent with those of the past experiments.

Finally, we calculated the detection sensitivity of this camera. The gamma-ray, which were observed by this experiment, are the background, when we would observe a point gamma-ray source. Thus, with the angular resolution of 20° and the observation time of 10^6 sec, the number of background photons N_B is expected as follows.

$$N_B = N_d \times \left(\frac{10^6 \text{ sec}}{3 \text{ hour}} \right) \times \left(\frac{0.1 \text{ str}}{3 \text{ str}} \right), \quad (8.8)$$

where N_d is the detected photon number of this experiment. Then, the number of the photon from the target celestial object for the significance of 3σ is

$$N_S = \frac{9 + 3\sqrt{9 + 8N_B}}{2}, \quad (8.9)$$

Therefore, the detectable minimum flux is

$$F_S = \frac{N_S}{A_{\text{eff}} \times 10^6 \text{ sec}} \quad [\text{photons} / (\text{cm}^2 \text{ sec})], \quad (8.10)$$

where A_{eff} is the effective area (see Figures 7.33 and 7.34). The detected photon number in the energy range of 200 - 400 keV during the level flight is 151 events, and A_{eff} is $2.13 \times 10^{-2} \text{ cm}^2$. Therefore, the detection sensitivity F_s is $2.2 \times 10^{-4} \text{ MeV} / \text{cm}^2 \text{ sec}$. The detectable minimum flux and the effective area of this experiment are shown in Figures 8.28 and 8.29, respectively. From these figures, although the effective area of this experiment is smaller by about three

order than that of COMPTEL, the detection sensitivity is smaller by only one order. This fact means that our camera has actually a high signal to noise ratio due to the kinematic fit based on Compton scattering. On the other hand, from these figures, if a $50 \times 50 \times 50 \text{ cm}^3$ detector, which has the effective area as same as COMPTEL, were realized in the future, the sensitivity would reach ten times of that of COMPTEL.

Chapter 9

Summary & Future Work

For the next generation MeV gamma-ray Compton camera, we developed an Electron Tracking Compton Camera, which consisted of a μ -TPC as a tracker and the GSO-PSAs as absorbers. First, we constructed a prototype camera using an Ar gas filled TPC, and we revealed the ability of an electron tracking Compton imaging, of which there are fully reconstruction of the direction of the incident gamma-rays, and in particular the background rejection due to the Compton scattering kinematics. For the 662 keV gamma-rays, the energy resolution and the angular resolutions ARM/SPD were 14 %, $\sim 9^\circ$ and $\sim 90^\circ$ at FWHM, respectively. The detection efficiency was $\sim 5 \times 10^{-6}$. Also the FOV of the prototype was obtained ~ 1 str. Next, in order to measure diffuse cosmic gamma-rays and atmospheric gamma-rays, we designed and constructed a flight model detector with an improvement of the detection efficiency for a balloon borne experiment. In the balloon borne experiment, the detection efficiency is most significant. Therefore, we decided to use a Xe gas, although the energy resolution and the angular resolution were little worse than those of the prototype, such as 19 %, $\sim 12^\circ$ and $\sim 200^\circ$ at FWHM for 662 keV, respectively. However, by a Xe gas TPC and a larger scintillator coverage, the detection efficiency was dramatically increased 10 times of that of the prototype, and the wide FOV spreaded to 3 str. Finally, we loaded the flight model on a balloon, and launched at 06:11 on September 1 2006 as the 1st flight of Sub-MeV gamma-ray Imaging Loaded-on-balloon Experiment (SMILE) from Sanriku Balloon Center (39.16N, 141.82E). The balloon reached to 35 km at 08:56, and the level flight continued during 4 hours. There was no serious problem on the balloon system and the flight model detector. Also we succeeded in the detection of ~ 200 downward gamma-rays during the 3.5 hours level flight (the live time of 3.0 hours). The detected photon number of ~ 200 photons in 3 hours was consistent to the simulated value, Then, we obtained the following fluxes of diffuse cosmic gamma-rays and atmospheric gamma-rays with the growth curve of this experiment,

$$F_{\text{cosmic}}(E) = (41 \pm 2) \times \left(\frac{E}{\text{keV}} \right)^{-2.0} \quad [\text{photons} / \text{cm}^2 \text{ sec str keV}], \quad (9.1)$$

$$F_{\text{atmos}}(E) = (0.65 \pm 0.16) \times \left(\frac{E}{\text{keV}} \right)^{-1.7} \quad [\text{photons} / \text{cm}^2 \text{ sec str keV (g/cm}^2)]. \quad (9.2)$$

where we assumed that the power law index of F_{cosmic} and F_{atmos} are -2.0 and -1.7 , respectively. These spectra are consistent with the previous data. Moreover, although the effective area of 1st SMILE was 3 order smaller than that of COMPTEL, the sensitivity of the MeV camera of this experiment was about 1 order worse than the sensitivity of COMPTEL, which means that our detector improve the signal to noise ratio by 1.5 order better than that of COMPTEL. This experiment is the first observation result in sub-MeV region by a Compton camera. Because there are many backgrounds due to charged particles, the observation in this energy band is very difficult. Actually, there has existed few observations of atmospheric gamma-ray flux in

sub-MeV region so far. Thus, it is very important that our detector obtained both the fluxes and the zenith angle dependence of diffuse cosmic gamma-rays and the atmospheric gamma-rays in the sub-MeV region.

The purpose of the next balloon experiment is the test of the imaging power, by the observation of a bright source like Crab nebula or Cyg X-1. Because an imaging needs a lot of photons, we must develop a μ -TPC having a larger volume of $30 \times 30 \times 30 \text{ cm}^3$. Figure 7.6 says that the efficiency of the current analysis is 10 - 30 %, and also Figure 5.18 shows that the obtained direction of the recoil electron is not so accurate. Therefore, the improvement of the analysis for the reconstruction of the recoil electron would improve both the effective area and the angular resolution. On the other hand, the increase of the μ -TPC volume gives an increase of the area of the absorber. When we construct the 2nd flight model similar to the 1st flight detector, the readout circuit of μ -TPC and GSO are 3 times and 10 times of those of the 1st flight model, respectively. Thus, we must also develop the low power readout circuit.

We have already started to develop a $30 \times 30 \times 30 \text{ cm}^3$ TPC using a $30 \times 30 \text{ cm}^2$ μ -PIC. However, for the tracker of the Compton camera, we will need study a gas as a Compton scattering target. Although we used Xe gas for the 1st flight model μ -TPC, the drift velocity of electron in Xe gas is too slow and the cross section of absorption of Xe atom is too large. Thus, by using Xe gas, the random coincidence might be increased, and also the background event, for example the events of scattering from the GSO, might be increased. As the candidate of the Compton target gas, we consider a CF_4 gas, which has 42 electrons per one molecule and consists of the low Z atoms. Also the drift velocity of electron in a CF_4 gas is rapider than that in an Ar gas. On the other hand, since the gas gain of a CF_4 gas is not high, the problem of the increase of the operation high voltage remains.

After these improvements, our detector would be able to obtain a few hundred photons from Crab nebula by a 3 hours level flight, because the effective area will be ~ 30 times larger than that of the 1st flight model. Also, if a ~ 10 days level flight is realized, our camera will be able to detect the other celestial objects, like Cen A which is a radio galaxy and its flux is about 0.1 Crab [62].

reference

- [1] V. Schönfelder; “The Universe in Gamma Rays”, *Springer* (2001).
- [2] M.Oda and K. Matshuoka; *Progress in Elementary Particles and Cosmic-Ray Physics*, **10** (1971), 305.
- [3] K. S. Cheng, G. E. Romero; “Cosmic Gamma-Ray Sources”, textitKluwer Academic publishers (2004).
- [4] P. V. Ballmoos; *Experimental Astronomy*, **6** (1995), 85.
- [5] V. Schönfelder et al.; *Astron. Astrophys. Suppl. Ser.*, **143** (2000), 145.
- [6] R. C. Hartman et al.; *ApJS*, **123** (1999) 79.
- [7] S. E. Boggs et al.; *ApJ*, **544** (2000), 320.
- [8] M. Pohl; astro-ph/9807267.
- [9] R. A. Chevalier; *Nature*, **355** (1992), 691.
- [10] A. Lyne and F. G. Smith; “Pulsar Astronomy”, *Cambridge* (2005).
- [11] D. J. Thompson et al.; *ApJ*, **516** (1999), 297.
- [12] L. Kuiper et al.; *A&A*, **378** (2001), 918.
- [13] F. A. Aharonian, A. M. Atoyan; astro-ph/9803091.
- [14] M. L. McConnell et al.; *ApJ*, **572** (2002), 984.
- [15] W. R. Purcell et al.; *ApJ*, **491** (1997), 725.
- [16] G. Weidenspointner et al.; *A & A*, **450** (2006), 1013.
- [17] R. Schödel et al.; *Nature*, **419** (2002), 694.
- [18] C. M. Urry, P. Padovani; (http://heasarc.gsfc.nasa.gov/docs/objects/agn/agn_model.html)
- [19] M. Chiaberge et al.; *MNRAS*, **324** (2001), 33.
- [20] L. Maraschi, F. Tavecchio; astro-ph/0102295.
- [21] G. H. Share, R. J. Murphy; *ASP Conference Series*, **206** (2000), 377.
- [22] M. S. Briggs et al.; *ApJ*, **524** (1999), 82.
- [23] W. S. Paciesas et al.; *ApJS*, **122** (1999), 465.
- [24] XCOM; Photon Cross Section Database (<http://physics.nist.gov/PhysRefData/Xcom/Text/XCOM.html>).

REFERENCE

- [25] G. F. Knoll; “Radiation Detection and Measurement 3rd edition”, *WILEY* (2001).
- [26] M. S. Longair; “High Energy Astrophysics”, *Cambridge university press*, (1994).
- [27] Jean in’t Zand; “Coded Aperture Imaging in High-Energy Astronomy”,
(<http://lheawww.gsfc.nasa.gov/docs/cai/coded.html>).
- [28] P. v. Ballmoos et al.; *Exp. Astron.*, **20** (2005), 253.
- [29] P. v. Ballmoos; *Proc. of Astronomy with Radioactivities IV and MeV Gamma-Ray Telescopes*,
(http://www.mpe.mpg.de/gamma/science/lines/workshops/seeon03/ballmoos_1.pdf).
- [30] V. Schönfelder et al.; *ApJS*, **86** (1993), 657.
- [31] J. M. Ryan; *Proc. of Astronomy with Radioactivities IV and MeV Gamma-Ray Telescopes*
(http://www.mpe.mpg.de/gamma/science/lines/workshops/seeon03/ryan_1.pdf).
- [32] T. Kamae et al.; *NIM*, **A260** (1987), 254.
- [33] W. Coburn et al.; *Proc. SPIE*, **5898** (2005).
- [34] P. F. Bloser et al.; *New Astronomy Reviews*, **46** (2002), 611.
- [35] G. Weidenspointner et al.; *A&A*, **368** (2001), 347.
- [36] A. Zogauer, G. Kanbach; *Proceeding of SPIE*, **4851** (2003), 1302.
- [37] G. R. Lynch, O. I. Dahl; *NIM*, **B 58** (1991), 6.
- [38] V. Schönfelder; *New Astronomy Reviews*, **48** (2004), 193.
- [39] T. Takahashi.
- [40] T. Nagayoshi; Ph. D. Thesis, Kyoto Univ. (2004).
- [41] H. Kubo; *NIM*, **A 513** (2003), 94.
- [42] O. Sasaki; “Amplifier-Shaper-Discriminator ICs and ASD Boards”
(<http://online.kek.jp/~sosamu/ASD-PRR.pdf>)
- [43] A. Takeda et al.; *IEEE NS*, **51** (2004), 2140.
- [44] F. Sauli; *NIM*, **A 386** (1997), 531.
- [45] R. Orito; Ph. D. Thesis, Kyoto Univ. (2005).
- [46] K. Kasturirangan, U. R. Rao; *Astro. Space Sci.*, **15** (1972), 161.
- [47] V. Schönfelder et al.; *ApJ*, **217** (1977), 306.
- [48] F. Makino; *Astro. Space Sci.*, **8** (1970), 251.
- [49] T. Mizuno, et al.; *ApJ*, **614** (2004), 1113.
- [50] J. C, Ling; *J. Geophys. Res.*, **80** (1975), 3241.
- [51] V. Schönfelder et al.; *ApJ*, **240** (1980), 350.
- [52] J. A. Bleeker, A. J. M. Deerenberg; *ApJ*, **159** (1970), 215.

- [53] F. Makino; *Astro. Space Sci.*, **37** (1975), 115.
- [54] J. I. Vette et al.; *ApJ*, **160** (1970), 161.
- [55] J. I. Trombka et al.; *ApJ*, **181** (1973), 737.
- [56] J. M. Ryan et al.; *J. Geophys. Res.*, **82** (1977), 3593.
- [57] R. L. Kinzer et al.; *J. Geophys. Res.*, **79** (1974), 4567.
- [58] R. R. Daniel et al.; *Astro. Space Sci.*, **18** (1972), 462.
- [59] L. E. Peterson et al.; *Space Sci. Rev.*, **13** (1972), 320.
- [60] D. J. Thompson et al.; *ApJS*, **86** (1993), 629.
- [61] D. Attié et al.; *A & A*, **411** (2003), 71.
- [62] H. Steinle et al.; *A & A*, **330** (1998), 97.

Acknowledgments

I am deeply grateful to Professor Toru Tanimori for his guidance and encouragements in this work. This thesis would not be completed without his support. I specially thanks the SMILE team: Dr. Hidetoshi Kubo, Hironobu Nishimura, Kazuki Ueno. Also I would like to thank μ -PIC collaborators: Dr. Miuchi, Dr. Tsuchiya, Dr. Kabuki, Okada, Hattori, Kurosawa (Kyoto Univ.), Dr. Takeda, Dr. Sekiya (ICRR), Dr. Nagayosi (Waseda Univ.), Dr. Ueno (Tokyo Institute of Technology), Dr. Orito (Kobe Univ.), Dr. O. Bouianov (Espoo-Vantaa Institute of technology) and Dr. M. Bouianov (CSC-Scientific Computing Ltd.). I am grateful to all the member of the cosmic ray laboratory in Kyoto University for their continuous discussions and encouragements.

I sincerely thank Professor Yamagami, Professor Yoshida, Professor Saito, Nonaka, Mizuta, Professor Takahashi, Dr. Nakazawa (ISAS/JAXA), Professor Gunji (Yamagata Univ.), and the member of Sanriku Balloon Center (ISAS/JAXA) for a lot of advices and assistances of the balloon experiment. I thank Professor Nagae (KEK) and members of his laboratory, who helped the experiment at T1 beam line in the Proton Synchrotron at KEK.

I appreciate Tomohisa Motomura (D.T. Circuit Technology Co., Ltd.) and the staffs of D.T. Circuit Technology and TOSHIBA who manufactured the μ -PIC and gave us several technical informations about the manufacturing process. For the production of the SMILE system, I am grateful to Ogawa, Tanaka (Arkus), Uchiyama, Shimizu (Clear Pulse), Ozawa, Okada (Hitachi KMS), Yoribayashi(Houshin), Kochou (Max-Electronics), Matsumaru (REPIC), Oyobe (Sansei System), Hiruta (Shinwa Denzai). I thank Mori (Furamingo) for the production of the gondola, and I also thank Shimizu (Rikensha) for the creating the TPC vessel.

This work was supported by a Grant-in-Aid in Scientific Research of the Japan Ministry of Education, Culture, Science, Sports and Technology. Also, this work was supported by a Grand-in-Aid for the 21st Century COE “Center for Diversity and Universality in Physics”, and the Japan Society for Promotion of Science for Young Scientists.